Technical Report

Pattern Recognition and Image Processing Group
Institute of Computer Aided Automation
Vienna University of Technology
Favoritenstr. 9/1832
A-1040 Vienna AUSTRIA
Phone: +43 (1) 58801-18351
Fax: +43 (1) 58801-18392
E-mail: mara@prip.tuwien.ac.at
URL: http://www.prip.tuwien.ac.at/

PRIP-TR-103 14. February 2006

Documentation of Rotationally Symmetric Archaeological Finds by 3D Shape Estimation

Hubert Mara

Abstract

Tens of thousands of fragments of ceramics (called sherds for short) are found at every archaeological excavation site and have to be documented for further archaeological research. The traditional documentation is based on the profile line, which is the intersection of the sherd along the axis of symmetry in the direction of the rotational axis.

Traditionally this is done by experts by manually drawing the profile line, using different tools like a *Profilkamm* (profile comb), flexible wires, circle- templates, etc. to estimate the axis of rotation and the profile line. The traditional drawing is error prone and time consuming, therefore a semiautomatic method using a *Profilograph* was introduced to increase accuracy. Since the measurement is still manually, the time for drawing was not decreased.

We propose a fully automatic system for the estimation of the rotational axis and the profile line. For data-acquisition we are using acquisition methods based on the principle of structured light, which have also been compared in respect to accuracy and performance to traditional methods of documentation. Based on continuous experiments and comparisons we show a new method for estimation of the rotational axis and the profile line, which is inspired by traditional archaeological methods.

The methods shown in this thesis were tested on synthetic and real data. The experiments with real data were done at the archaeological excavation in *Tel Dor* in Israel. The results for estimation of the profile line and the comparison between the manual drawings, the *Profilograph* and the 3D- acquisition by structured light are shown in this thesis. Furthermore methodological experiments of geometrical surface analysis are shown, which demonstrate the possibility of estimation of ancient manufacturing techniques of ceramics. Finally an outlook towards detection of lines and analysis of painted ceramics is given.

Kurzfassung

Zehntausende Scherben von Keramiken werden auf archäologischen Ausgrabungen gefunden. Diese Tonscherben müssen für abschließende wissenschaftliche Untersuchungen dokumentiert werden. Grundlage dieser Dokumentation ist bis heute die händische Zeichnung der Profillinie, welche einen vertikalen Schnitt durch die Scherbe entlang der Rotationsachse, auch Symetrieachse genannt, beschreibt.

Die Handzeichnungen der Profillinie und die dafür benötigte Rotationsachse werden von Archäologen unter zur Hilfenahme verschiedenster Werkzeuge, wie zum Beispiel dem Profilkamm, flexiblem Bleidraht oder Kreisschablonen erstellt. Diese traditionelle Methode der Dokumentation ist allerdings sehr zeitaufwendig und fehleranfällig. Daher wurde der *Profilograph* entwickelt, der mit manuellem, mechanischem Abtasten der Scherben die Profillinie zur Weiterverarbeitung an einen Computer übermittelt.

Da auch der *Profilograph* auf Grund der manuellen Arbeitsschritte keine schnellere Dokumentation ermöglicht, wurde ein automatisches System zur Aufnahme von Scherben und zur automatisierten Berechnung der Profillinie entwickelt. Die Erfassung wird mittels Lichtschnittverfahren (strukturiertes Licht) durchgeführt. Aus den Aufnahmen wird ein 3D-Modell erstellt, aus dem die Rotationsachse und somit die Profillinie von Scherben berechnet wird.

Durch ständige Experimente, Zusammenarbeit mit Archäologen und dem Vergleich mit traditionellen Methoden, wurde das automatische System weiterentwickelt. Diese Arbeit stellt eine neue Methode zur Bestimmung der Rotationsachse, basierend auf den traditionellen Methoden der Archäologen vor, welche eine genauere Berechnung der Profillinie ermöglicht. Weiters werden auch methodische Experimente zur Analyse der Geometrie von Keramiken gezeigt, welche Rückschlüsse auf antike Fertigungstechniken ermöglichen.

Das vorgestellte System wurde auf künstlichen und realen Daten getestet. Für die Experimente mit realen Daten wurde das System mittels Funden der archäologischen Ausgrabung in *Tel Dor* in Israel getestet und mit den traditionellen Handzeichnungen und dem *Profilograph*en verglichen. Die Ergebnisse im Bezug auf dokumentierten Scherben pro Stunde und zur Präzision der verschiedenen Verfahren werden in diesem Dokument gezeigt. Abschließend werden künftige Erweiterungen vorgestellt.

Contents

Chapter 1

Introduction

The methods for 3D-acquisition, post-processing, analysis and comparison to traditional and other existing systems in this thesis have been done as part of the Austrian Science Foundation (FWF) project *Computer Aided Classification of Ceramics* which was performed by the Pattern Recognition and Image Processing (PRIP) Group at the Institute of Computer Aided Automation at the Vienna University of Technology.

Motivated by the requirements of modern archaeology we are developing an automated system for documentation of pottery. Pottery are among the most widespread finds in archaeology, because ceramics have been used by mankind for several thousands of years for daily live. As pottery does not decay like wood and has not been reused like objects made of metal it is found in numbers of tens of thousands on excavations of habitats like for our examples the ancient cities of *Carnuntum* [Grü79] in Austria, *Sagalassos* [Deg00] in Turkey and *Tel Dor* [Ste00] in Israel. Figure 1.1 shows an excavated area with buckets full of sherds, sorted sherds and their storage.

(a) (b) (c)

Figure 1.1: *Tel Dor*: (a) Area D with buckets full of sherds (b) cleaned sherds (c) storage of sherds.

These three ancient cities and their related excavation groups were the partners of the PRIP Group, which has an interest in application of Computer Vision methods in archaeology. The reason for that strong interest in archaeology and other applications of cultural heritage is based on the fact that the variety and number of objects to be recognized is larger than in industrial applications, where the ground truth of objects is

well known. In this thesis we will show our latest results of the cooperation with the *Weizmann Institute of Science* (WIS) and the *Israel Exploration Society* responsible for the excavation of *Tel Dor*.

Tel Dor is an important excavation, because it was for several thousand years an important harbor and therefore trading place at the Mediterranean Sea. Figure 1.1(a) shows the large number of sherds found at the excavation in *Tel Dor* in a few hours. The sherds are collected with buckets and brought to the excavations office, where they are cleaned and documented (see Figure 1.1(b) and the next section) and finally put into a storage container (Figure 1.1(c)).

The remainder of this chapter will give an overview of the automated archaeological documentation using 3D-acquisition, followed by an outline of the thesis structure.

1.1 Archaeological Documentation

In habitats ceramics (pottery) usually have been used until it was heavily broken and therefore could not be used anymore. The fragments of ceramics are shortly called sherds. These sherds have been used as filling material for floors and walls or dumped in trash pits. Therefore archaeologists find these tens of thousands of sherds in layers (called loci) with context to time periods and cultural groups. Furthermore sherds represent information about population movements, inter-regional contacts, production context, and technical or functional constraints (archaeometry [Leu87]). The documentation, classification and publication (e.g. [Gil01]) of these tens of thousands of sherds is an important task for archaeologists [OTV93]. Figure 1.2 shows such an example of a sherd, which we will use to demonstrate our method.

Figure 1.2: A sherd found during season 1998-2000 in area D1 in *Tel Dor*, Israel.

The basic information that is collected about sherds are the place where it has been found and its profile line, which is an intersection of the sherds along the axis of symmetry. This axis of symmetry is also called axis of rotation and can be found for sherds manufactured on rotational plates [YM97], which were used to produce pottery for daily life. Additionally the fabric, which is the structure and the color of the sherd, is described. The traditional way is to draw the profile line and the decorations of the surface of the

sherd by hand. Figure 1.3 shows the manual drawing of the profile line, the registration number, and the fabric ("dark orange fabric, well levigated"). The registration number "98-00 D1 260901" shows that the sherd has been found during the excavation season 1998 to 2000 in area D1 in locus number 260901. The numbering system for archaeological artifacts are regulated by the excavators and therefore the formatting is different between excavations.

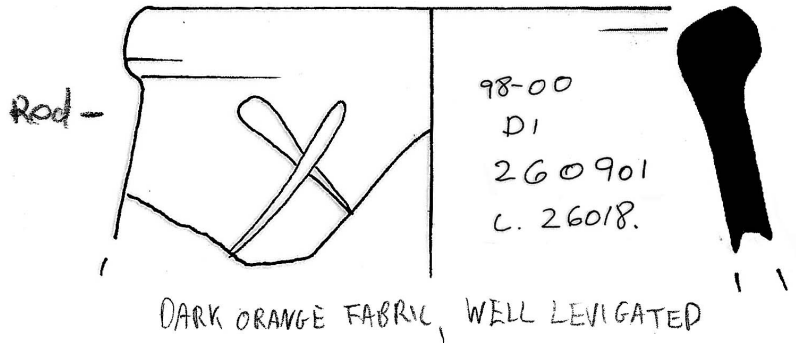

Figure 1.3: The manual drawing of the profile line, surface and the description of sherd number "98-00 D1 260901" from Figure 1.2.

Drawing and orientating the sherd so that its profile line corresponds to the orientation and the rotational axis of the unbroken vessel requires expert knowledge and a skilled draftsman. The time required for drawing such a profile with pencil and ink is approximately 10 or more minutes per sherd. Archaeologists use a *Profilkamm* (profile comb) (Figure 1.4(a)) which consist of horizontally moveable pins, which are fixed by a clamp, where the ends of the pins describe the profile line. Figure 1.4(b) shows further tools for manually drawing the profile line: The scale-paper which consists of circle templates is used for estimation of the diameter of a sherd. Another tool used by archaeologists in similar manner is the lead-wire. It is used like the *Profilkamm* to cast the profile line along the wall of the sherd. Afterwards the casted lead-wire is used to stencil the profile line on paper. Although this tool increases the precision of the drawing it does not increase the processing speed and it can not be used for fragile or painted sherds, because this tool is pressed against the surface and therefore leaves scratches. Therfore such sherds can only be drawn free-handed without any proper measurements.

1.2 Existing Systems

With the increasing use of computers for commercial applications during the 1980's, two systems were developed to apply computerized methods for documentation of sherds. These systems are called *ARCOS* (*AR*chaeological *CO*mputer *S*ystem) [Gat84, LK89] and *SAMOS* (*S*tatistical *A*nalysis of *M*athematical *O*bject *S*tructers) [Ste88, Ste89]. Both systems are half-automated and therefore they require user interaction as described in [SMD91]. The resolution of approx. 2 *mm* between points of the profile lines generated by these systems is not sufficient for archaeological publications.

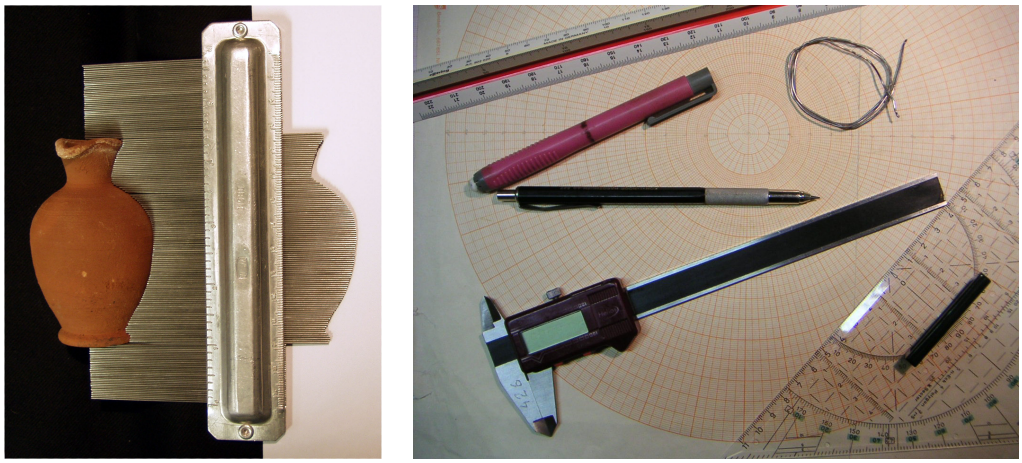

(a) (b)

Figure 1.4: Tools for drawing a profile line: (a) *Profilkamm*, (b) pens, scale paper, lead-wire, ruler and sliding calliper.

To increase the resolution the *Profilograph* [UD02] was developed during the 1990's. It is a Human Interface Device (HID), which transfers manually pin-pointed 3D-coordinates of a surface of a sherd to a computer. For pin-pointing a needle-shaped sensor (push-button) is used. Later versions of the *Profilograph* (Figure 1.5) include a laser-pointer to acquire points without physical contact of the surface. The *Profilograph* requires a similar amount of user interaction like *ARCOS* & *SAMOS*.

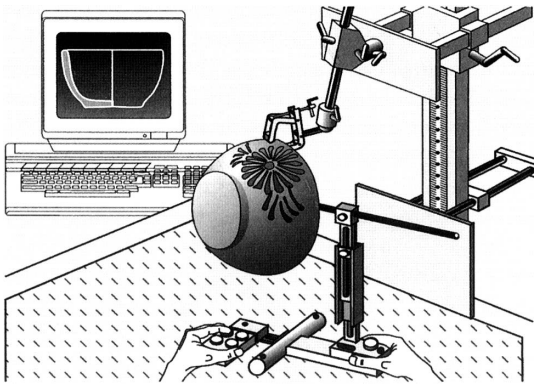

Figure 1.5: Scheme of the *Profilograph* [UD02] for digital but manual acquisition of the profile line.

Therefore we are propsing an automated method for orientation of sherds and estimation of profile lines using a 3D-scanner based on the principle of structured light [KS99a, CIG+01, KS01, SK02]. Todays computers can process large amounts of data generated by modern 3D-scanners which have a resolution of less than 0.5 *mm* between two points of the surface of a sherd. So we were motivated to develop a fully automated, digital and portable system for acquisition and processing for archaeological documentation that requires a minimum of user interaction.

1.3 Thesis Structure & Contribution

The main contribution of this thesis is the estimation of the rotational axis of fragments of rotationally, symmetric objects. Therefore we applied and compared existing methods for estimation of the rotational axis to such fragments. As the existing methods require either manual interaction or complete objects, we choose to implement a new method inspired by the manual method for orientation sucessfully used by archaeologists for several decades.

Our main application and our real-data for experiments are archaeological finds. As the environment at an archaeological excavation site is not as clean as in a laboratory and due to the time-concerns about the massive amount of findings the second part is the processing of sherds. Both parts have been tested with synthetic objects and with real sherds as shown and compared to other methods in the third part. Finally we propose a method to demonstrate the extended use of 3D-acquisition before a summary and an outlook are given.

Therefore this document is structured into following Chapters: Chapter 2 presents the mathematical background necessary to understand the geometrical equations used for acquisition, processing and estimation of the rotational axis. To understand the demands of archaeologists, this chapter shows the traditional archaeological documentation and classification of finds. Chapter 3 describes the acquisition systems we have been using for sherds from Vienna, Austria. It also covers the setup we used, when we joined the field-trip to the excavation to *Tel Dor* in Israel to test, compare and improve our actual system. The estimation of the rotational axis is shown in Chapter 4 followed by the Chapter 5 concerning the processing of sherds. Both chapters include experiments with synthetic data. Furthermore Chapter 5 includes experiments with well-known objects. The experiments with real data from the excavation and the comparison with manual drawings and the Profilograph are shown in Chapter 6. Finally a conclusion for this thesis and an outlook for future enhancements is given in chapter 8.

Chapter 2

Theoretical Background

This chapter introduces the mathematical background for 3D-acquisition and processing of archaeological finds. The first part (Section 2.1) shows the geometrical methods used for acquisition of $2\frac{1}{2}$D-images (depth-images) shown in Chapter 3. The principles of these methods and their notation are required for Chapter 4 and Chapter 5. As archaeological documentation is our application, Section 2.2 describes archaeological terms and shows examples for manual archaeological documentation and classification.

2.1 $2\frac{1}{2}$D-coordinates using Structured Light

The acquisition using structured light is based on the geometrical principal of triangulation. The simplest setup would consist of two parts: a pinhole camera [Nal93], which assumes an ideal camera and a light source emitting a single ray of light. This ray is reflected on the point of intersection of the ray with the surface of an object. This point of the surface is acquired by the camera. The distance between a point highlighted by the light source and a camera acquiring this point can be triangulated, if the relative positions of the camera to the light source is known. Furthermore the perspective projection of the points highlighted by the light source, which emits either a single ray of light (Section 2.1.2) or a plane of light (Section 2.1.2) is transformed into a parallel projection. The result is a depth-image, which contains $2\frac{1}{2}$D-coordinates.

2.1.1 Homogenous Coordinates and Affine Transformations

Estimations in a 3D-space are traditionally described by addition and multiplication of 3×1 vectors. The drawback using these traditional methods is that they have to be performed step-by-step and can not be predetermined. Predetermination is important in respect to performance for our method, because our 3D-models consist of thousands of vertices and triangles, which have to be translated, rotated, intersected, etc. Therefore we use homogeneous coordinates in this thesis, because vectors, lines, planes, transformations, intersections, etc. can be predetermined by combination of $4\times n$ matrices for 3D-coordinates. This $4\times n$ matrices are also well suited for calculations by use of modern

computer architectures. In general vectors are described by $\mathbf{v}^T = (v_1, v_2, v_3, v_4)$ and affine transformations by 4×4 matrices:

$$\mathbf{v}' = \mathbf{A}\mathbf{v} = \begin{pmatrix} r_{11} & r_{12} & r_{13} & t_1 \\ r_{21} & r_{22} & r_{23} & t_2 \\ r_{31} & r_{32} & r_{33} & t_3 \\ p_1 & p_2 & p_3 & s \end{pmatrix} \begin{pmatrix} v_x \\ v_y \\ v_z \\ v_h \end{pmatrix} \tag{2.1}$$

The components of the affine transformation $\mathbf{A}$, with $i, j = \{1, 2, 3\}$ correspond to:

- r_{ij} ... Rotation or scaling
- t_i ... Translation
- p_j ... Perspective transformation
- s ... scaling

Table 2.1 shows commonly used affine transformations for translation $\mathbf{T} = (t_1, t_2, t_3)^T$, and rotation about an angle α about the axes of the coordinate system.

$$\mathbf{T} = \begin{pmatrix} 1 & 0 & 0 & t_x \\ 0 & 1 & 0 & t_y \\ 0 & 0 & 1 & t_z \\ 0 & 0 & 0 & 1 \end{pmatrix}$$
(a)

$$\mathbf{R}_x = \begin{pmatrix} 1 & 0 & 0 & 0 \\ 0 & cos(\alpha) & -sin(\alpha) & 0 \\ 0 & sin(\alpha) & cos(\alpha) & 0 \\ 0 & 0 & 0 & 1 \end{pmatrix}$$
(b)

$$\mathbf{R}_y = \begin{pmatrix} cos(\alpha) & 0 & sin(\alpha) & 0 \\ 0 & 1 & 0 & 0 \\ -sin(\alpha) & 0 & cos(\alpha) & 0 \\ 0 & 0 & 0 & 1 \end{pmatrix}$$
(c)

$$\mathbf{R}_z = \begin{pmatrix} cos(\alpha) & -sin(\alpha) & 0 & 0 \\ sin(\alpha) & cos(\alpha) & 0 & 0 \\ 0 & 0 & 1 & 0 \\ 0 & 0 & 0 & 1 \end{pmatrix}$$
(d)

Table 2.1: Common affine transformations for (a) translation and rotation about the (b) x-axis, (c) y-axis and (d) z-axis.

As v_4 corresponds to a the scaling s for vectors, a vector describing a vertex $(x, y, z)^T$ has a scaling of 1 and therefore we get the homogenous vector $\mathbf{v} = [x, y, z, 1]^T$. Furthermore vectors describing a direction like for example a normal-vectors $(n_x, n_y, n_z)^T$ have a scaling of 0 and therefore we get the homogenous normal-vector $\mathbf{n} = (n_x, n_y, n_z, 0)^T$.

2.1.2 $\frac{1}{2}$D-acquisition using a Camera and a Laser

As our acquisition-system consists of a laser and a camera, we use the ideal models for explanation of the general understanding in this section. So we use the model of the pinhole-camera which consists of a point of projection, rather than a lens and an ideal image-plane on which a scene is projected.

Is $\mathbf{u}^T = (n1, n2, n3, -d)$ the image-plane with the normal-vector $\mathbf{n} = (n_1, n_2, n_3, 0)$ and the center-point $a^T = (a, b, c, 1)$ of the projection P^C, so the projection $\mathbf{x}'_p$ of a point $\mathbf{x}_p = (x_p, y_p, z_p, 1)$ can be estimated by intersecting the line $\mathbf{a}\mathbf{x}_p$ with $\mathbf{u}$. The line $\mathbf{a}\mathbf{x}_p$ is described by the homogenous 4×4 matrix $\mathbf{G}$:

$$\mathbf{G} = \mathbf{a}\mathbf{x}_p^T - \mathbf{x}_p\mathbf{a}^T \tag{2.2}$$

The projection of $\mathbf{x}_p$ through $\mathbf{a}$ on $\mathbf{u}$ is the point of intersection $\mathbf{s}$ of the line $\mathbf{G}$ with the plane $\mathbf{u}$. The point $\mathbf{s}$ is estimated by:

$$\mathbf{s} = \mathbf{G}\mathbf{u} = \left(\mathbf{a}\mathbf{x}_p^T - \mathbf{x}_p\mathbf{a}^T\right)\mathbf{u} \tag{2.3}$$

Equation 2.3 can be transfered into an affine transformation of $\mathbf{x}_p \mapsto \mathbf{x}'_p$:

$$\mathbf{x}'_p = \mathbf{G}\mathbf{u} = \left(\mathbf{u}^T\mathbf{a}\right)\mathbf{x}_p - \left(\mathbf{u}^T\mathbf{a}\right)\mathbf{x}_p = \left(\mathbf{u}^T\mathbf{a} * \begin{pmatrix} 1 & 0 & 0 & 0 \\ 0 & 1 & 0 & 0 \\ 0 & 0 & 1 & 0 \\ 0 & 0 & 0 & 1 \end{pmatrix} - \mathbf{a}\mathbf{u}^T\right)\mathbf{x}_p \tag{2.4}$$

For the pin-hole-camera as well as for real cameras the focal distance f is known and estimated as the orthogonal distance $\mathbf{u}^T\mathbf{a}$ between the pin-hole $\mathbf{a}$ and the image-plane $\mathbf{u}$:

$$\mathbf{x}'_p = \mathbf{A}\mathbf{x}_p = \begin{pmatrix} f - an_1 & -an_2 & -an_3 & ad \\ -bn_1 & f - bn_2 & -bn_3 & bd \\ -cn_1 & -cn_2 & f - cn_3 & cd \\ -n_1 & -n_2 & -n_3 & f + d \end{pmatrix}\mathbf{x}_p \tag{2.5}$$

For the cameras coordinate system we assume that it is placed parallel the xy-plane, which corresponds to the normal vector $\mathbf{n} = (0, 0, 1, 0)$. The focal length f equals the

offset d of $\mathbf{u}$. Furthermore we place the pin-hole $\mathbf{a}$ into the origin $(0,0,0,1)$. By multiplication $\mathbf{A}$ by $1/f$ we get the affine transformation $\mathbf{A}_P HC$ for the pin-hole-camera (Equation 2.6). The camera-coordinates (u,v) are estimated by dividing $\mathbf{x}'_p$ by z'/f, so that $u = x'f/z'$ and $v = y'f/z'$.

$$\mathbf{x}'_p = \begin{pmatrix} u \\ v \\ f \\ 1 \end{pmatrix} = \begin{pmatrix} x' \\ y' \\ z' \\ z'/f \end{pmatrix} = \begin{pmatrix} 1 & 0 & 0 & 0 \\ 0 & 1 & 0 & 0 \\ 0 & 0 & 1 & 0 \\ 0 & 0 & 1/f & 0 \end{pmatrix} \begin{pmatrix} x \\ y \\ z \\ 1 \end{pmatrix} = \mathbf{A}_{PHC}\mathbf{x}_p \tag{2.6}$$

Figure 2.1a shows an example for the projection of the triangle with the coordinates $\mathbf{x}_a^T = (-1,-1,2,1)$ $\mathbf{x}_b^T(1,-1,2.5,1)$ $\mathbf{x}_c^T = (0,1,1.5,1)$ on the general image-plane tilted by 5° about the x-axis and the y-axis $\mathbf{u} = (sin(5^o), sin(5^o), 1 - sin^2(5^o), -2)$ and the projection point $\mathbf{a}^T = (1,0,-2,1)$. Figure 2.1b shows the same triangle $\mathbf{x}_a, \mathbf{x}_b, \mathbf{x}_c$ projected on the image plane $\mathbf{u} = (0,0,1,-2)$ of a pin-hole-camera with $d = -f = 2$ and the point of projection $\mathbf{a} = (0,0,0,1)$ equal with the origin of the camera coordinate system. The dashed line in Figure 2.1 is the normal $\mathbf{n}$ with the length of d.

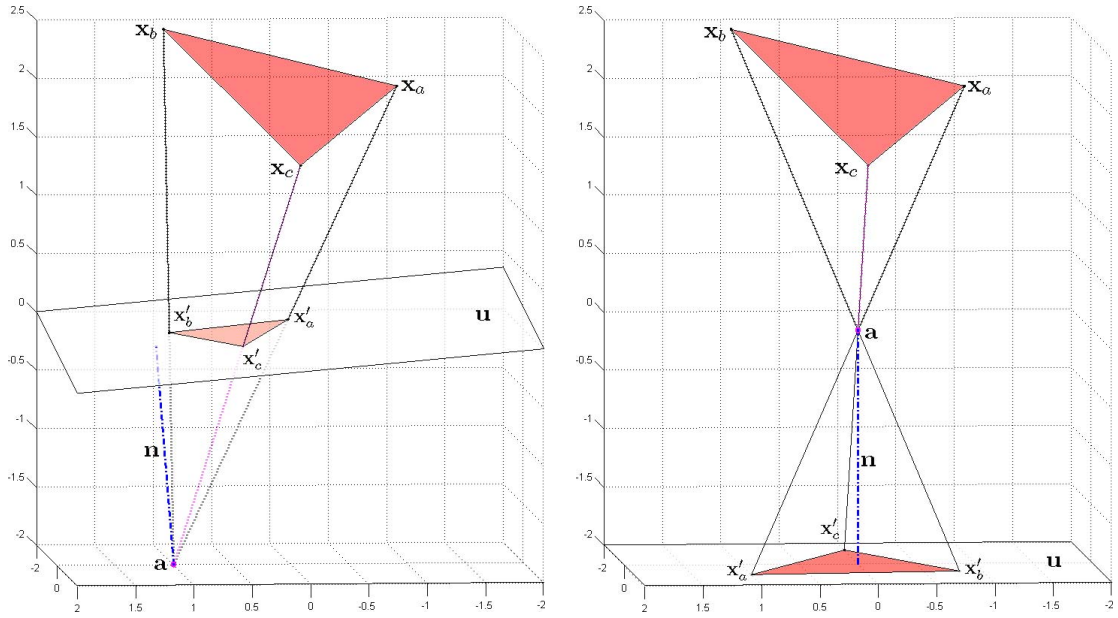

Figure 2.1: Projection of a triangle on an image-plane (a) in general and (b) for the pin-hole-camera.

Ray of Light

Is the position $\mathbf{k}^T = (k_x, k_y, k_z, 1)$ of a light-source emitting a single ray of light in the direction $\mathbf{d}^T = (d_x, d_y, d_z, 0)$ known, we can describe this line $\mathbf{G}_l$ by equation 2.7:

$$\mathbf{G}_l = \mathbf{k} + \lambda\mathbf{d} = \begin{pmatrix} k_x \\ k_y \\ k_z \\ 1 \end{pmatrix} + \lambda \begin{pmatrix} d_x \\ d_y \\ d_z \\ 0 \end{pmatrix} \tag{2.7}$$

The line $\mathbf{G}_l$ is projected by $\mathbf{A}_{PHC}$ into the image-plane $\mathbf{u}$ using equation 2.8:

$$\mathbf{G}'_l = \mathbf{A}_{PHC}\mathbf{G}_l \;\Rightarrow\; u = f\frac{k_x + \lambda d_x}{d_z + \lambda k_z}\;,\; v = f\frac{k_y + \lambda d_y}{d_z + \lambda k_z} \tag{2.8}$$

Equation 2.8 is transformed into Equation 2.9 to estimate λ of $\mathbf{G}_l$:

$$\lambda = \frac{fk_x - uk_z}{ud_z - fd_x} \;\vee\; \lambda = \frac{fk_y - vk_z}{vd_z - fd_y} \tag{2.9}$$

With Equation 2.10 and λ from Equation 2.9, we can estimate the coordinates of $x_{pi} = (x_{pix}, x_{piy}, x_{piz})^T$:

$$\mathbf{G}'_i = x'_{pi} + \lambda_i d_i = \begin{pmatrix} x'_{pix} \\ x'_{piy} \\ x'_{piz} \end{pmatrix} + \lambda \begin{pmatrix} d_{ix} \\ d_{iy} \\ d_{iz} \end{pmatrix}\;,\; d_i = a - x'_{pi} \tag{2.10}$$

Using the coordinates of $\mathbf{x}_{pi}$ we can estimate the orthogonal distance d_{piz} (also called depth) to the image-plane $\mathbf{u} = (u_1, u_2, u_3, u_4)^T$ by Equation 2.11. and the coordinates d_{pix} and d_{piy} of a parallel projection of p_{xi} into the image plane. The coordinates $(d_{pix}, d_{piy}, d_{piz})^T$ are called depth image or $2\frac{1}{2}$D-image.

$$d_{piz} = \frac{u_1 x_{pix} + u_2 x_{piy} + u_3 x_{piz} + u_4}{\sqrt{u_1^2 + u_2^2 + u_3^2}} \tag{2.11}$$

The parallel projected coordinates d_{pix} and d_{piy} in the coordinate system of $(\mathbf{u})$ with the parallel projection of a as origin is estimated by Equation 2.12. The vectors $\mathbf{n}_1 = (n_{11}, n_{12}, n_{13})^T$, $\mathbf{n}_2 = (n_{21}, n_{22}, n_{23})^T$ and $(u_1, u_2, u_3)^T$ are orthogonal to each other.

$$\begin{pmatrix} d_{pix} \\ d_{piy} \\ 0 \end{pmatrix} = \left(\begin{pmatrix} x_{pix} \\ x_{piy} \\ x_{piz} \end{pmatrix} - \begin{pmatrix} a \\ b \\ c \end{pmatrix} \right) \begin{pmatrix} n_{11} & n_{21} & u_1 \\ n_{12} & n_{22} & u_2 \\ n_{13} & n_{23} & u_3 \end{pmatrix} \tag{2.12}$$

Given the image-plane is parallel to the xy-plane ($\mathbf{u} = (0, 0, 1, u_4)^T$, $\mathbf{n}_1 = (1, 0, 0)^T$, $\mathbf{n}_2 = (0, 1, 0)^T$), d_{pix} and d_{piy} can be estimated by:

$$\begin{pmatrix} d_{pix} \\ d_{piy} \end{pmatrix} = \begin{pmatrix} x_{pix} \\ x_{piy} \end{pmatrix} - \begin{pmatrix} a \\ b \end{pmatrix} \tag{2.13}$$

Figure 2.2 shows two examples with the light-source $\mathbf{x}_{LS}^T = (1, 1, 2, 1)$ emitting the ray as line $\mathbf{G}_{l_i}$, $i = \{1, 2\}$. The line $\mathbf{G}_{l_i}$ intersects an object $\mathbf{p} = (0, 0, 1, 2)$ at the point $\mathbf{x}_{p_i}$, which is projected through $\mathbf{a}$ on the image-plane $\mathbf{u} = (0, 0, 1, -2)$.

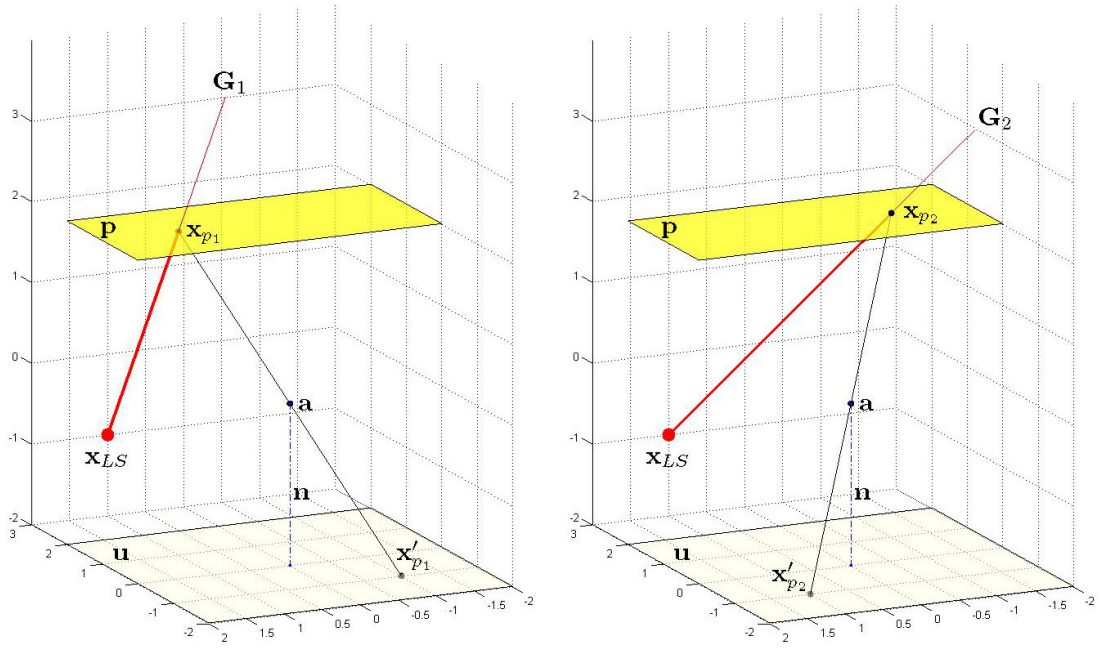

Figure 2.2: Projection $\mathbf{x}'_{p_i}$ on the image-plane $\mathbf{u}$ of the point of intersection $\mathbf{x}_{p_i}$ between the lines (a) $\mathbf{G}_1$, (b) $\mathbf{G}_2$ and an object $\mathbf{p}$ (plane).

Plane of Light

For better performance this triangulation can be enhanced (for example) by using a grid of points. Rather than projecting a grid of points we use a prismatic lens to split the ray of light into a plane [Lis99]. So we get an image of the line of intersection instead of the point of intersection. The world- coordinates of the points of the intersecting lines in the image can be estimated in the same way as for the single point, shown before. The same equation can be applied by using a well-defined movement, which can be a translation and/or rotation of the light source. This allows scanning of the surface of an object by acquisition of multiple images, when the laser line is moved over the object.

Figure 2.3 shows the projection $\mathbf{G}'_{pq}$ of the intersection $\mathbf{G}_{pq}$ between the plane of light $\mathbf{q}$ and an object (plane) $\mathbf{p}$. This figure is a combination of Figure 2.2a and Figure 2.2b, where two rays $\mathbf{G}_1$ and $\mathbf{G}_2$ are aligned within the plane $\mathbf{q}$.

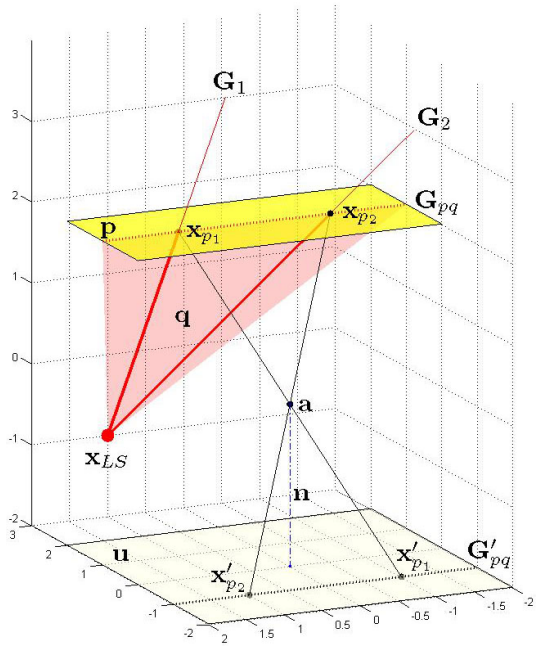

Figure 2.3: Projection of the line of points $\mathbf{G}'_{pq}$ of the intersection $\mathbf{G}_{pq}$ between the plane of light $\mathbf{q}$ and the plane $\mathbf{p}$.

The distance d_{zp} is estimated by Equation 2.11 using the coordinates of $\mathbf{x}_{pi}$. Similar d_{xp} and d_{yp} are estimated using Equation 2.12 or Equation 2.13. The difference between using a plane and a ray of light, is that the point $\mathbf{x}_{pi}$ is estimated by intersection of the inverse ray $\mathbf{G}'_j$ with the plane $\mathbf{q} = (q_1, q_2, q_3, q_4)^T$ at the point $\mathbf{x}_{pi}$. This is done by Equation 2.14 and Equation 2.15 for estimation of λ.

$$\mathbf{G}'_i = \mathbf{x}'_{pi} + \lambda_i \mathbf{d}_i = \begin{pmatrix} x'_{pix} \\ x'_{piy} \\ x'_{piz} \end{pmatrix} + \lambda \begin{pmatrix} d_{ix} \\ d_{iy} \\ d_{iz} \end{pmatrix} \ , \ \mathbf{d}_i = \mathbf{a} - \mathbf{x}'_{pi} \tag{2.14}$$

$$\lambda = \frac{q_1 x'_{pix} + q_2 x'_{piy} + q_3 x'_{piz} + q_4}{q_1 d_{ix} + q_2 d_{iy} + q_3 d_{iz}} \tag{2.15}$$

The result of the triangulation is the distances for each point (pixel) of the acquired image between the camera and the point on the object. This distance is called depth or range and therefore the images are called depth-images, range-images or $2\frac{1}{2}$D-images. To estimate the world-coordinates (3D-coordinates) the position of the camera in the world-coordinate system has to be added. Even when we now have 3D-coordinates of the surface of an object, we still have only a cloud of points that are not connected and these points do not describe the whole surface of an object. If for example one scan of a primitive object like a sphere is made, we would only get the points of one half of the sphere's surface.

Before we move on to the method of registration, we have to mention that our 3D-scanner consists of a real camera. In contrast to the pin-hole-camera, the images acquired by real world cameras have distortions from the lenses and position of the sensor. To remove this distortions the camera-system has to be calibrated to estimate the camera-parameters, which are used to equalize the images acquired. As the camera-parameters and the calibration is already integrated into our 3D-scanner, further information on the subject of camera-calibration can be found in [Tsa86, Rob96, Zha00].

2.1.3 From $2\frac{1}{2}$D-images to 3D-models

This section describes how we can achieve a virtually complete surface of an object using $2\frac{1}{2}$D-images. As described before, the system can measure only the sides of an object, which are acquired by the camera. To get a complete 3D-model you have to move the acquisition system around an object to acquire $2\frac{1}{2}$D-images of all sides of the object. These $2\frac{1}{2}$D-images must be merged in the world-coordinate-system. This merge is called registration [BM92].

In general the registration of $2\frac{1}{2}$D-images can be solved using three corresponding points. Finding these corresponding points automatically is generally not trivial. There are many registration algorithms making assumptions about the geometry of the object or acquisition system to overcome the problem of finding corresponding points [PVC+01]. Examples of such algorithms for registration of $2\frac{1}{2}$D-images are:

- Manual pin-pointing of three or more corresponding points [PVC+01].
- Registration using markers, which can be easily detected (e.g. spherical shape [CWK+01]).
- Feature based registration (e.g. [BDW+04]).
- Acquisition using well-known movement of the camera or object (e.g. using a turntable [Tos02]).
- Algorithms specialized for certain objects. (e.g: for fragments of rotationally symmetrically objects [KS99b]).

For our work the acquisition and registration is done by using the well-known movement of a turntable [Tos02], because sherds are thin objects and therefore no corresponding features or markers could be detected for registration of $2\frac{1}{2}$D-images. Manual pin-pointing has the same drawback, because no overlapping areas can be pin-pointed. To use the axis of rotation is not possible, because we have to process the data before we can estimate it (see Chapter 5). Because sherds are thin objects, we acquire at least two $2\frac{1}{2}$D-images of the sherds. One $2\frac{1}{2}$D-image is acquired of the inner side and the second $2\frac{1}{2}$D-image of the outer side of the sherd. Additional $2\frac{1}{2}$D-images can be acquired for sherds with decorations introducing shadowing effects, because we can only acquire surfaces seen by the camera and intersected by the laser-plane. The scheme of our setup consisting of a 3D-scanner and a turntable are shown in Figure 2.4.

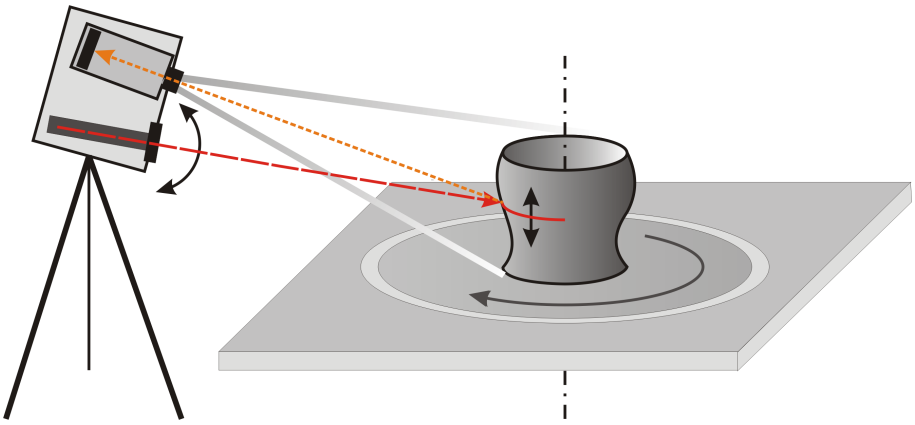

Figure 2.4: Scheme for 3D-acquisition based on a moving light plane using a laser and a prism. Left: 3D-scanner consisting of a camera (top) and laser enhanced by a prism (bottom) to a plane. Right: Turntable with acquired object. The rotational axis of the turntable is shown as dashed-dotted line. The movement of the laser plane (dashed line) and its intersection with the object is shown as double-arrows. The projection of the intersection to the camera's sensor is shown as dotted line.

Concluding this section, we have shown the principle of 3D-acquisition. Therefore we use equations e.g. for intersections of lines and planes, which are used in the following chapter for estimation of the rotational axis and processing of the sherds.

2.2 Archaeological Terms

Archaeology uses several terms which will be explained in this section, because some terms have a special meaning, which may not agree with the terms of computer-science. For example: Pottery is considered as complete in archaeology, when a sherd of an object exists, which allows the drawing of a complete profile line. As the written history can be changed by single finds, it is often difficult to find a ground truth in archaeology and therefore the definition of rules for documentation and classification is not always straight forward and fuzzy terms like "can", "might', etc. are used.

The profile line is defined as the longest elongation that can be drawn around the wall of a sherd parallel to the axis of symmetry. The axis of symmetry is the axis through the center of an object, when it is orientated in its upright position. As ceramics were manufactured on rotational plates for thousands of years, the axis of symmetry is virtually identical to the axis of rotation. There also exist ceramics, which have not been produced on rotational plates, but as these finds are rare in comparison to the tens of thousands of daily finds, we will use the term rotational axis in this thesis.

The maximum height of a sherd is estimated parallel to the axis of rotation between the highest and lowest point. As the maximum height corresponds to the profile line and the maximum and minmum point need not be co-planar with the axis of rotation, the drawn profile line can be constructed out of two or multiple profile lines. The use of multiple profile lines to construct the longest profile line is required only for rare sherds with large and complex fracture.

2.2.1 Types of Sherds & Characteristic Points

Archaeologists distinguish between regular finds and special finds. Regular finds are ceramics of daily use and therefore tens of thousands are found. Special finds are rare or unique ceramics, which generally belonged to rich and important people. As we want to help archaeologists with their daily finds, we focus on the processing of regular finds. As the principle of documentation of special finds is identical, our system can also assist the archaeologist by providing a profile line, but manual interaction, like adding a special description is required.

In case of regular ceramics, the profile line is generally drawn only for rim-fragments. The rim-fragments are fragments of the upper part of an object, which contain the *lip* of the orifice. Therefore the plane that touches the lip tangentially is called orifice-plane. Analogical there exists a bottom- plane for sherds from the bottom, where a profile line is drawn, if the bottom contains special features like applications supporting the vessel.

The rim-fragments have the highest priority for documentation, because these fragments contain most of the information required by archaeologists for further analysis like classification and interpretation. This information is given by the characteristic points

of the profile line, which are shown in Figure 2.5. This example for characteristic points shown are the inflection points (IP), local maxima (MA), local minima (MI), the outermost point, where the profile line touches the orifice plane (OP), the outermost point, where the profile line touches the base plane (BP) and the point, where the profile line touches the axis of rotation.

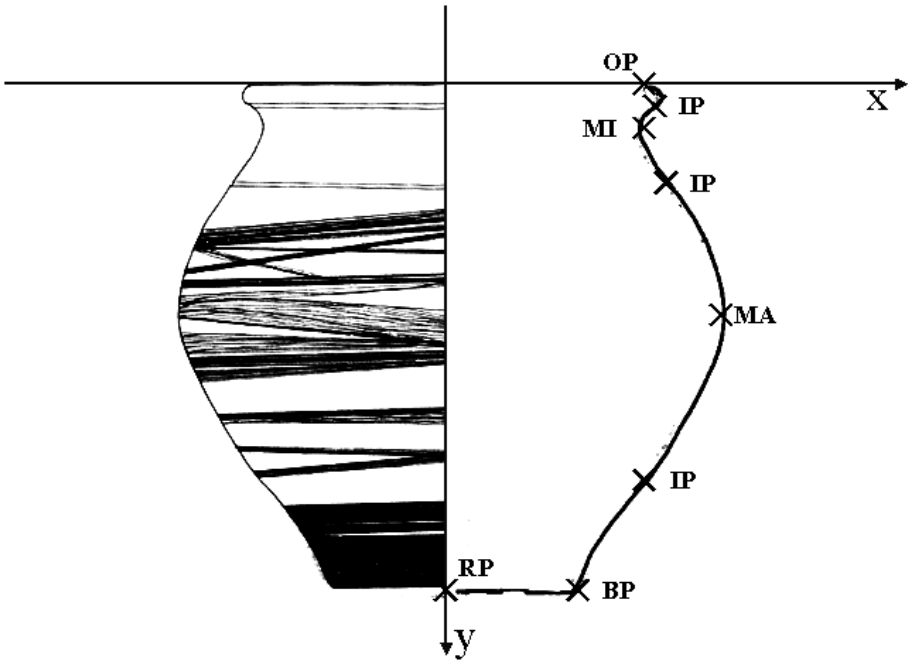

Figure 2.5: Characteristic points of a complete vessel.

Optionally archaeologists draw a view of the top of a rim-fragment, because these are often decorated by patterns of scratches (called rills) in the surface. These patterns can be significant for detailed classification of pottery.

Beside the wall-fragments, which are virtually never documented, the bottom-fragments are only drawn, if they contain rings or feet that support the object. Furthermore objects may have so-called applications, like handles, relieves, or other small decorations which can disturb the symmetry of an object.

2.2.2 Classification

Ceramics found on an excavation are separated into different classes. The main classification is the time-period (e.g. bronze-age, iron-age, etc.) a ceramic belongs to. Furthermore the region and/or culture is classified (e.g roman, germanic, cypriot, etc.). Afterwards the ceramics are divided into sub-classes, which generally describe the type of ceramic (e.g. plate, bowl, jar, etc.). Depending on the level of detail of the archaeological documentation, the type of ceramic is further diveded into variations of types, which are generally

numbered. As the type of ceramic can change constantly over decades it is also possible that a range of types is given as class.

Table 2.2 and Table 2.3 show an example of basic classification of late roman burnish ware of Carnuntum in reference to [Grü79]. The abbreviations used are:

- b breadth or width of vessel (maximum)
- bdm belly-diameter (maximum)
- $bodm$ bottom-diameter
- CP corner point (abrupt inconstancy resp. inflection)
- rdm rim-diameter
- h heighth of vessel (maximum)
- IP inflection point
- MA local maximum point with vertical tangency
- x-values ... x-coordinates of the profile line sorted descending by height (y-coordinate).

basic vessel form	characteristic ratio $(+/-15\%)$	absolute rdm	absolute bdm
plate	$h : rdm = 1 : 8$	$16 - 34\ cm$	n.a.
bowl	$h : rdm = 1 : 2 \ldots 1 : 4$	$10 - 16\ cm$ (bowl 1-2) $12 - 30\ cm$ (bowl 3-7)	n.a.
beaker	$h : rdm = 1 : 1$	$4 - 10\ cm$	$5 - 14\ cm$
jug	$h : rdm = 4 : 1 \ldots 2 : 1$ with handle	n.a.	n.a.
pot	$h : rdm = 1 : 1 \ldots 3 : 1$	$8 - 12\ cm$ (pot 1) $12 - 16\ cm$ (pot 2)	$15 - 25\ cm$ (pot 1) $18 - 21\ cm$ (pot 2)

Table 2.2: Example: classification of late roman burnish ware of Carnuntum into basic vessl groups.

The basic forms from Table 2.2 can be sub-divided into main types shown in Table 2.3. Table 2.3 also includes the common german type name, because in contrast to informatics german is, besidea spanish and french, a traditional language in archaeology.

vessel type	Common type name	characteristics in curvature	Notes	references to [Grü79]
Beaker 1	Becher	No IP No CP	only steady or decreasing x-values	78/1-4, ...
Beaker 2	Henkel-becher	IP	s-shaped with handle	78/6, ...
Bowl 1-2	Schale	No IP No CP	only steady or decreasing x-values	70/1-6, 71/2
Bowl 3-7	Knickwand-schüssel	CP	only steady or decreasing x-values	72/5-8, 73/1-3 74/4,6-8, ...
Pot 1	Hoher, bauchiger Topf	IP	s-shaped, bulgy $rdm << bdm$	79/2, 81/2
Pot 2	Gedrungener, bauchiger Topf	IP	s-shaped, bulgy	79/1-3
Plate 1-2	Teller	No IP No CP	only decreasing x-values	71/1-9, 75/1-4

Table 2.3: Example: sub-classes of late roman burnish ware of carnuntum.

2.3 Summary

In the first part of this chapter we have shown the principle of 3D-acquisition using structured light to acquire a $2\frac{1}{2}$D-image of an object. To show this principle we use Homogenous coordinates and affine transformations required for the next Chapters. The second part of this chapter described archaeological terms and the importance of the profile line and its use for archaeological classification to understand the importance of the profile line and therefore its correct orientation using the axis of rotation.

Chapter 3

Data Acquisition

The following section describes the setup for acquisition of sherds using a 3D-scanner and an immediate improvement made for our system during our field-trip. As the 3D-scanner was not the only acquisition system at the field-trip, we show acquisition of sherds using a competing system, called *Profilograph*. Both systems were compared to the manual drawings. Therefore we show the acquisition and processing of manual drawings. For each system at the end of each section the data format required for further processing and comparing the systems is described. Finally this chapter is concluded with a summary.

3.1 Competing Systems on the Field-Trip

For our practical experiments we joined the excavation in *Tel Dor* for a four week campaign. The main goal of the practical experiments was to test our method and compare the three documentation systems. Therefore we brought the 3D-scanner of the *Innovative Project 3D-Technologies* of the Vienna University of Technology (*TU, Wien*) and the *Profilograph* to the excavation, where sherds are still drawn manually.

Besides the 550 3D-scans of sherds and other finds (e.g. columns, figures, etc.), the archaeologists choose 25 different sherds for comparison of the three ways of documentation. The criteria of the archaeologists for choosing these samples were to see where each method has its limits. The comparison was done using the estimated profile lines of all three ways of documentation and is shown in Chapter 6, while this Chapter focuses on the acquisition of the data for this comparison.

Regarding performance measurements we used additional sherds which were brought from the excavation to the pottery registration office to gather a representative selection of routine data. For acquisition of sherds with respect to performance, which is measured in sherds per hour, we trained a student, without archaeological, computer science or 3D-scanning expert knowledge. The same was done for the *Profilograph*. The manual drawings have been made by a draftsperson with more than ten years of experience, because manual drawing requires several weeks of training and expert-knowledge for proper archaeological documentation of the finds.

3.2 3D-Scanner

3D-scanners using structured light have been existing for more than ten years [SMD91]. Meanwhile 3D-scanners are used for industrial and medical applications and therefore they got available as products "off-the- shelf". Regarding size and weight, we choose such a product to join field-trips and test our methods in practical experiments. The chosen 3D-scanner is produced by *Konica-Minolta* and the model used for this thesis is called *Vi-900*.

The camera of the *Vi-900* is high-speed CCD camera achieving $\frac{1}{2}$D-acquisition between 0.5 and 2.5 seconds. The resolution of the CCD sensor is 640×480 pixels. The resolution is given by *Konica-Minolta* as $\pm 0.2\ mm$ in x, y-direction and $\pm 0.1\ mm$ in z-direction (depth). The reason for the better resolution of the depth compared with the resolution of x, y is, that the resolution of the depth depends only on the precision of the triangulation, while the resolution of x, y can only be increased by having a sensor with a higher resolution. As the camera has an interchangeable lens- system, the given resolution is achieved using the camera with the "Tele"-lens having a focal length f of $25\,mm$. This resolution decreases for a maximum of a factor of ≈ 4 for the "Wide"-lens ($f = 8\ mm$). The third lens provided with the scanner is the "Middle"-lens having $f = 14\ mm$.

The emitted laser power is eye-safe ("Class-2 - IEC 60825-1"). The laser beam is splitted into a laser-plane using a prism as shown in the previous Chapter. This laser-plane is translated using a galvanometer-driven mirror [CRB+02, MGI04], which is also responsible for the precision of the triangulation. The working distance between the 3D-scanner and an object has to be within 600 mm and 1200 mm. The acquired volume depends on this working distance and the type of lens as shown in Table 3.1.

Lens Type	$min(X)$ mm	$max(X)$ mm	$min(Y)$ mm	$max(Y)$ mm	$min(Z)$ mm	$max(Z)$ mm
"Tele"	111	463	83	347	40	500
"Middle"	198	823	148	618	70	800
"Wide"	359	1196	269	897	110	750

Table 3.1: Dimensions of the bounding of the volume acquired by the *Konica-Minolta Vi-900* 3D-scanner depending on the minimum (600 mm) and maximum (1200 mm) working distance.

For our work, the 3D-scanner has been set up to scan sherds of small ($4 \times 3\ cm$) to large size ($27 \times 20\ cm$). Therefore we have chosen the "Middle"-lens and a working distance of 750 mm. The acquisition of the sherds has been done using an *ISEL RF-1* rotational plate with a stepping motor. The angular resolution of this rotational plate is 0.017°. The acquisition was generally done by using a stepping angle of 180° to acquire the inner and outer side. For decorated sherds an additional $2\frac{1}{2}$D-image was required and therefore a stepping angle of 120° was chosen to acquire one $2\frac{1}{2}$D-image of the inner side and two $2\frac{1}{2}$D-images of the outer, decorated side. Decorations of the inner side never required an

additional $2\frac{1}{2}$D-image during our experiments. The points of the $2\frac{1}{2}$D-image are registered using the known position of each image given by the rotational plate. The Iterative closest Point (ICP) Algorithm [BM92, CM92] is used to register the vertices to a connected surface.

Figure 3.1 shows this setup with such a sherd. There also exist sherds of even smaller and larger size, but these are not representative for daily finds, because very small ones are generally not documented. Sherds of large size may be complete vessels in respect to archaeological terms or special finds, which were not a topic of our investigation.

(a) (b)

Figure 3.1: (a) Setup of the 3D-scanner (rectangle) and the rotational plate with an acquired sherd (ellipse). The lower arrow shows the direction of the laser plane. The upper arrow shows the projection of the intersection of the laser beam towards the camera. (b) View of the setup in the direction of the field of view of the 3D-scanner.

During the acquisition of sherds in the first two weeks of our field-trip, we always measured the time for documentation per sherd and consequently we also measured the time for the single steps of documenting a sherd by 3D-acquisition. Therefore we could break down the work into the following steps.

1. Mounting a sherd on the rotational plate using white plasticine.
2. 3D-acquisition including the movement of the rotational plate.
3. Transfer of Data between the 3D-scanner and the computer.
4. Manual inspection of the 3D-model.
5. Entering the finding number as file name for the 3D-model.
6. Estimation of the rotational axis and the profile line.

The overall time required for all of these steps were approximately 6 minutes. The most time consuming steps were steps 2, 3 and 6, which required 80% of the time (4 : 45 minutes). The time for step 6 (2 minutes) could be saved by processing the data in parallel on a second computer or by processing the data after working hours, when the computer for 3D-acquisition was not in use.

The remaining steps 2 and 3 for acquisition and data-transfer required times between 3 : 00 and 3 : 30 minutes. This shows that due to mechanical movement of the system (laser, optics and turntable), the overhead for the data-transfer and the size of the acquired sherd influences the time required for acquisition by less than 17%.

On the other hand the scanner always requires a certain volume, because the geometry and the optics have not been optimized for maximum resolution for each 3D-acquisition. This was done because the resolution of less than 0.3 mm for an unoptimized setup is sufficient for archaeological documentation.

3.2.1 Acquisition of Multiple Sherds

This has lead to the idea of enhancing the acquisition system by acquisition of multiple sherds at one time. Therefore we built a frame, whereupon we mounted eight clamps for mounting sherds. The frame and the clamps have been covered with black-mate paint, which can not be acquired by the 3D-scanner. The size of the frame was 20×30 cm and in practical experiments we could mount up to five or six sherds, as shown in Figure 3.2.

(a) (b)

Figure 3.2: (a) Frontview and (b) Backview of the sherds mounted in a frame with clasps for increase the acquisition of sherds per hour.

Using this frame we could increase the rate of acquired sherds from a maximum of 20 sherds per hour to 40 sherds per hour. As we can see, using such a frame can not increase the performance by a factor equal the number of clamps used, because larger

sherds require more space and mounting the sherd requires time also. A further enhancement would be to have multiple frames in different sizes, which can be filled with sherds while one frame is acquired. A further benefit of the frame is, that it can be used without the rotational plate, because it can be registered automatically by use of the frame itself as registration-target (also called marker) or by addition of markers like spheres.

Figure 3.3 shows two registered images of sherds acquired with the frame. We can see that even by using of black-mate color some parts of the frame are acquired, which can be easily detected by its color and size like other noise. Furthermore it must also be mentioned that the frame is not suitable for acquisition of special finds, because a part of the sherd is covered by the clamp and therefore missing in the 3D-model. This is not of concern for estimation of the profile line as long as the clamp does not cover parts of the longest profile line.

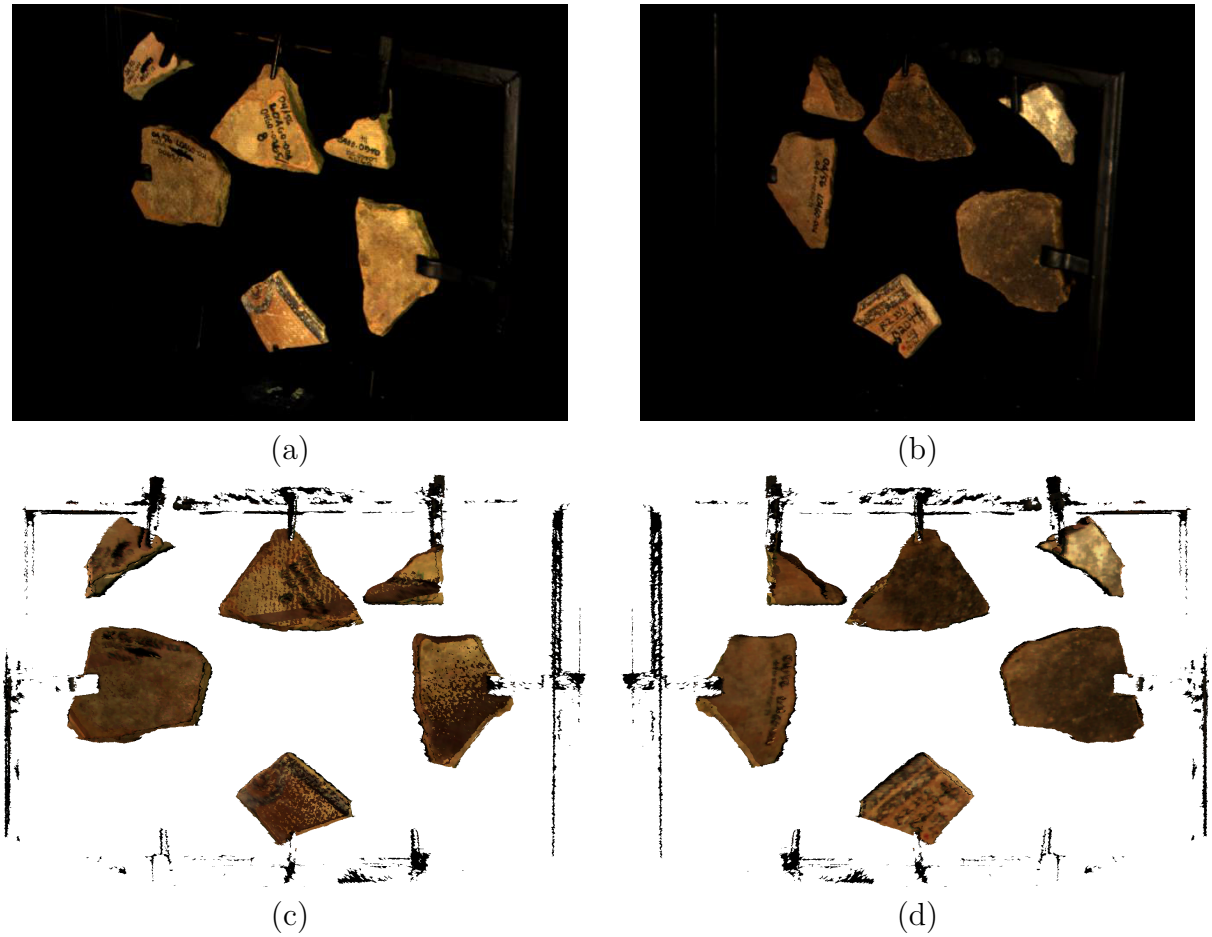

Figure 3.3: Image of the (a) frontside and (b) backside acquired by the camera of the 3D-scanner. (c) Frontview and (d) backview of the 3D-model.

The next section shows the data-structure used for storage and processing the acquired 3D-models.

3.2.2 Data Structure: 3D-Surface & Profile Line

As shown in Figure 3.3 even the $2\frac{1}{2}$D-images are vertices connected to triangles together with color information. The color information is acquired by using a color wheel after the $2\frac{1}{2}$D-image has been estimated. Therefore we get also the *R*ed, *G*reen and *B*lue values of a point (vertex) of a surface. For storage of the acquired $2\frac{1}{2}$D-images we choose a simple file format using a list for vertices and triangles. Therefore we choose *Alias™Wavefront Object ASCII* to describe the surface of the acquired sherds by polygons. This is done by a list of vertices prefixed by a `v`, followed by the x-, y- and z-coordinate and the color-values $R, G, B = \{0, ..., 255\}$ A polygon is prefixed by an `f` and followed by the indices to the vertices. Comments are prefixed by a `#`. Figure 3.4 example shows a simple triangle, with two yellow vertices and one violet vertex, defined by:

```
# Simple Wavefront file
# Vertices:
#   x   y   z    R   G   B
v 0.0 0.0 0.0  255 255   0
v 1.0 0.0 1.0  255 255   0
v 0.0 1.5 1.5  255   0 255
# Triangle:
f 1 2 3
```

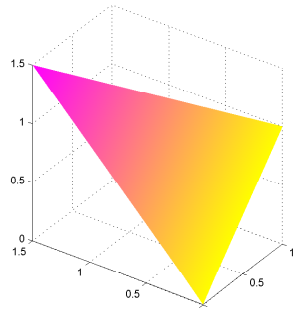

Figure 3.4: Triangle defined by an *Alias™Wavefront Object ASCII* file.

There also exist other file formats, like the freely available *VRML* specification, which has been used in previous work [Mar03, MK03]. We changed to *Alias™Wavefront Object ASCII*, because its specification is also freely available and can be converted to other file formats like *VRML*, by minimal adaption of the file structure (e.g. file header, line-prefixes).

Using this 3D-model the profile line is estimated as shown in the next two Chapters. This profile line is an ordered list of x, y-coordinates, where x equals the radius and y equals the height of a profile lines.

3.3 *Profilograph*

The *Profilograph* is manufactured by *Dolmazon Vermessungstechnik & Computerdokumentationen* in Heidelberg, Germany. It is a pin-pointing-system related to the computer-human interface device *mouse*. Therefore it can estimate the x and y-coordinate of the pointer and the z-coordinate by moving the pointer vertically along an electric resistor. The value of resistance corresponds to z. When the pointer touches the surface the x, y and z coordinate are transmitted to a computer.

In theory the surface of a sherd could be acquired point by point resulting in a 3D-model like acquired by the 3D-scanner. Due to requirements of archaeologists and the amount of time ($\approx$ 10 points per minute) for such an acquisition this is not practicable, because only the profile line is needed. The acquisition of tens of thousands of points of the complete surface would require several hours of work. As our experiments in respect to performance have shown, the acquisition of a profile line consisting typically of 80 to 150 points requires between 10 and 15 minutes of working time.

To save working time only points along the surface parallel to its supposed rotational axis are acquired. The location where these points are acquired is chosen at the point where the sherd has its maximum height, which generally results in the longest profile line. In case of a complicated fracture two or more profile lines are extracted and merged to get a virtual longest profile line. For acquisition with the *Profilograph* the orientation has to be determined manually and it has to be mounted into the *Profilograph* using the manual orientation.

3.3.1 Estimation of the Radius

As this acquisition of the profile line results in a correct shape and orientation, no information about the radii can be estimated. Therefore points on the inner and outer side of the sherds vertical to the profile line are acquired. These two lines of the inner and outer side describe an arc, which is part of a circle, when the sherd has been (manually) orientated properly.

Figure 3.5 shows the profile line and the horizontal profile line of the inner and outer side. The horizontal profile lines are shown as arcs. Into these arcs, circles are fitted minimizing the least-square error [GGS94].

As the horizontal profile lines are extracted along the middle of the sherds height the average radii of the inner and outer side is applied as offset for the radii of the center of gravity of the profile. In case of sherds with sharp corner edges at the rim, the horizontal profile lines can also be measured along these corners, but then the radii of the profile line have to be adapted manually.

Furthermore Figure 3.5b shows that the two matched circles are not perfectly concentric. Therefore the distance between the circle centers d_{pc12} is used as measurement of error for the manual orientation of the sherd, when it was mounted into the *Profilograph*.

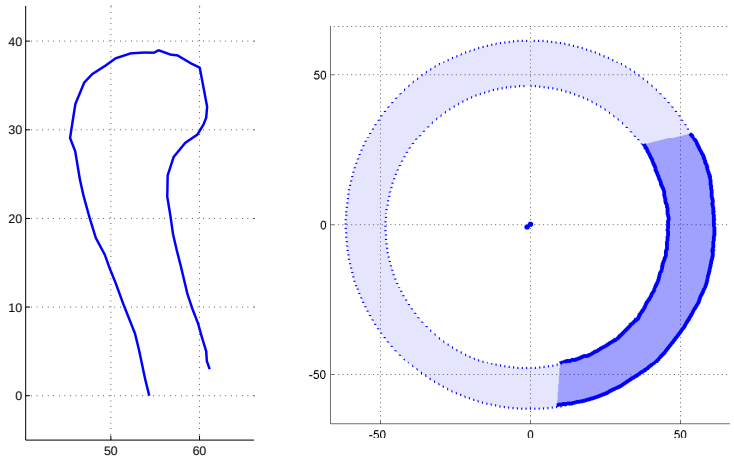

(a) (b)

Figure 3.5: (a) Profile line orientated manually and acquired by the *Profilograph*. (b) Horizontal profile line of the inner and outer side (continuous arcs) and the fitted circles (dotted line) of sherd D2-L19720-305925-12.

3.3.2 Profile Lines as Polylines

As the profilograph is designed as a human interface device for *C*omputer *A*ided *D*esign (*CAD*) software, the data is stored as *Autodesk AutoCAD Release 12 DXF* file, which is an *ASCII* file, similar to the *Alias Wavefront Object* and shown below. The profile lines are stored as 2D polygons, which is a sorted list of x and z coordinates for the profile line and x and y coordinates for the two horizontal profile lines. These *DXF* files have been parsed by using a *MathWorks Inc., Matlab* script. Therefore only the lines after the tags `10`, `20` and `30` are read and stored as x, y and z-coordinates. As these lines are two dimensional ($z = 0$) this coordinate is ignored. Because a *DXF* file contains two profile lines for the horizontal intersection, the coordinates are seperated using the tag `POLYLINE`. The result are two profile lines for estimation of the radius and one profile line having x, y-coordinates like the profile lines from the 3D-scanner.

```
# ... Header (skipped) ...
POLYLINE
# ... Offset (skipped, because it is always zero) ...
VERTEX
  5   # Vertex Index
46    # 46 (Hexadecimal)
  8
0
 10   # x-coordinate (prefix 10):
328.09817240216353
 20   # y-coordinate (prefix 20):
205.69893655420441
 30   # z-coordinate (prefix 30):
0.0
  0
# ... List of Vertices  ...
SEQEND # Suffix
```

3.4 Digitizing Manual Drawings

For the manual drawings tools like sliding calliper, ruler and circle templates are used to draw the profile line of sherds with pencil on scale paper. Due to concerns about printing an archaeological documentation, the sherds acquired for our experiments have been drawn in a scale of $1 : 2$. As the pencil drawings on scale paper are not suitable for reproduction, the drawings are transferred to transparent paper and afterwards manually traced by black ink. Also the profile line is filled with black ink resulting in the profile typically found in archaeological publications.

For our experiments, we acquired a gray-level image of the profile line on the transparent paper before it has been inked, to prevent further noise introduced by tracing the profile line with ink. Therefore a *Canon LiDE-50* flat bed scanner with a maximum resolution of 1200 dots per inch (DPI) has been used. As archaeological measurements are given with a resolution of 0.1 mm and the scaling factor of $1 : 2$, we require at least a resolution of 40 points per mm (102 DPI) (Shannon's Theorem [Sha48]). Therefore we choose the next finest resolution of 300 DPI, due to the operating software of the scanner, to digitize the profile lines.

After the image has been digitized, it is processed by the following steps to gather a profile line for comparison with the *Profilograph* and the 3D-scanner. Figure 3.6 shows the gray-level image of a manual profile line of sherd D2-L19720-305925-12.

1. Estimation of a binary image by application of a threshold ($> 63\%$ level of gray).
2. Estimation of the bounding box of all black pixels.
3. Trim of the image by use of the bounding box.
4. Removal of the left half of the image (outer view of the ceramic).
5. Labeling and removal of horizontal and vertical lines detected by the ratio of their bounding box ($width : height >> 10 : 1 \vee 1 : 10$).
6. As the rotational axis and the orifice plane appear as connected horizontal and vertical line, their bounding box is less than 80% of the image size and their area cover less than 3% of the bounding box, these two line are removed using these properties.
7. Removal of noise (labeled areas less than 20 pixels).
8. Thinning of the remaining profile line to a width of one pixel.
9. Connection of the pixels by their 8-point neighborhood.
10. Conversion of the image coordinates into real-world coordinates using the resolution of the 2D-scanner and the drawing scale.

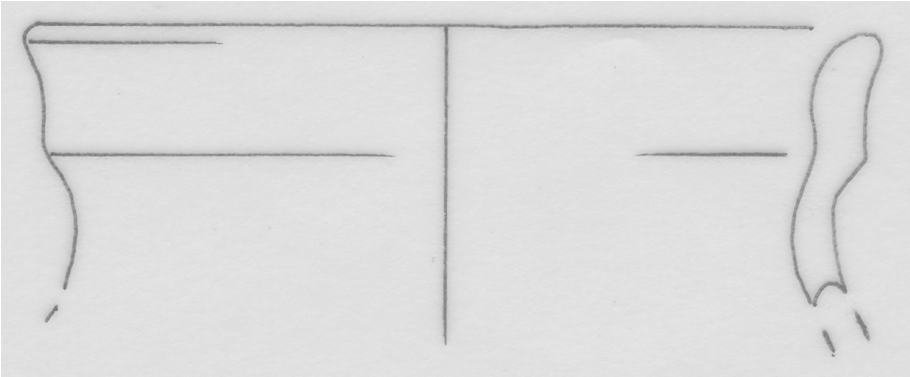

Figure 3.6: Gray level image of the manually drawn profile line of sherd D2-L19720-305925-12.

Figure 3.7a shows the labeled image after step 4. The detected lines of the rotational axis and the orifice plane (dark gray), lines (medium gray) and the noise (light gray) are shown. Figure 3.7b shows the profile line after step 7. The gray area shown is actually white (empty) pixels, which are required to maintain the correct radii in step 9. The final profile line with real-world coordinates are shown in Figure 3.7c. The x-axis shows the radius and y-axis the height of the sherd. Therefore the profile line is represented as sorted list of x and y coordinates like the profile lines estimated by the *Profilograph* and the 3D-scanner.

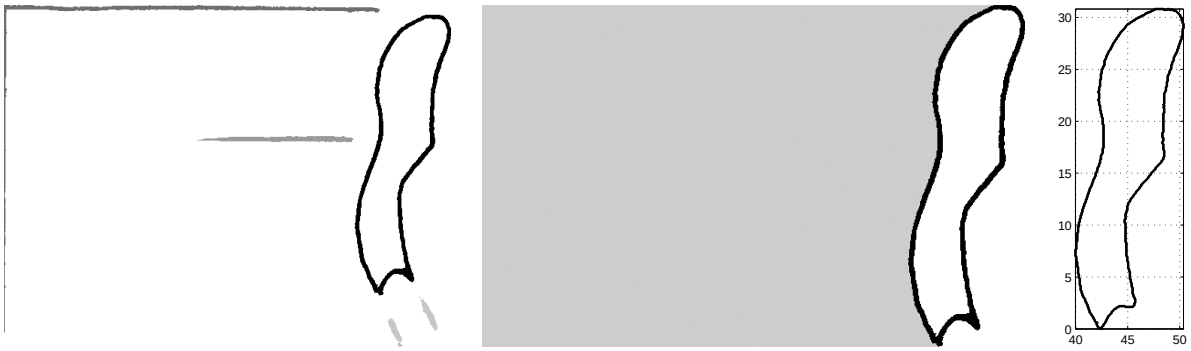

(a) (b) (c)

Figure 3.7: (a) Labeled image: The gray colored labels are removed. The black colored label is the (b) remaining profile line with white-space (shown in gray) for maintaining the radii. (c) Profile line with real-world coordinates The radii are shown on the x-axis and the height on the y-axis in mm.

3.5 Summary

Concluding this chapter, we have shown the setup of the 3D-scanner for acquisition of sherds including a performance related improvement. Then the acquisition using the *Profilograph* was shown including the estimation of the profile lines with this device. Finally we have shown the acquisition and processing of manually drawn profile lines using a flat bed scanner. Furthermore we have shown the data-structures for storing and comparing the 3D-models and the profile lines of the 3D-scanner, *Profilograph* and from the digitized manual drawing. The next chapter shows the estimation of the rotational axis, which is required to estimate the profile line using a 3D-model.

Chapter 4

Rotational Axis

Regardless of the system used, the orientation of a sherd is the essential part of the documentation. Therefore this chapter shows how orientation is done by estimation of the rotational axis. First an overview about related methods and previous work is given. Then our new method inspired by the manual methods used by archaeologists is shown and evaluated with synthetic data. This evaluation includes real sherds from a real, well-known vessel, which is compared with the manual method. Finally the chapter is concluded with a summary.

4.1 Aproaches for Rotationally, Symmetric Surfaces

The oldest and well approved approach for orientation is the manual method used by archaeologists for several decades. This manual approach is based on the production process of ceramics, because ceramics have been produced on rotational plates for thousands of years. Therefore ceramics have a rotational axis, which is also called axis of symmetry. This rotational axis is present for fragments of ceramics (sherds). The manual method of finding the orientation of sherds is generally applied on sherds containing a part of the rim or the bottom. As sherds are found in tens of thousands, the remaining sherds from the walls of vessels are not documented, because their manual orientation is more difficult and time consuming. Furthermore the gain of information of the sherds from the wall is minimal, because they generally contain only one or two characteristic points, which is not sufficient for classification. The manual method uses a plane with circle templates (Figure 1.4b), which is aligned along the rim. This plane is also called orifice plane. Therefore the rotational axis is estimated orthogonal to the orifice plane and by the center of the circle templates. The same method is also used for the sherds from the bottom.

The method of using orifice-plane for orientation has been implemented by the Department *Lenguajes y Sistemas Informaticos* of the Granda University. This system also uses a 3D-scanner for acquisition. For orientation, the rim has to be approximated manually by pin-pointing. Afterwards the rotational axis is estimated using the circle arc of the rim [MLCT03]. Therefore the drawbacks of this system are the required manual

interaction, which requires expensive working time of experts. Furthermore sherds with a decorated or damaged rim can not be processed, because for such fragments no arc can be found for axis estimation.

Another novel method for finding the axis of rotation is the approach by Pottmann and Randrup [PR98]. This method has been designed to estimate the rotational axis for rotational and helical surface based on line geometry [PW01] using Plücker coordinates [Plü68]. It has been well tested and used for different applications [PPR99]. The drawback for this method is, that it has been designed for complete surfaces and therefore its application to sherds is not suitable [Lau01, CM02].

There exists an alternative method [CM02], which is based on the idea of tracing normal vectors towards the rotational axis. This approach is similar to previous work [Kam03], which uses a Hough-inspired method [YM97] and an accumulator space. Therefore the normal vectors are traced through the accumulator space. For each trace the weight of the intersected voxels of the accumulator space is increased. In theory the weights of the voxels should increase towards the rotational axis, which is determined by use of the Principal Component Analysis (*PCA*) [DKK96, Jol02].

Due to our experiments on the field-trip we have noticed that the method of finding the axis of rotation by the normal vectors fails for S-shaped objects and for coarse ware. The reasons for these failures are the shape and the noise.

4.2 Normal Vectors for Axis Estimation

The principle of the normal vectors pointing towards the rotational axis is shown in Figure 4.1. This figure shows two synthetic fragments of rotationally symmetric objects, with their normal vectors and their axis of rotation. The synthetic data used for the following experiment is the same as used for experiments with our new method. The properties of this synthetic data are described in Section 4.5.

For our experiments using normal vectors for axis estimation we used our smooth synthetic objects, which contain only the quantization error. Facing this quantization error, which is less than the error expected from our 3D-scanner, the assumption, that the normal vectors intersect at the rotational axis, is no longer valid. Therefore we have to assume that the distance between normal vectors have a minimum near the rotational axis. Therefore the first experiment was to estimate the minimum distance ρ an between pairs of normal vectors (skew lines) $\mathbf{n}_i = \mathbf{k}_i + \lambda \mathbf{d}_i$ and $\mathbf{n}_j = \mathbf{k}_j + \lambda \mathbf{d}_j$. The minimum distance ρ its location $\mathbf{v}_{ij}$ is estimated with the following equations [Cou79]:

$$\rho = (\mathbf{d}_j - \mathbf{d}_i) \frac{\mathbf{n}_i \times \mathbf{n}_j}{|\mathbf{n}_i \times \mathbf{n}_j|} \tag{4.1}$$

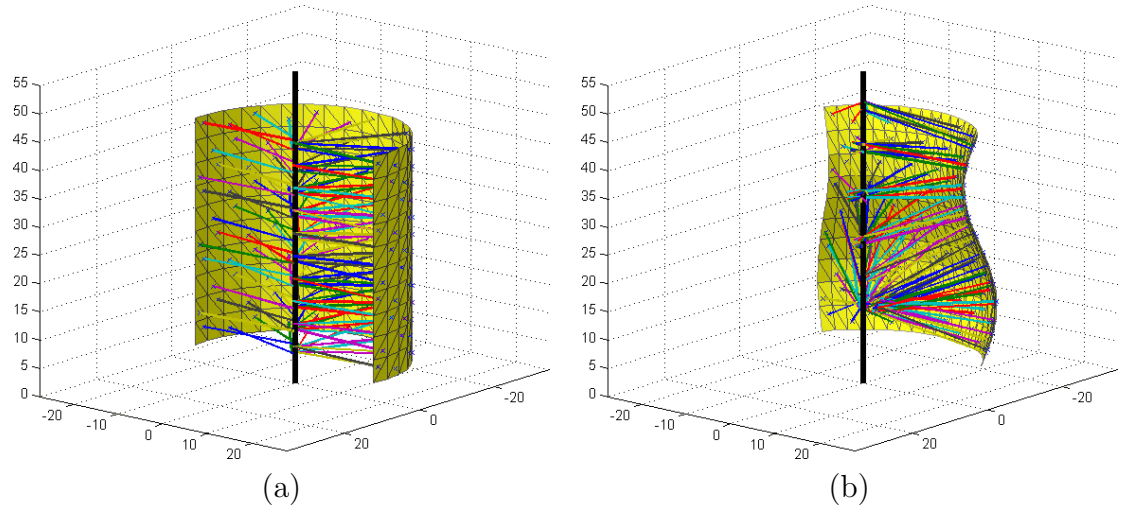

Figure 4.1: Fragments of synthetic, rotationally symmetric objects for experiments. Fragment of (a) a Cylinder and (b) a s-shaped object, similar to certain ceramics (e.g. vase).

$$\mathbf{v}_{ij} = \mathbf{v}_i + \frac{\mathbf{v}_j - \mathbf{v}_i}{2},$$

$$\mathbf{v}_i = \mathbf{k}_i + \lambda_i \mathbf{d}_i, \mathbf{v}_j = \mathbf{k}_j + \lambda_j \mathbf{d}_i,$$

$$\mathbf{k}_{ij} = \mathbf{k}_i - \mathbf{k}_j,$$

$$\lambda_i = \frac{(\mathbf{k}_{ij}\mathbf{d}_j^T)(\mathbf{d}_j\mathbf{d}_i^T) - (\mathbf{k}_{ij}\mathbf{d}_i^T)(\mathbf{d}_j\mathbf{d}_j^T)}{(\mathbf{d}_i\mathbf{d}_i^T)(\mathbf{d}_j\mathbf{d}_j^T) - (\mathbf{d}_j\mathbf{d}_i^T)}$$

$$\lambda_j = \frac{(\mathbf{k}_{ij}\mathbf{d}_j^T) + (\mathbf{d}_j\mathbf{d}_i^T)\lambda_i}{(\mathbf{d}_j\mathbf{d}_j^T)} \tag{4.2}$$

Except for parallel vectors, each pair of vectors $\mathbf{n}_i$ and $\mathbf{n}_j$ has a minimum distance, therefore a threshold has to be applied to determine distances close to an intersection. Parallel vectors are detected when the denominator for λ_i is 0. The threshold has been set to 0.1 mm, because lower thresholds would be below the resolution of our 3D-scanner and therefore for our whole documentation system. Due to the resolution, we have hundreds of vectors of neighboring areas pointing in the same direction. For performance issues 10% of the normal vectors were randomly selected by using a normal distribution. This increases the processing speed by a factor of 20.

Figure 4.2 shows the points $\mathbf{v}_{ij}$ with $\rho < 0.1$ mm for the largest synthetic objects ($\beta_{cm} = 60°$) with and without normal distributed noise. Fitting a correct rotational axis (equals z-axis) using the *PCA* could only be achieved for the cylinder and the cone without noise. Furthermore we see, the influence of the quantization error for $\mathbf{v}_{ij}$ in Figure 4.2a,b,e,f. Another drawback of [Kam03] in respect to [CM02] are the parameters

required for the accumulator space. These parameters are the size, position and resolution, which can easily be set if the size and shape of an object is well- known, like in industrial applications. For sherds these parameters have to be adapted for each shape, because, for example, a convex sherd requires a smaller size with finer resolution than a cylindrical sherd of the same size. This can bee seen in Figure 4.2e, where the accumulator space has to be $10{\times}10{\times}30\ mm$ in contrast to Figure 4.2i, where the accumulator space has to be $5{\times}5{\times}10\ mm$.

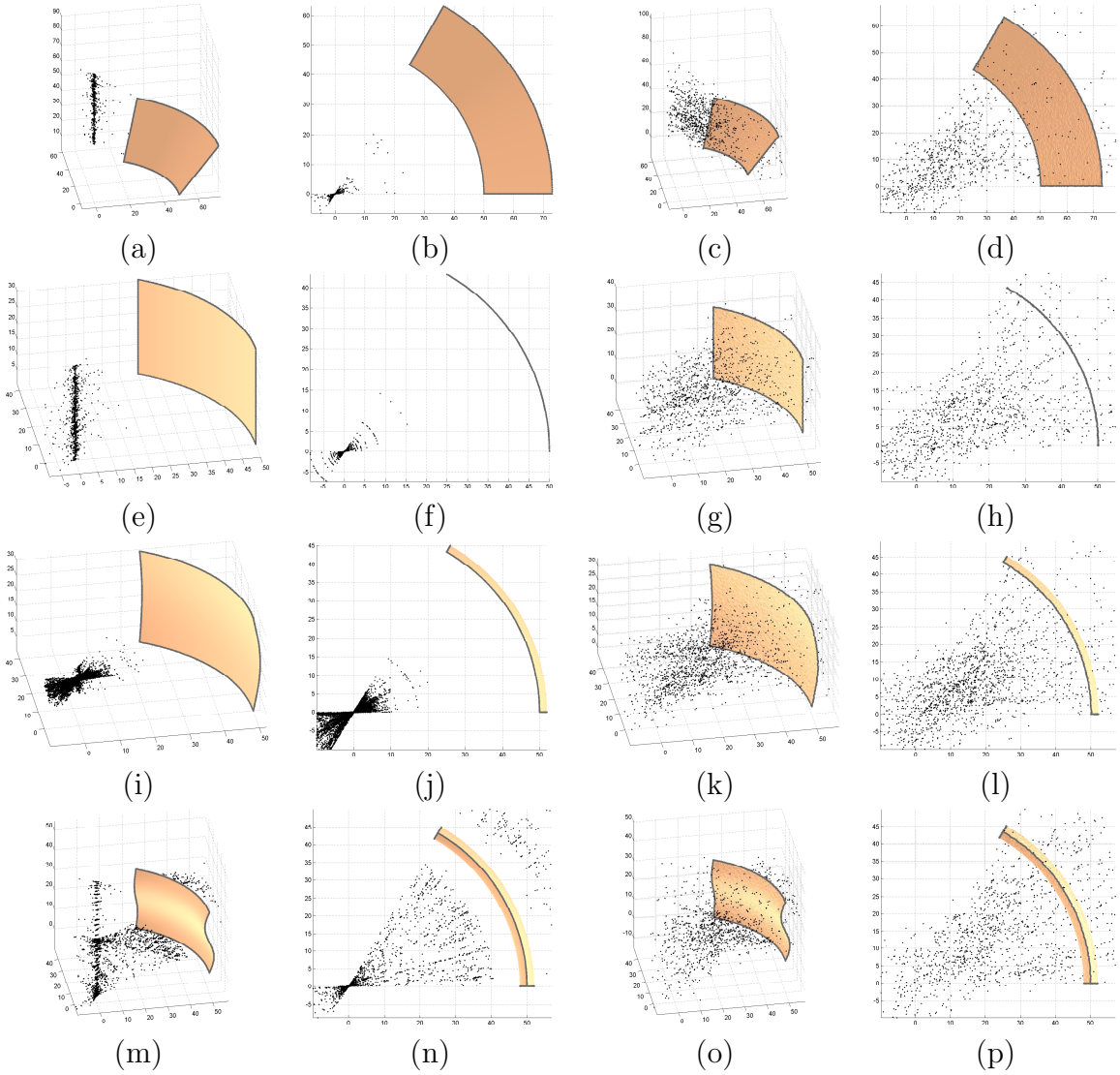

Figure 4.2: Points of "intersection" of normal vectors for synthetic fragments for a cone (a,b) without and (c,d) with noise, cylinder (e,f) without and (g,h) with noise, sphere (i,j) without and (k,l) with noise and a s-shaped vessel (m,n) without and (o,p) with noise. The distribution of the noise is uniform.

As an axis is described by a vertex $\mathbf{k}$ and a direction $\mathbf{d}$, the result of the evaluation is the distance d_{s-NV} between the rotational axis $\mathbf{s} = \mathbf{k}_s + \lambda_s \mathbf{d}_s$ of the objects and the estimated rotational axis $\mathbf{NV} = \mathbf{k}_{NV} + \lambda_e \mathbf{d}_{NV}$. The distance d_{s-NV} is shown in mm at the point at half height ($z = 15\ mm$) of the objects. The direction is compared by estimation of the angle γ_{s-NV} between the rotational axis of the objects and the estimated axis. The numeric results are shown in Table 4.1 for the objects shown in Figure 4.2. The same objects are used for experiments using the estimation of the rotational axis proposed in this thesis.

Type	β_{cm}	d_{s-NV}	γ_{s-NV}	d_{s-NV}	γ_{s-NV}
		smooth		noisy	
Cone	60°	0.90	5.46°	38.21	50.13°
Cylinder	60°	0.02	0.25°	22.39	89.70°
Sphere	60°	49.68	86.23°	17.51	88.67°
S-Shape	60°	314.70	81.30°	31.39	89.72°

Table 4.1: Distance between the rotational axis $\mathbf{s}$ of synthetic fragments and the estimated rotational axis $\mathbf{NV}$ estimated using *PCA*. The distance d_{s-NV} between the real, synthetic axis and the estimated axis at the half height of the objects is shown in mm. The angle γ_{s-NV} between the axis is shown in degree.

Based on these experiments, we can conclude that normal vectors can be used for perfectly rotational objects, like used in industry and very well manufactured ceramics. Due to the surface of coarse ware and possible distortions of symmetry due to a sloppy manufacturing process, methods on based tracing normal vectors are not applicable.

4.3 Orientation using Circle Templates

For our new approach, we choose a method inspired by a variation of the manual orientation, which is related to [MLCT03], because we also use fitting of circle templates for axis estimation. The difference between our method and [MLCT03] is the automatic axis estimation, shown in this section. Therefore we do not require any manual interaction to extract profile lines, which saves working time of archaeologists.

The variation of the manual method uses the rills on the inside of a sherd, which are horizontal traces of the manufacturing process. When an archaeologist orients such a sherd, he places the sherd vertical in front of him and rotates it about the direction of view and tilts towards him until the rills are seen as horizontal stripes.

Virtually looking at the horizontal stripes/rills from the top, the rills describe arcs of concentric circles. The second method of manually orientation is applied to sherds without rills. Therefore archaeologists use circle templates, which are manually fit into the inside of a sherd until the circle templates are concentric and their centers are aligned

along the rotational axis. The following method is derived from the manual method.

The next step is the vertical alignment of the remaining surface by translation of the center of gravity into the origin and by rotation using the Eigenvectors [Arf85, MM88] of the vertices estimated by *SVD* [Str88]. This step fits the surfaces balance plane into the xz-plane. The first approximation of the rotational axis based on this orientation is done by intersections of multiple planes:

1. Estimate the bounding box (l_x, l_y and l_z) of the sherd.
2. Estimate n multiple planes $\mathbf{p}_n$ parallel to xy-plane, with offsets $d_i = i\frac{l_z}{n}$, $i = \{1, .., n\}$ parallel to the z-axis. n has been chosen, so that $d_{i+1} - d_i$ is twice the resolution of the 3D-model.
3. Estimate the intersection $\mathbf{v}_{pt}$ between $\mathbf{p}_n$ and the edges of the triangles $\mathbf{t}$. For this algorithm the estimation of $\mathbf{v}_{pt}$ is sufficient. As we require connected vertices for the profile line, we use for this algorithm the same method as show in Section 5.2.
4. For each plane $\mathbf{p}_n$ the 3D-coordinates of $\mathbf{v}_{pt_n}$ are transformed into the 2D-coordinate system $\mathbf{v}'_{pt_n}$ of p_n.
5. A 2D-circle is fitted into $\mathbf{v}'_{pt_n}$ using minimizing the least square error [GGS94]. The 2D-circle is described by its center $\mathbf{x}'_{0_n}$, the radius r and the average distance σ_n of the vertices $\mathbf{v}'_{pt_n}$ to the circle.
6. Estimate the standard variation of the centers $\mathbf{x}'_0$ parallel to the x-axis.
7. Rotate the surface about $\alpha = 5°$ about the y-axis and return to step 1 until the surface has been rotated about 355°.
8. Select $\mathbf{x}_{0_k}$ with the lowest deviation parallel to the x-axis as first approximation of the rotational axis, by least-square fitting of a line.

For increased performance this algorithm has been modified by rotation of the intersecting planes instead of rotating all vertices of the surface. Furthermore the elongation along the z-axis of the bounding box is estimated by the maximum radius in the direction of the normal vectors of the intersecting planes using the radii of the vertices in the polar coordinate system. Figure 4.3 shows all intersections $\mathbf{v}_{pt_n}$ in different level of gray. The level of gray corresponds to n.

In case of a sherd from a cylindrical vessel, similar to Figure 4.1a, this approximation would return the rotational axis. As ceramics are generally not cylindrical the circles are fitted into elliptic shaped intersections $\mathbf{v}_{pt}$ and therefore the centers $\mathbf{x}_{0_n}$ are located on the major axis of the ellipse, but the centers have to be shifted towards/backwards the rotational axis. This means that the first approximation using $\mathbf{x}_{0_k}$ is an axis that is located on a plane of symmetry together with the rotational axis (also called axis of symmetry).

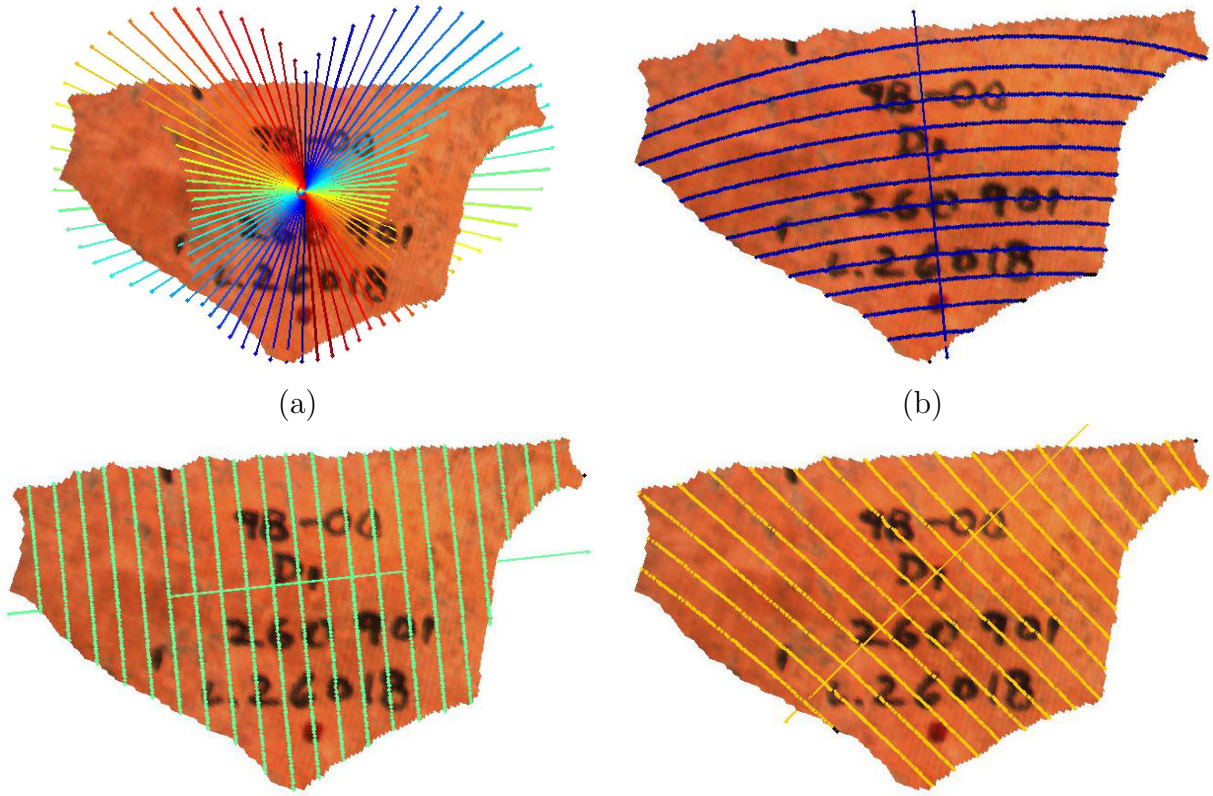

Figure 4.3: (a) Axes used for the first estimation of the rotational axis. These axes are defined by the masspoint and the balancing plane. (b) First Axis from (a) defined by the first eigen-vector of the balancing plane. (c) Axis defined by the second eigen-vector of the balancing plane. (d) Axis from (a) defined by the about 130° rotated first eigen-vector of the balancing plane.

The estimation of the final axis of rotation is based on the same algorithm described above, but instead of rotation the plane $\mathbf{p}_n$ about the y- axis the planes are rotated within the plane of symmetry about the center of gravity of $\mathbf{x}_{0_k}$ (second iteration). As sherds are not perfectly symmetric, practical experiments have shown that the axis of symmetry can be tilted for a maximum of 10°. Therefore a third iteration of the algorithm with a tilted plane of symmetry can improve the result.

4.4 Minimum Fragment Size

In theory having 3 points (A, B and C) of a circle are sufficent to determine its center. Only if these points are aligned along a line, the radius is infinite and therefore no center can be estimated. For our real world application we expect these points to be error prone. This means that these points can be shifted (A', B' and C') by e_z and therefore aligned on a line. As we acquire the inner side of the fragment parallel to the image plane of the 3D-scanner, the error for depth (e_z) influences the points describing the circles estimated by intersection of the inner side. Figure 4.4 shows the influence of e_z on A, B and C of a circle-arc.

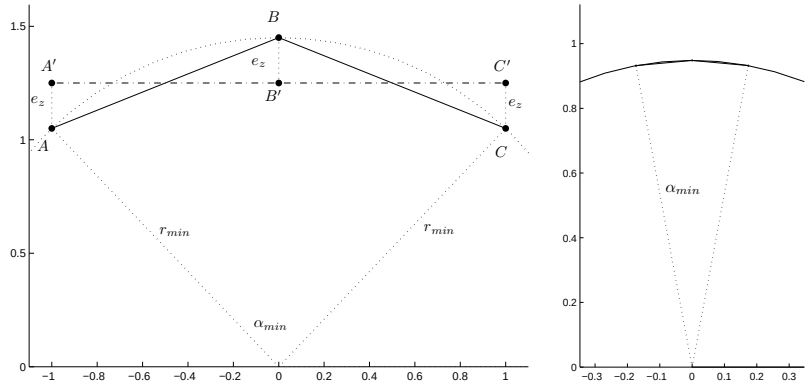

(a) (b)

Figure 4.4: (a) Scheme of a circle described by three points A, B and C, which are shifted by $e_z = 0.2$ to A', B' and C'. $d_{xy} = 1$. (b) $\alpha_{min} = 21.08°$ using $d_{xy} = 0.72\ mm$ and $e_z = 0.008\ mm$ of our 3D-scanner.

Having the error e_z and the x, y-resolution of d_{xy} of a 3D-scanner, we can estimate the minimum angle α_{min} of the circle arc using the following equations:

$$a = b = |\overline{AB}| = \sqrt{d_{xy}^2 + 4e_z^2}\ ,\ c = |\overline{CA}| = 2d_{xy} \quad \ldots \quad \text{Length of the triangles edges.}$$

$$S = |\overline{AB} \times \overline{BC}|/2 = 2d_{xy}e_z \quad \ldots \quad \text{Area of the triangle.}$$

$$r_{min} = \frac{abc}{4S} = \frac{d_{xy}^2+4e_z^2}{4e_z} \quad \ldots \quad \text{Radius of the circle.}$$

$$\alpha_{min} = 2 * arcsin\frac{d_{xy}}{r_{min}} \tag{4.3}$$

Using the given precision $e_z = 0.008\ mm$ and the x, y-resolution between $d_{xy} = 111/640\ mm = 0.17\ mm$ and $d_{xy} = 463/640\ mm = 0.72\ mm$ (see Table 3.1) of our 3D-scanner we get a minimum angle between $\alpha_{min} = 5.07°$ and $\alpha_{min} = 21.08°$ using the "Tele"-lens. As the precision decreases with the focal length, the range of α_{min} is identical for the other lenses. As ceramics are not perfectly symmetric, α_{min} depends on the technique used for manufacturing. Practical experiments have shown, that sherds have to cover at least 7% ($\alpha_{min} \approx 25°$) of the circumference for proper orientation.

The minimum height of a fragment has to be twice d_{xy} [Sha48], because in theory we need only two circlces to estimate an axis. Practical experiments using our 3D-scanner have shown, that the height should be at least 10 mm.

Another limit, which has to be considerd, are fragments of spheres because spheres have a point of rotation instead of an axis of rotation. Therefore fragments having profile lines shaped like a circle arc can not be orientated when the radius r_{ca} of the circle arc equals the radius r_o of the object. Practical experiments with synthetic objects have shown that the rotational axis can be estimated, when $|r_{ca} - r_o|/r_o > 0.15$.

Concluding this section, we can propose the proper orientation of sherds with a minimum height of 10 mm covering more than 7% of the circumference.

4.5 Experiments with Synthetic Data

The synthetic data, which are fragments of synthetic rotational objects, have been estimated by rotation of a line, a tilted line, a circle arc and a sinus wave. Therefore we use fragments of a cylinder, cone, sphere and a s-shaped object. We begin with experiments regarding the removal of noise, estimation of geodesic distance, geodesic patches, curvature and finally the estimation of the rotational axis.

For evaluation of the orientation and therefore for evaluation of the estimation of the rotational axis we choose a set of 24 synthetic fragments of rotational objects with well known axis of rotation. About this axis we rotated vertical lines, diagonal lines, circle arcs and a sinus waves. These lines have been chosen in respect shapes of real profile lines and extreme cases, which are fragments of spheres and cones. Spheres do not have an axis of rotation; they have only a point of rotation (center). Fragments of spheres are typically from bowls. Cones with a large angle can introduce numeric problems, because of low curvature and sliding intersection. They are typical for plates. Furthermore we choose a simple cylinder (jugs) and an S-Shaped fragment (bowls).

All fragments have a height of 30 mm and a minimum diameter of 50 mm. The maximum diameters are 70 mm for the fragments of the sphere and the s-shaped object and 80 mm for the cone. Along the circumference the fragments cover an angle β_{cm} of 20° (5.6%), 40° (11.2%) and 60° (16.8%) of the complete object. The mesh describing the surface has been estimated using quadrangular patches with an edge length of 0.65 mm, which are divided into triangles, to simulate the data-structure of our real sherds. Therefore we get synthetic fragments with an area between 500 and 2500 mm^2, which correspond to a number of triangles between 4000 and 13000. These sizes are determined by the memory usage. Practical experiments have shown that larger sizes dramatically slow down the axis estimation, because the memory (1 GB[1]) of our computer was exceeded.

[1] $GB \ldots$ *Gigabyte*$\ldots$ 1.073.741.824 *Bytes*

As these 12 synthetic fragments are almost smooth, only introducing a minor quantization error, we estimated a second set of fragments with normal distributed noise to simulate the noise introduced by the 3D-scanner. The fragments with noise are duplicates from the fragments without noise. The level of noise has been set to twice the noise of the 3D-scanner, which can estimate the position of a vertex with an absolute accuracy of 0.1 mm. This corresponds to a relative accuracy of 10% for objects of the size of our synthetic fragments.

Table 4.2 shows, similar to Table 4.1, the distance d_{s-C3D} in mm between the rotational axis **s** of the objects and the angle γ_{s-C3D} between the estimated axis **C3D** at the half height ($z = 15\ mm$) of the objects. Furthermore the objects with $\beta_{cm} = 60°$ are identical to the objects shown in Figure 4.2 and Table 4.1.

Figures 4.5 shows the results for the fragments of the cylinder. The first column shows the fragment and the axis used for the first estimation like Figure 4.3a. The second column shows the deviation of the centers for selection of the first iteration of the axis estimation - lower values mean better fit. The levels of gray of the bars correspond to the color of the axis of the first column. The third column shows the rating for the second iteration. The forth column shows the estimated rotational axis (line with dots) after third iteration and the synthetic axis (dashed line).

Type	β_{cm}	d_{se}	γ_{s-C3d}	d_{se}	γ_{s-C3d}
		smooth		noisy	
Cylinder	20°	0.00	0.00°	0.27	1.78°
	40°	0.00	0.00°	0.04	0.05°
	60°	0.00	0.00°	0.02	0.09°
S-Shape	20°	0.00	0.00°	0.61	1.79°
	40°	0.00	0.00°	0.16	0.51°
	60°	0.00	0.00°	0.01	0.04°
Sphere	20°	0.00	0.00°	0.04	0.38°
	40°	0.00	0.00°	0.12	1.71°
	60°	0.00	0.00°	0.05	0.19°
Cone	20°	0.06	0.04°	2.22	2.70°
	40°	0.15	0.11°	1.41	0.51°
	60°	0.74	0.55°	0.37	0.37°

Table 4.2: Distance between the real rotational axis ($\mathbf{k}_s + \lambda_s \mathbf{d}_s$) of synthetic fragments and the rotational axis ($\mathbf{k}_{C3d} + \lambda_{C3d} \mathbf{d}_{C3d}$) estimated by our algorithm. d_{s-C3d} is shown in mm and γ_{s-C3d} is shown in degree. The height of the fragment is 30 mm and the diameter, depending on the type is between 50 and 70 mm.

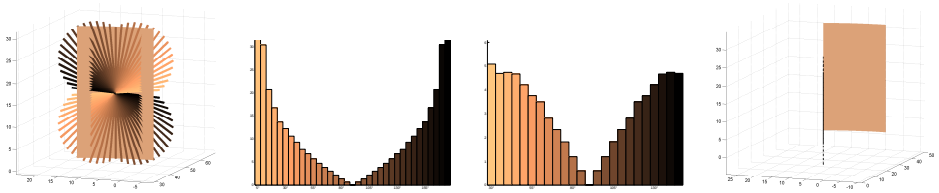

Cylinder, $\beta_{cm} = 20°$, smooth.

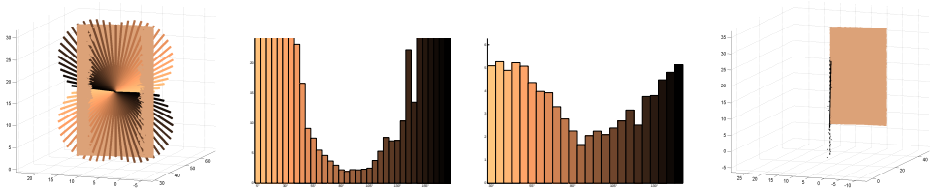

Cylinder, $\beta_{cm} = 20°$, noisy.

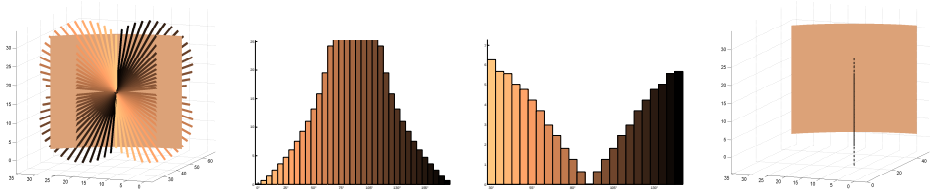

Cylinder, $\beta_{cm} = 40°$, smooth.

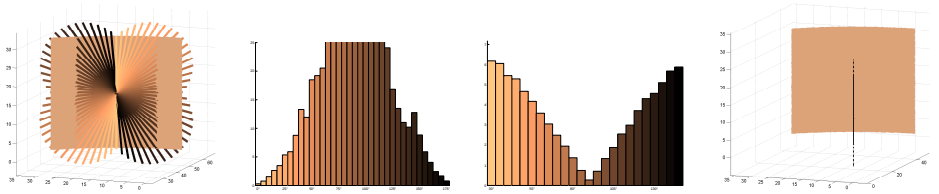

Cylinder, $\beta_{cm} = 40°$, noisy.

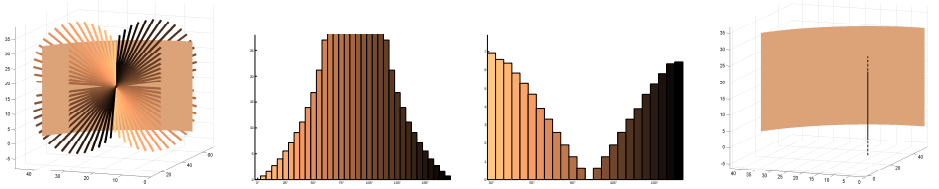

Cylinder, $\beta_{cm} = 60°$, smooth.

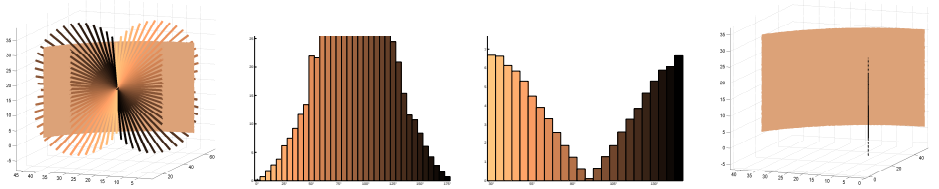

Cylinder, $\beta_{cm} = 60°$, noisy.

Figure 4.5: Results of the orientation of a synthetic fragment of a cylinder.

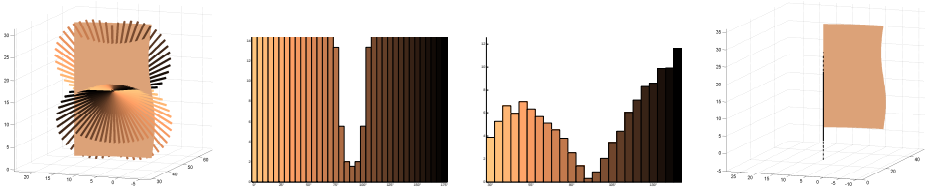

S-Shape, $\beta_{cm} = 20°$, smooth.

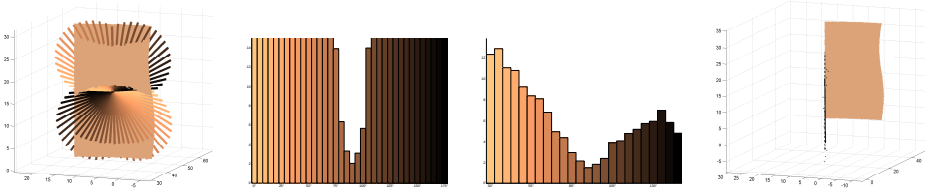

S-Shape, $\beta_{cm} = 20°$, noisy.

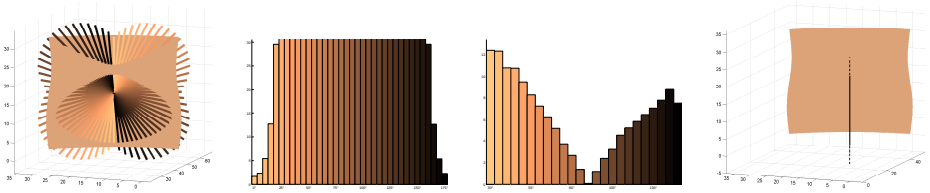

S-Shape, $\beta_{cm} = 40°$, smooth.

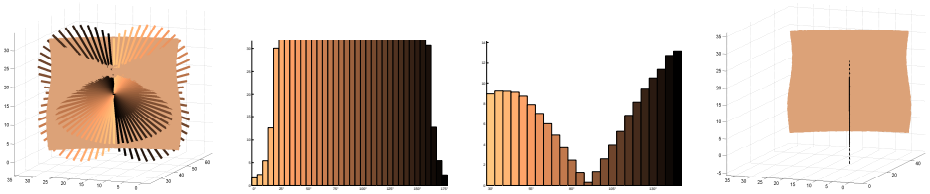

S-Shape, $\beta_{cm} = 40°$, noisy.

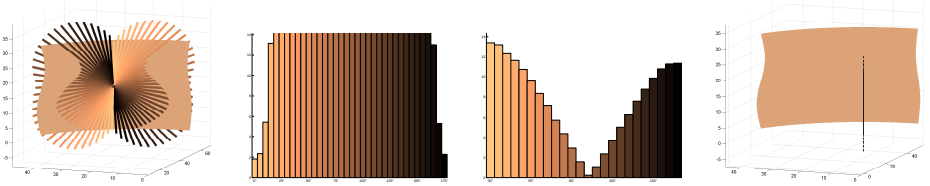

S-Shape, $\beta_{cm} = 60°$, smooth.

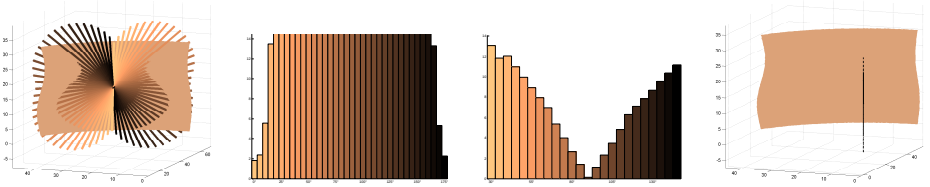

S-Shape, $\beta_{cm} = 60°$, noisy.

Figure 4.6: Results of the orientation of a synthetic fragment of an s-shaped object.

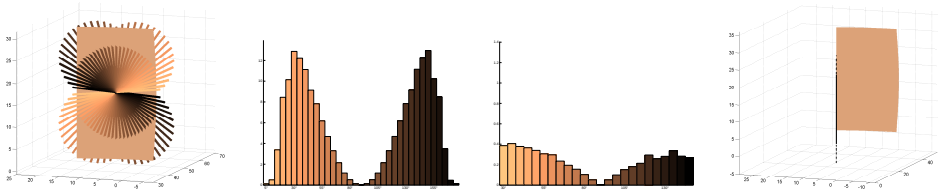

Sphere, $\beta_{cm} = 20°$, smooth.

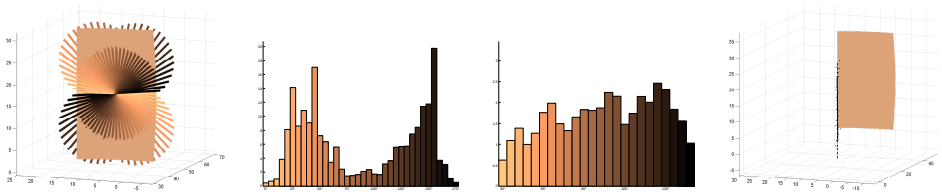

Sphere, $\beta_{cm} = 20°$, noisy.

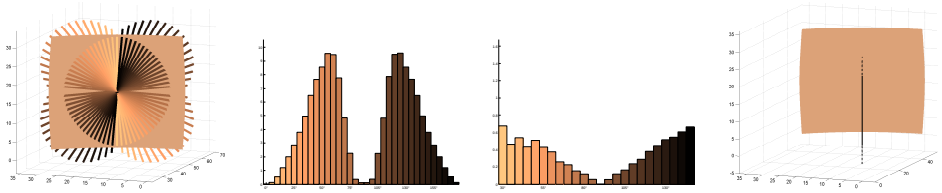

Sphere, $\beta_{cm} = 40°$, smooth.

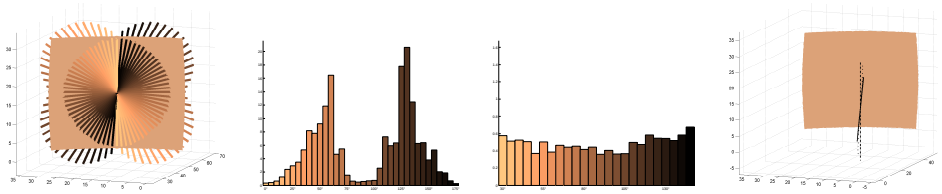

Sphere, $\beta_{cm} = 40°$, noisy.

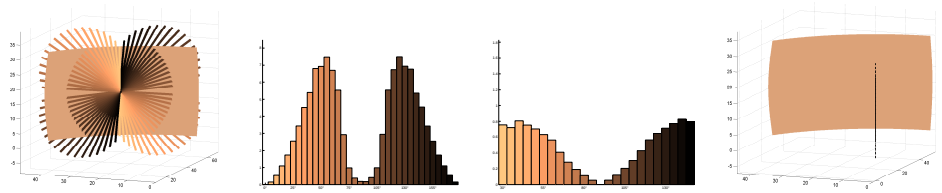

Sphere, $\beta_{cm} = 60°$, smooth.

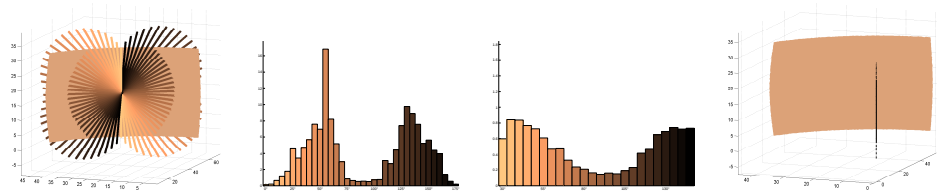

Sphere, $\beta_{cm} = 60°$, noisy.

Figure 4.7: Results of the orientation of a synthetic fragment of a sphere.

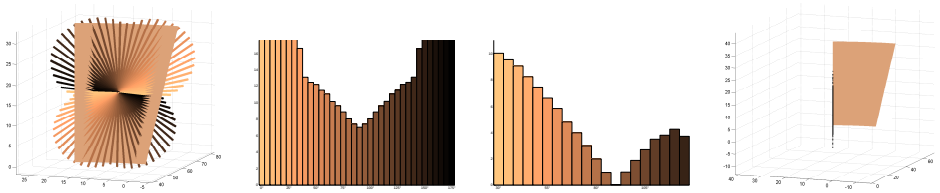

Cone, $\beta_{cm} = 20°$, smooth.

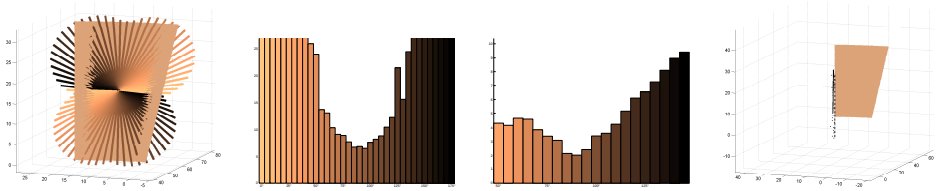

Cone, $\beta_{cm} = 20°$, noisy.

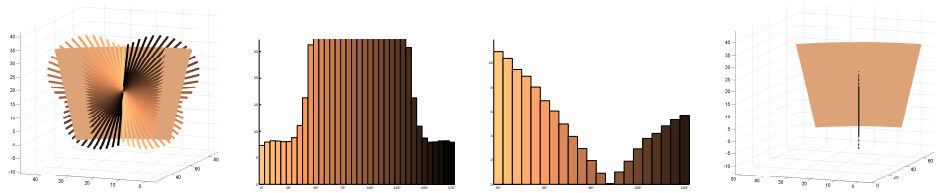

Cone, $\beta_{cm} = 40°$, smooth.

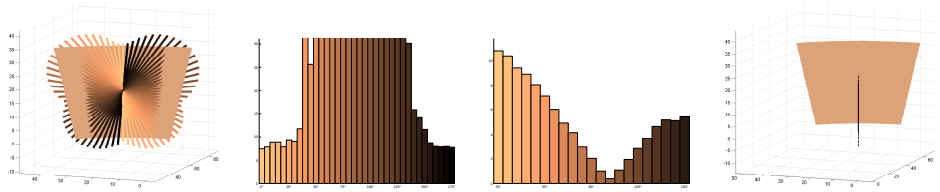

Cone, $\beta_{cm} = 40°$, noisy.

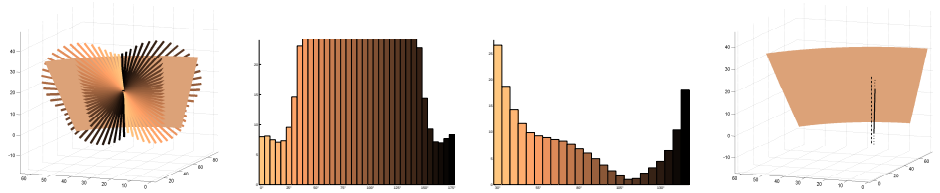

Cone, $\beta_{cm} = 60°$, smooth.

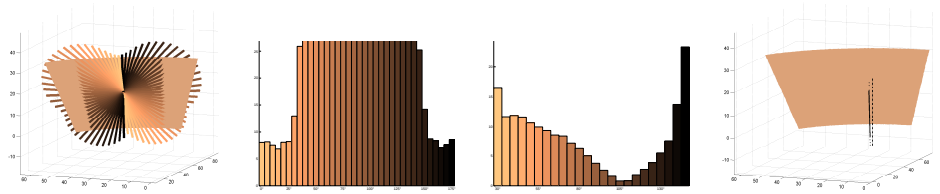

Cone, $\beta_{cm} = 60°$, noisy.

Figure 4.8: Results of the orientation of a synthetic fragment of a cone.

Regarding the results shown in Table 4.2, we can conclude that the estimation of the rotational axis is most difficult for fragments of cones. The reason therefore being the influence of distortion by noise and quantization of the angle θ between the intersecting planes and the surface of the fragment. For our experiments with the cone without noise, the angle θ has a maximum of $\theta_{max} = 40°$, when the intersecting planes are perfectly orthogonal to the rotational axis. In our experiments with the cone including noise, the noise shifts the vertices up to 20% randomly in any direction. Therefore this shift is also parallel to the intersecting planes towards the rotational axis, which changes the angle θ for $\pm 11°$. This corresponds to a maximum error of 25% for θ_{max}, which increases for lower values of θ. Despite this massive influence of noise for cones, we could achieve an axis having less than 4.5% error regarding the radial error and less than 3.0% for the angular error.

Figure 4.9 shows the scheme (side-view) of intersecting planes (dotted) orthogonal to the rotational axis of the undistorted cone (continuous) for $\theta = theta_{max} = 40°$. The distorted cone $\theta = (29°,\ 51°$ is shown as dashed lines. This scheme shows the maximum influence of noise for the best case of intersections required for estimation of the rotational axis.

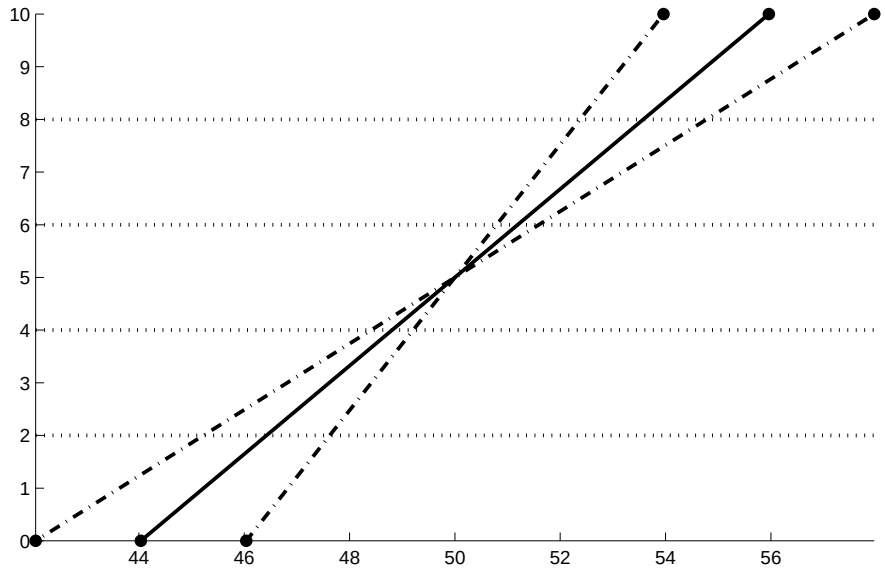

Figure 4.9: Scheme (side-view) of angles of intersection θ of the cone (continous line) intersected by planes (dotted) orthogonal the rotational axis. The dashed line shows the surface tilted by noise.

The angular error of θ is in general responsible for increasing error for lower values of β_{cm}. The only exception are the results from the fragments, which are shaped like a sphere, because for a perfect sphere the rotational axis degenerates to a point of rotation and therefore the quadratic ($h : 2r\pi/\beta_{cm} \approx 1$) fragment ($\beta_{cm} = 40°$) has the maximum error for our experiments with fragments of spheres with noise.

Summarizing the results shown in Table 4.2, we can estimate the rotational axis for all fragments. All results using fragments without noise, except the cone, have no measurable error (angular and radial) regarding the resolution of our system (0.01 mm, 0.01°). Even the cone, has an acceptable error of less than 1% for the worst case. Using the fragments with noise the error for estimation of the rotational axis is below 1% for the cylinder and the s-shaped fragments. The fragments shaped like a sphere have an error less than 2% and the fragments of the cone have an error less than 4.5°. Even the error for the cone is acceptable, because the noise added is twice the noise of our 3D-scanner and the precision for manual drawings, given by archaeologists, is $\approx 5\%$.

Table 4.3 shows the results for orientation using normal vectors (NV) from Table 4.1 in comparison with the results using fitting of circle templates ($C3D$) from Table 4.2. Regarding Table 4.3 we can conclude an increase of accuracy using circle templates by a factor of more than 10 depending on the shape of an object. Only for the smooth cylinder the results are approximately identical.

Type	β_{cm}	d_{s-NV}	γ_{s-NV}	d_{s-NV}	γ_{s-NV}	d_{se}	γ_{s-C3D}	d_{se}	γ_{s-C3D}
		smooth		noisy		smooth		noisy	
Cone	60°	0.90	5.46°	38.21	50.13°	0.74	0.55°	0.37	0.37°
Cylinder	60°	0.02	0.25°	22.39	89.70°	0.00	0.00°	0.02	0.09°
Sphere	60°	49.68	86.23°	17.51	88.67°	0.00	0.00°	0.05	0.19°
S-Shape	60°	314.70	81.30°	31.39	89.72°	0.00	0.00°	0.01	0.04°

Table 4.3: Distance between the rotational axis **s** of synthetic fragments and the estimated rotational axis **NV** estimated using PCA. The distance d_{s-NV} between the real, synthetic axis and the estimated axis at the half height of the objects is shown in mm. The angle γ_{s-NV} between the axis is shown in degree.

Finally we estimated the time for processing of the synthetic fragments. The time consumed by fitting of circle templates was 15 to 45 seconds, depending on their size. As we choose the size and type of our synthetic objects similar to the smallest and flattest pieces which can be orientated by humans, we can propose at least the same results for the automated orientation of the sherds in a fraction of time. The next section shows a comparison of the proposed method and the manual method, which inspired our work.

4.6 Comparison with the Manual Aproach

As our method is inspired by the method for manual orientation, we compared our method with the manual method using a well-known real vessel. The vessel was industrially manufactured with a given radius of 65 mm for the orifice. This vessel has been broken into 5 sherds, shown in Figure 4.10. These sherds are two fragments covering approximately half of the vessel. These two fragments have a matching surface and therefore they are numbered as "1a" and "1b" and were drawn as reconstructed fragment by archaeologist. The manual drawings are shown in Figure 4.11.

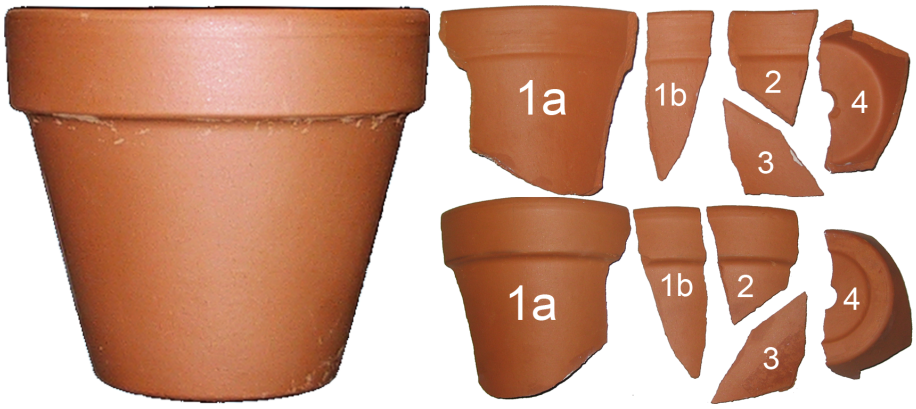

Figure 4.10: Well-known modern pot (left) and the front-view and back-view of its sherds (right, with numbers) for comparison of the automated and manual estimation of the rotational axis.

The sherd numbered "2" is a typical rim-fragment. The wall-fragment was numbered "3" and was not drawn manually, because it is difficult to orientate manually and without a matching fracture to another sherd and without decoration it can not be used for archaeological classification. As we propose our new orientation method independed of rim-fragments in contrast to [MLCT03], we included it in our experiment. The bottom sherd was numbered "4".

To compare the methods we choose three features of profile lines, which can be derived from the manual drawings. The first two features were the maximum diameter and the preserved height, which was given as numbers by archaeologists and derived from the digitized manual drawing. As third feature we choose the angle of the straight wall towards the rotational axis, because it is related to the archaeological "orientation" of the profile line. Therefore the longest outer part profile with minimal deviation to a straight line was chosen. The deviation of points describing the straight line was 0.05 mm for the profile line of the 3D-model and 0.15 mm for the manual drawing. The reason for selecting the outer part, was that archaeologists consider the outer part of the profile as more important than the inner part, because in general only the outer part contains the characteristic points for classification.

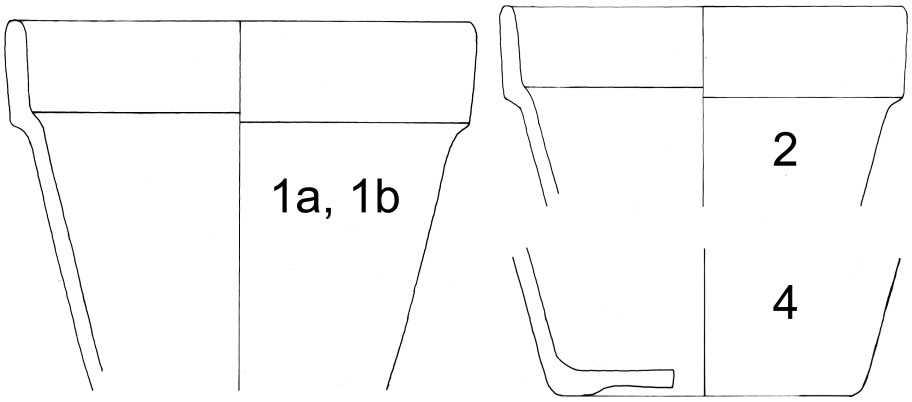

Figure 4.11: Manual drawings of sherds of a well-known modern pot. Large, matching sherds (No. 1a, 1b) covering approximately 2/3 of the pot, small sherd (No. 2) and bottom sherd (No. 4).

Figure 4.12 shows the horizontal intersections for the final step of the estimation of the rotational axis. These intersections are arcs of concentric circles with a deviation less than 0.5 *mm* of their centers. Figure 4.12(a) contains the arcs of sherds "1a' and "1b" registered by use of the circle centers. An extra space between "1a" and "1b" has been added for better visibility of the intersections of "1a" and "1b".

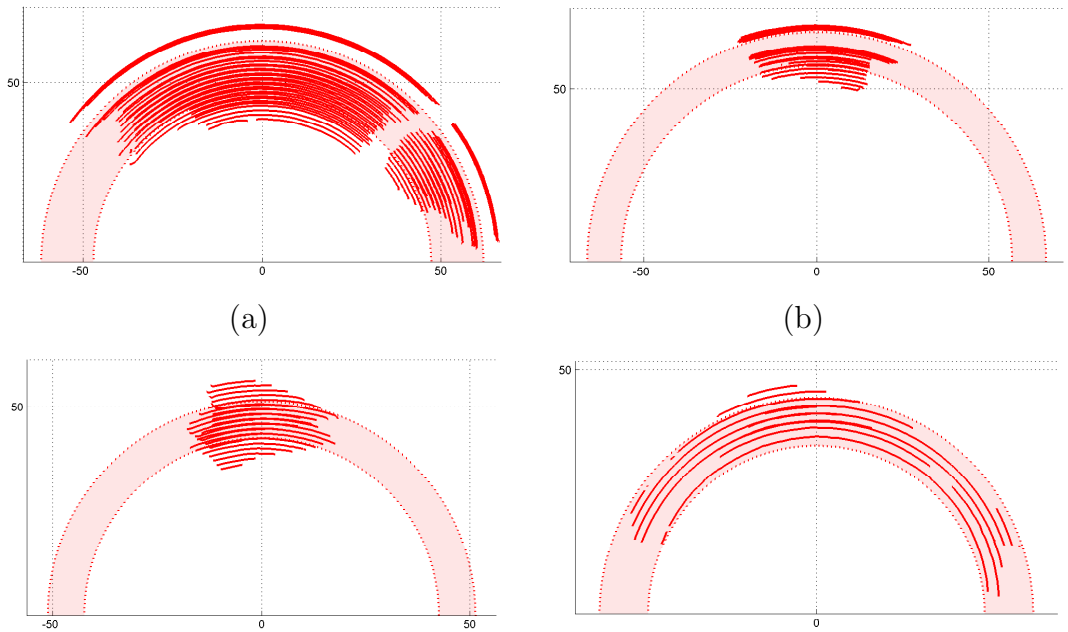

Figure 4.12: Horizontal intersection for final estimation of the rotaional axis. Sherds number (a) "1a" registered with "1b" (b) "2" (c) "3" and (d) "4".

Figure 4.13a,b,d,f,g show the profile lines extracted from the 3D-model using the estimated rotational axis. The method for extraction is a horizontal intersection of the 3D-model using a plane defined by the rotational axis and the point of maximum height of the sherd. This method, which uses multiple profile lines is shown in detail in the following chapter. For each sherd the multiple profile lines have been estimated along the circumference. This was done to estimate the deviation of the distance between pairs of multiple profile lines to approximate the accumulated error of acquisition system and axis estimation. For the sherds "1" to '3' the deviation of the distance between pairs of multiple profile lines was less than 0.7 mm. The sherd "4" for the bottom had a maximum deviation of 1.1 mm. The reason therefore is that only 870 mm^2 of the sherds surface could be used for axis estimation due to flat parts of the bottom. This renders sherd "4" as smallest sherd in respect to the axis estimation. The complete surface area of sherd "3" and of the other sherds is shown Table 4.4. Figure 4.13c,e,h show their manually drawn counterparts.

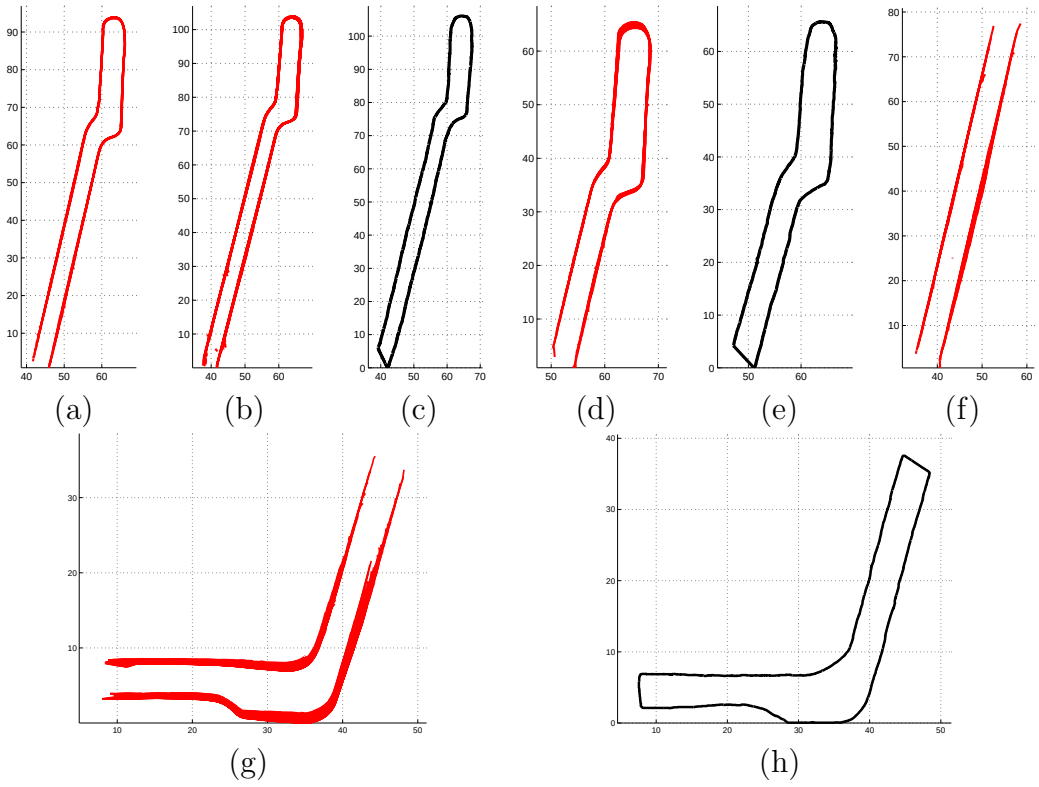

Figure 4.13: Profile lines estimated using the 3D-model of sherds number (a) "1b", (b) "1a", (d) "2" (f) "3" and (g) "4". Profile lines manuall drawn of sherd number (c) "1a" and "1b", (d) "2" and (h) "4".

Table 4.4 shows the size of the sherds as area of the surface in mm^2 and the three features maximum radius r, preserved height h and angle of straight wall γ for the profile line using the orientation by fitting of circle templates ($C3D$) and from the manual drawing (M). Furthermore the same features are shown using the method based on normal-vectors

(NV). For r_M and h_M the first value is the number given by archaeologists, measured with a caliper. The second value has been estimated using the digitized manual drawing. Therefore it appears that there is a minor scaling error of 3.8%, which may be introduced by rounding or the device for digitizing the drawing. For sherds "1a" and "1b" we can show that we have repeat accuracy auf 0.2 mm (0.3%) in respect to radius of 65 mm. Regarding the radii we have a maximum difference $r_{C3D} - r_M = 2.2; mm$ (3.3%) for sherd "2". The comparison of the results of the manual drawings and the circle fitting with the method based on normal vectors shows a larger error, which is between 7.7% and 28.5% for the radii and between 4.3% and 37.7% for the angular error.

Sherd No.	Area mm^2	r_{C3D} mm	h_{C3D} mm	γ_{C3D}	r_M mm	h_M mm	γ_M	r_{NV} mm	h_{NV} mm	γ_{NV}
1a	9553	66.9	103.9	76.2°	65 / 67.5	104 / 106.1	76°	56.3	102.6	69.3°
1b	2773	66.7	93.9	77.2°	65 / 67.5	104 / 106.1	76°	49.2	93.8	71.1°
2	2595	68.9	65.4	76.4°	65 / 66.7	65 / 65.6	75°	34.3	59.8	60.1°
3	1960	58.7	78.5	77.1°	n.a.			39.6	75.8	66.3°
4	3887	48.3	36.9	73.3°	37 / 37.5	50 / 48.4	75°	20.5	25.6	41.1°

Table 4.4: Radii (r), height (h) and tilt-angle (γ) of the profile lines of the well-known vessel estimated by manual drawing (M), by estimation of the rotational axis using circle templates ($C3D$) and by using normal vectors (NV).

Concluding Table 4.4 we could show that the results using the proposed method differ for no more less than 4% from manual drawings of a well-known vessel. Measurements regarding performance showed that the manual drawings were done in 7 to 9 minutes. The profile lines were acquired and estimated in 2 to 4 minutes.

The increase of accuracy of using circle fitting ($C3D$) for orientation in respect to the use of normal vectors (NV) is shown in Table 4.5. Like in Table 4.1 we estimate the distance d_{C3D-NV} between the axis at the half height of the fragments and the angle γ_{C3D-NV} between the axis.

Figure 4.14 and Figure 4.15 show the fragments orientated by use of circle fitting. Therefore the rotational axis equals the z-axis (dotted line). The "points" of intersection of the normal vectors are shown as dots and the axis fitted into the "points" is shown as dashed line.

The conclusion of Table 4.4 is, that using normal vectors is only suitable for large fragments (Sherd No. "1a" and "1b"). Smaller fragments and also the conic shape of the well-known vessel introduces a difference between 13% and 37% for the radius and a difference between 8% and 42% for angular comparison. As the error estimeted for orientation by fitting of circle templates is less than 4%, the error for using normal vectors can be given as $\approx 5\%$ for large objects up to $\approx 35\%$ for small objects ("2,4").

Sherd No.	d_{C3D-NV}	γ_{C3D-NV}
1a	8.50 mm	7.58°
1b	15.03 mm	5.00°
2	24.26 mm	18.01°
3	8.55 mm	12.63°
4	21.33 mm	38.50°

Table 4.5: Distance between the rotational axis **C3D** estimated using the proposed method and the rotational axis **C3D** estimated by the use of normal vetcors. The distance d_{C3D-NV}, estimated between **C3D** and **NV** at the half height of the sherds, is shown in mm. The angle γ_{C3D-NV} between the axis is shown in degree.

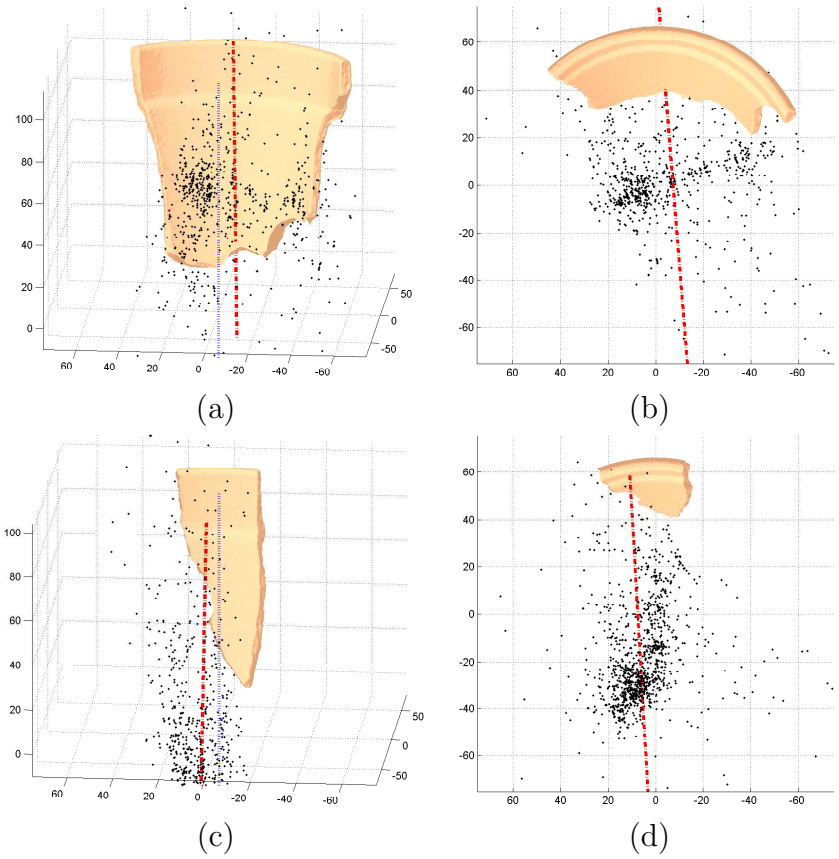

Figure 4.14: "Points" of intersection using the normal vectors for sherd (a,b) 1a and (c,d) 1b. The estimated axis using *PCA* is shown as dashed line. The axis estimated by fitting circle templates is shown as dotted line (equals z-axis). The first column (a,c) shows the inner sides of the fragments and the second column (b,d) shows a views from the top.

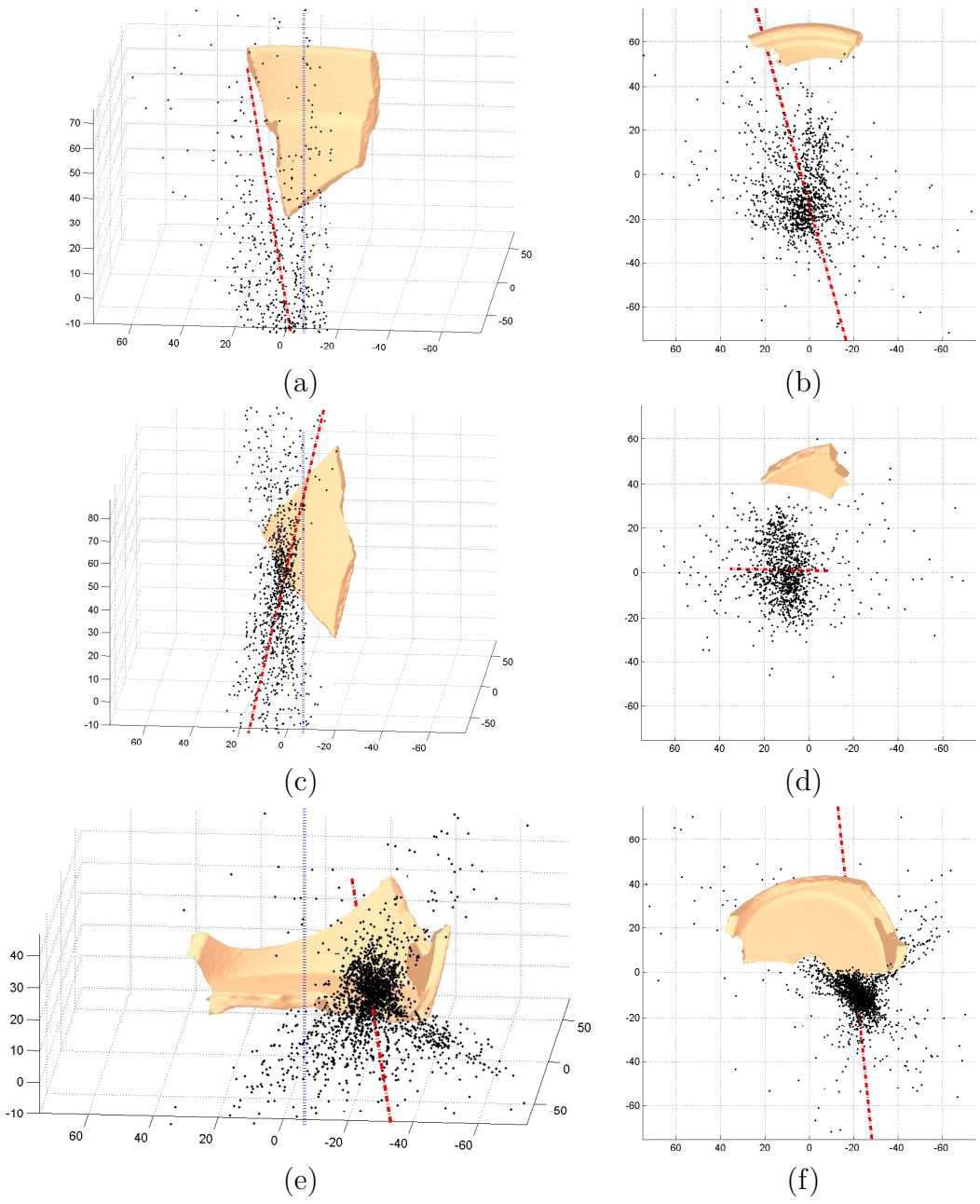

Figure 4.15: "Points" of intersection using the normal vectors for sherd (a,b) 2, (c,d) 3 and (e,f) 4. The estimated axis using *PCA* is shown as dashed line. The axis estimated by fitting circle templates is shown as dotted line (equals z-axis). The first column (a,c,e) shows the inner sides of the fragments and the second column (b,d,f) shows a views from the top.

4.7 Summary

Concluding this chapter, we have described and compared related and previous work for orientation, which is done by estimation of the rotational axis. This lead to a method inspired by the manual orientation used by archaeologists. We showed the accuracy in experiments with synthetic data. In respect to real-world application we also used synthetic objects with twice the noise as expected from our 3D-scanner. These experiments and the comparison using a real well-known objects and its manual drawing showed that we meet the requirements for archaeological documentation.

Furthermore 25 sherds have been compared with manual drawings and with the *Profilograph*. This comparison is shown in Chapter 6. The next chapter shows the processing of 3D-models, which has to be applied before the automated estimation of the rotational axis. Furthermore the next chapter shows the extraction of the profile line.

Chapter 5

Processing of Sherds

The previous chapter has shown the orientation of synthetic 3D-models and sherds acquired in the laboratory. As sherds are found at archaeological excavations, where they have to be documented straight away before they are put to their storage, we need to acquire the sherds as fast as possible. Therefore we have to take care about mounting devices of sherds and additional noise from dust. Real sherds can also have small applications (decorations), which have to be removed before the axis of rotation can be estimated. This chapter shows the required processing steps of from acquired 3D-models to proper 3D-models of sherds for orientation and documentation. Documentation means extraction of the profile line, which is shown towards the end of this chapter. Afterwards experiments with synthetic data are shown. At the end of this chapter a summary of the processing steps is given.

5.1 Noise removal

Our 3D-models contain two kinds of noise. The first kind of noise are non-existing vertices or vertices with wrong coordinates. Such noise is introduced by acquisition of dust in the air or sliding intersections of the laser-plane with parts of the acquired objects. Sliding intersections often appear at the fracture of a sherd. This kind of noise is already removed by the acquisition software of the 3D-scanner using topological noise removal [GW01].

The second kind of noise are acquired objects other than sherds. These objects are typically holding devices, which in our case is either white plasticine, or the black frame with black clamps (see Section 3.2). Even though the frame used for acquisition is colored in mate black some parts of the frame, the rotational plate and the ground plane are acquired. The reason is dust, which was always present during our work with ceramics, because even perfectly cleaned sherds are brittle and dust is falling off the breakage. Therefore the 3D-scanner always acquires parts of the background.

As the scanner also acquires color information we choose to remove (dark) black parts of the 3D-model, which have a size less than the minimum size (300 mm^2) of the acquired sherds. Sherds of this size are useless for archaeological documentation unless they are special finds (see Section 2.2.1). The minimum size may vary depending on the type of ceramics that is documented, because from large transport vessels of sizes about 1 mm of height even larger pieces are not documented.

We also used the color information for removal of plasticine, which is also used to mount sherds for 3D-acquisition and for manual drawings. In contrast to the color of the ceramics, the plasticine is colored (bright) white. Therefore we also remove parts of the 3D-model colored white. Due to illumination the threshold for the black and white color can be adjusted.

Figure 5.1 shows the frontview and the backview of the sherds after removal of noise. The result are multiple sherds stored in one 3D-model, which have to be separated for further processing. This is done by labeling of the surfaces analog to labeling of images [HS92]. Therefore the first unlabeled vertex is tagged with a new label number. Then all vertices connected with this vertex via triangles are tagged with the same label number. This is repeated until all vertices have been tagged. As we require the triangles for further processing, the triangles are tagged with the same label numbers as their vertices. Figure 5.1 shows the label numbers of the triangles as texture in levels of gray. Each level of gray corresponds to one label number. The increasing memory consumption using a recursive method can be approximated by $\sum_{n=1}^{j}(3n)^2$, where j is the number of recursive steps required for labeling. As the smallest sherds with reasonable size for acquisition have at least 100 mm^2 and the resolution is 0.1 mm, these sherds consist of 10.000 or more triangles. The largest acquired ceramics with a height of 1 m consist of $\approx$ 1 million triangles. As such 3D-models already require up to 100 MB[1] of memory and the memory consumption of recursive function increases with a power of two, we choose an iterative method, which has requires a constant amount of memory:

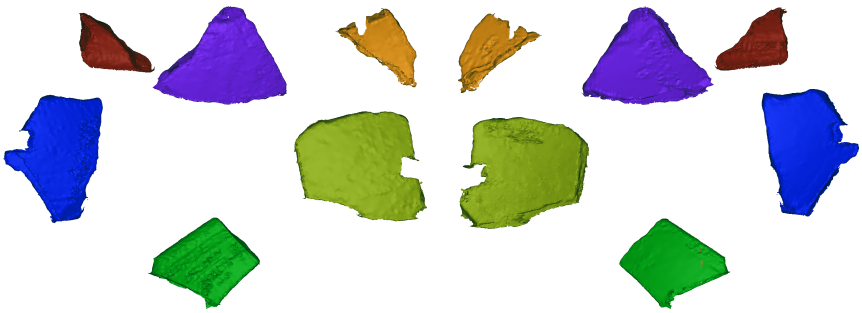

(a) (b)

Figure 5.1: (a) Frontview and (b) Backview of sherds mounted into the frame after removal of noise. The level of gray corresponds to the label number of each surface/sherd.

1. Estimate the indices of neighboring triangles and assign the (initial) label number 0 (unlabeled) for each triangle.
2. Increase the label number by one.
3. Search for the first triangle that has not been labeled.
4. Set the label nr for this triangle and for the neighboring triangles and set the counter of labeled triangles to 1

[1] *MB... Megabyte...* 1.048.576 *Bytes*

5. Search for labeled triangles with unlabeled neighbors.

6. Increase the counter number by the number of newly labeled neighbors.

7. Repeat step 5 and 6 until the counter does not change.

8. Return to step 2 until all triangles have been labeled.

Iterative methods theoretically have longer execution times than recursive methods, because the number of iterations is larger than for recursive methods. Therefore we had to approximate the number of iterations for typical surface to assure that the chosen method can be executed in a reasonable time ($>$ 1 minute). As the triangles generally have three neighbors, we can estimate the number of iterations by $\sqrt{m}$, where m is the number of triangles. This means that processing of largest ceramics requires 10 times the time required for the smallest sherds. As practical experiments showed, we can process small sherds with today's computers in less than 3 seconds and therefore we can also process large ceramics in less than 30 seconds. Figure 5.2a shows a typical triangle with its three neighbors. The three neighbor triangles therefore have only one neighbor. Triangles having one or two neighbors are typical for triangles located at the border.

This iterative search furthermore performs a detection of triangles with more than one neighboring triangle per edge. Such structures are called floating data and are introduced during registration of the $2\frac{1}{2}$D-images along the borders of overlapping surfaces due to distorted triangles. The floating data has to be removed, because they break our profile lines by adding "T"-junctions, which means that the profile line is no longer a closed polygonal line. Consequently an open polygonal line would require unnecessary manual inspection and correction of the profile line. As floating data has been detected in less than 15% of the 3D-models and the number of floating data is typically less than 1% of the triangles, we can remove floating data without loss of required information and assure a correct estimation of the profile line. Figure 5.2b,c shows an example for floating data. It shows a triangle with four neighbors.

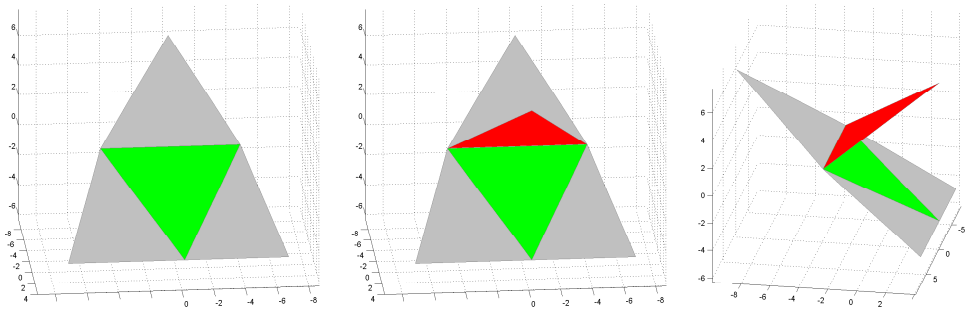

(a) (b) (c)

Figure 5.2: (a) Triangle (light gray) and its neighbors (medium gray). (b) Frontview and (c) Sideview of a triangle (light gray), its neighbors (medium gray) and a fourth neighbor (dark gray, floating data).

5.1.1 Geodesic Patches

After performing the previously described steps, we have removed all kinds of noise and errors introduced by the acquisition. This means we could apply the estimation of the rotational axis for orientation for plain (rotationally symmetric) sherds. As sherds are generally not plain, because the rotational symmetry is broken by the fracture, applications and decorations, we have to remove these distortions of symmetry before we can apply the estimation of the rotational axis.

As the method for orientation of sherds is inspired by the archaeological method, we follow this paradigm and use only the inner side of a sherds as input for the estimation of the rotational axis. This can be done because the inner side of a ceramic has generally not been decorated. The exception are small distortions from small decorations (stamps) and traces from usage. These distortions and the detection of the inner side of a sherd can be done by segmentation of the surface using curvature estimation [FJ89, TF95].

The surfaces of our sherds are discrete and therefore we have to estimate the curvature localy along the surface. The simplest and fastest way of finding a local area is a *k-ring*. A *k-ring* is estimated by collecting all triangles belonging to edges, which can be reached by k iterations following connected edges from a certain vertex. The problem of the *k-ring* are the results for surfaces having no equilateral triangles. Figure 5.3a shows a *k-ring* for k= 20 for a synthetic fragment. The estimation of the distances r_{CB} between the vertices $\mathbf{v}_B$ of the border of the *k-ring* towards $\mathbf{v}_C$, shows a deviation of $\pm$22.7%. This deviation is increasing having triangles of different size as shown in Figure 5.3b for a sherd. For this example, with k= 5 the deviation is $\pm$33.0%.

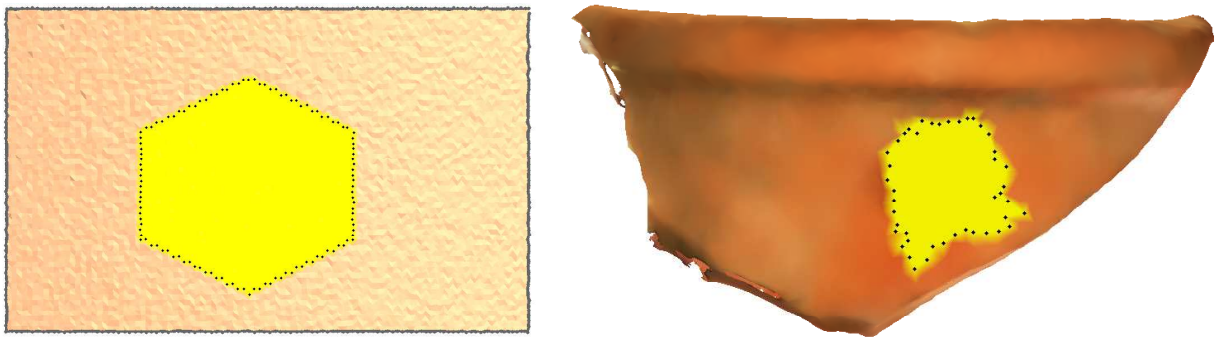

(a) (b)

Figure 5.3: *k-ring* (a) with k= 20 for a synthetic fragment and (b) with k= 5 a real sherd. The border vertices $\mathbf{v}_B$ of the *k-ring* are shown as black dots enclosing the *k-ring* shown as light gray area.

Therefore we choose to use geodesic patches to estimate local areas for curvature estimation as proposed in [NK02]. The geodesic patches are estimated using the geodesic distance [NK02] $g(\mathbf{v}_i)$ by the following algorithm, which has been inspired by [SA01] and adapted for our data-representation.

1. Set the geodesic distance for the seed vertex $\mathbf{v}_s$ to 0 and the maximum geodesic distance d_{max}. Set the geodesic distance for all vertices to infinite ($g(\mathbf{v}) = \infty$). Initialize a heap, which stores references to edges (of triangles). The heap is sorted ascending by a distance d_1 (primary) and d_2 (secondary). Furthermore the heap assures that d_1 and d_2 are exchanged, when $d_1 > d_2$.

2. Estimate the distance to the direct neighbors $\mathbf{v}_{r1}$ (1-ring neighborhood) using the length of the edges $d_{e_{sr1_i}} = |\mathbf{e}_{s_i}| = |\mathbf{v}_s\mathbf{v}_{r1_i}|$ of all triangles including $\mathbf{v}_s$.

3. Set the geodesic distance $g(\mathbf{v}_{r1_i}) = d_{e_{sr1_i}}$ for all $\mathbf{v}_{r1}$ with $d_{e_{sr1_i}} < d_{max}$. This is the initial geodesic patch, with vertices $\mathbf{v}_{gr1}$.

4. Estimate all edges $\mathbf{e}_{gr1}$ of triangles linking $\mathbf{v}_{gr1}$.

5. Push the edges $\mathbf{e}_{gr1_j} := \{\mathbf{v}_s, \mathbf{v}_{gr1_j}\}$ together with the geodesic distances $d_1 = g(\mathbf{v}_s)$ and $d_2 = g(\mathbf{v}_{gr1_j})$ on the heap. This concludes the initiation.

6. Pop an edge $\mathbf{e}_i := \{\mathbf{v}_{ei1}, \mathbf{v}_{ei2}\}$ with the geodesic distances d_{i1} and d_{i2}.

7. Repeat the previous step until $d_{i2} < d_{max}$ or the heap is empty. Is the heap empty all vertices of the geodesic patch have been estimated and the algorithm terminates, returning a list of the vertices $\mathbf{v}_g$ with $g(\mathbf{v}_g) < d_{max}$ and their geodesic distances $g(\mathbf{v}_g)$.

8. Estimate the triangle containing the vertices $\mathbf{v}_{ei1}$ and $\mathbf{v}_{ei2}$ in opposite order, because the vertices describing a triangle $\mathbf{t}_j := \{\mathbf{v}_{ei2}, \mathbf{v}_{ei1}, \mathbf{v}_j\}$ are ordered (clock-wise) and therefore we prevent moving back towards $\mathbf{v}_s$. In case no triangle is found return to step 6.

9. Estimate the geodesic distance $g(\mathbf{v}_j)'$ using Equation 5.1 with $\mathbf{v}_A = \mathbf{v}_{ei1}$, $\mathbf{v}_B = \mathbf{v}_{ei2}$, $\mathbf{v}_C = \mathbf{v}_j$.

10. Is $g(\mathbf{v}_j)'$ lower than a previously estimated geodesic distance $g(\mathbf{v}_j)$, set $g(\mathbf{v}_j) = g(\mathbf{v}_j)'$. Is $g(\mathbf{v}_j)' > g(\mathbf{v}_j)$ continue without changes.

11. Push the two edges $\mathbf{e}_{j1} := \{\mathbf{v}_{ei1}, \mathbf{v}_j\}$, $\mathbf{e}_{j2} := \{\mathbf{v}_j, \mathbf{v}_{ei2}\}$ on the heap.

12. Return to step 6.

Equation 5.1 is an approximation for the geodesic distance, assuming a virtual triangle $t_O := \{\mathbf{v}_B, \mathbf{v}_O, \mathbf{v}_A\}$ with the geodesic distances $|\mathbf{v}_O\mathbf{v}_A| = g(\mathbf{v}_A)$ and $|\mathbf{v}_O\mathbf{v}_B| = g(\mathbf{v}_B)$ as edge lengths. The neighboring triangle is abbreviated $t_j := \{\mathbf{v}_A, \mathbf{v}_C, \mathbf{v}_B\}$ for Equation 5.1. The angles α and β are required to determine the case, when the geodesic path intersect the edge $\mathbf{v}_A\mathbf{v}_B$ ans when it does not intersect it.

$$\alpha_O = \arccos \frac{|\mathbf{v}_A\mathbf{v}_B|^2 + g(\mathbf{v}_A)^2 - g(\mathbf{v}_B)^2}{2g(\mathbf{v}_A)|\mathbf{v}_A\mathbf{v}_B|} \ , \ \alpha_j = \arccos \frac{|\mathbf{v}_C\mathbf{v}_A|^2 + |\mathbf{v}_A\mathbf{v}_B|^2 - |\mathbf{v}_B\mathbf{v}_C|^2}{2|\mathbf{v}_A\mathbf{v}_B||\mathbf{v}_C\mathbf{v}_A|} \ ,$$

$$\beta_O = \arccos \frac{g(\mathbf{v}_B)^2 + |\mathbf{v}_A\mathbf{v}_B|^2 - g(\mathbf{v}_A)^2}{2|\mathbf{v}_A\mathbf{v}_B|g(\mathbf{v}_B)} \ , \ \beta_j = \arccos \frac{|\mathbf{v}_A\mathbf{v}_B|^2 + |\mathbf{v}_B\mathbf{v}_C|^2 - |\mathbf{v}_C\mathbf{v}_A|^2}{2|\mathbf{v}_B\mathbf{v}_C||\mathbf{v}_A\mathbf{v}_B|} \ ,$$

$$\alpha = \alpha_O + \alpha_j \ , \ \beta = \beta_O + \beta_j$$

$$g(\mathbf{v}_C)' = \begin{cases} g(\mathbf{v}_A) + |\mathbf{v}_A\mathbf{v}_C| & \text{for } \alpha \geq 180° \\ g(\mathbf{v}_B) + |\mathbf{v}_B\mathbf{v}_C| & \text{for } \beta \geq 180° \\ \sqrt{|\mathbf{v}_A\mathbf{v}_C|^2 + g(\mathbf{v}_A)^2 - 2|\mathbf{v}_A\mathbf{v}_C|g(\mathbf{v}_A)\cos\alpha} & \text{for } \alpha < 180° \wedge \beta < 180° \end{cases} \tag{5.1}$$

Figure 5.4a shows five randomly selected vertices of a sherd (shown in Figure 1.2) and their neighboring vertices with $g(\mathbf{v}_n) < d_{max}$, with $d_{max} = 3\ mm$. The level of gray corresponds to $g(\mathbf{v}_n)$ - black means $g(\mathbf{v}_n) = 0$ and white $g(\mathbf{v}_n) = d_{max}$. The remaining vertices are shown with their texture color. The border vertices $\mathbf{v}_{n_b}$ of the geodesic patch and vertices $\mathbf{v}_b$ on the border of the surface itself are shown as dark gray line. Figure 5.4b shows the geodeisc patch in the center of Figure 5.4a in detail. The medium gray lines are the edges $\mathbf{e}_i$ describing the triangles $\mathbf{t}_i$. The dark gray dots are $\mathbf{v}_{n_b}$.

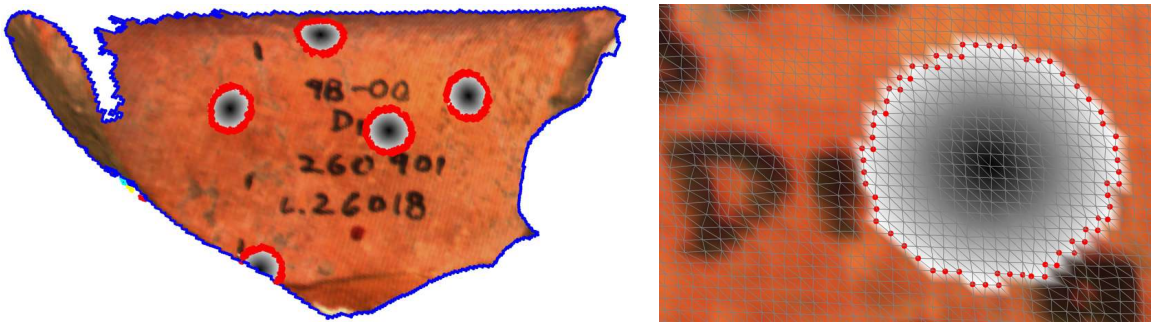

(a) (b)

Figure 5.4: (a) Inner side with 5 random vertices and their geodesic neighborhood $d_{max} = 3\ mm$. The level of gray corresponds to the geodesic distance $g(\mathbf{v}_n)$ - darker means closer. (b) Detail of one of the 5 random points. The dark gray dots are the border vertices $\mathbf{v}_{n_b}$ of the geodesic patch.

5.1.2 Curvature

Having the geodesic patches we estimate the curvature $\varkappa_i$ for all vertices $\mathbf{v}_i$ of the sherd to detect the inner side of the sherd using the sign of $\varkappa$. If $\varkappa_i$ has a negative sign, then the vertex belongs to a concave area and therefore it is part of the inner side. All vertices and the triangle they belong to, are part of the inner side for estimation of the rotational axis. Furthermore we dedect and remove small distortions of the inner side by $\overline{\varkappa} << \varkappa_j$ [TF95].

The geodesic patches are sets of vertices $\mathbf{v}_g$, which are neighbors of a vertex, which are within a certain geodesic distance. The geodesic distance set is typical 3 mm to 6 mm depending on the size of the sherd. This is done by the following steps, which transform $\mathbf{v}_g$, so that a second degree polynomial function $f(x, y)$ can be fitted. First the vertices $\mathbf{v}_b$ on the border of the geodesic patch are estimated. Then the center of gravity $\overline{\mathbf{v}_b}$ of $\mathbf{v}_b$ is estimated. All vertices ($\mathbf{v}_g \cup \mathbf{v}_b$) are shifted by $-\overline{\mathbf{v}_b}$. For estimation of the orientation of the patch the eigenvectors $\mathbf{E}$ of $\mathbf{v}_{b0} = \mathbf{v}_b - \overline{\mathbf{v}_b}$ are estimated using the singular value decomposition (SVD [ABB+99]). The vertices $\mathbf{v}_g$ are transformed by $\mathbf{v}'_{g_i} = \mathbf{v}_g\mathbf{E},\ \mathbf{v}'_{g_i} = (x_i, y_i, z_i)^T,\ i = 1, .., n$, where n is the number of vertices $\mathbf{v}_g$. Finally the curvature $\varkappa$ for $f(x, y)$ is estimated using Equation 5.2 based on [VH96].

$$\begin{pmatrix} a \\ b \\ c \\ d \\ e \\ f \end{pmatrix} = \begin{pmatrix} x_1^2 & y_1^2 & x_1y_1 & x_1 & y_1 & 1 \\ \vdots & \vdots & \vdots & \vdots & \vdots & \vdots \\ x_i^2 & y_i^2 & x_iy_i & x_i & y_i & 1 \\ \vdots & \vdots & \vdots & \vdots & \vdots & \vdots \\ x_n^2 & y_n^2 & x_ny_n & x_n & y_n & 1 \end{pmatrix} \setminus \begin{pmatrix} z_1 \\ \vdots \\ z_i \\ \vdots \\ z_n \end{pmatrix}$$

$$h_x = 2ax_2 + cy_2 + d,\ h_y = 2by_2 + cx_2e,$$

$$h_{xx} = 2a,\ h_{yy} = 2b,\ h_{xy} = c$$

$$\varkappa = \frac{h_{xx}h_{yy} - h_{xy}^2}{(1 + h_x^2 + h_y^2)^2} \tag{5.2}$$

As we have a $2\frac{1}{2}$D-image of the inner and outer side of the sherd, we can determine between the inner side and the outer using the overall sign curvature. Has the surface more geodesic patches with a negative sign than with a positive sign, than the surface is convex and tagged as inner view, because this $2\frac{1}{2}$D-image is used for further processing. The outer side could also be used for estimation of the rotational axis, but this side may have applications like handles and decorations, which are generally not present on the inner side. These applications are not trivial to detect, because they may appear in different size, shape and fractured. Therefore we consider a rotational axis estimated using the outer view as an extra validation if it is equal to the rotational axis estimated based on the inner side. If the axis estimated using the outer side does not equal the axis using the inner side, a tag can be set for manual inspection, because either the estimation of the rotational axis has failed, or the outer side of the sherd was not rotationally symmetric due to decorations.

Figure 5.5a shows the estimated curvature of the sherd from Figure 5.4. Dark color means high curvature, light color means low curvature. The areas of high curvature are the fracture of the sherd and areas next to the rim, where the sherd is worn from usage. The vertices with high curvature are discarded for estimation of the rotational axis Furthermore vertices of geodesic patches having vertices $\mathbf{v}_b$ of the border are discarded. Figure 5.5b shows the remaining surface after discarding these vertices from Figure 5.5a.

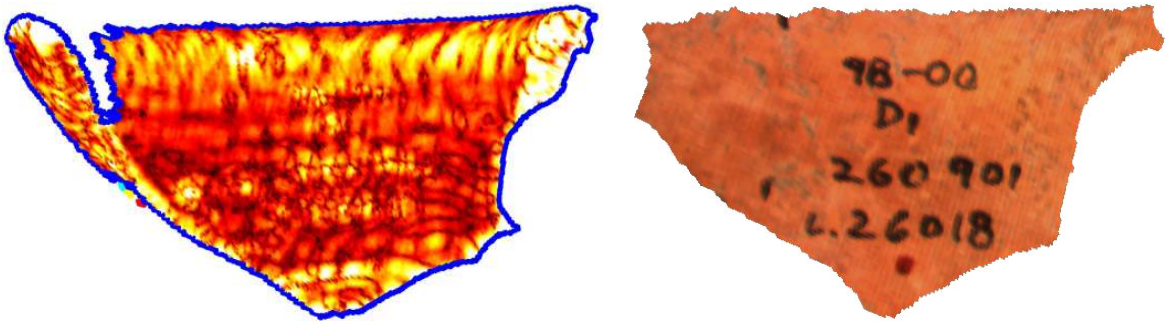

(a) (b)

Figure 5.5: (a) Curvature of the inner side of the sherd from Figure 5.4. Darker means higher curvature, lighter means low curvature. (b) The remaining surfaces after discarding vertices with high curvature and next to the border.

5.2 Estimation of the Profile Line

After removing the distortions of rotational symmetry using the curvature, the estimation of the axis of rotation is applied as shown in Chapter 4. Having the rotational axis and therefore the orientation of the sherd, we can estimate profile lines defined by the rotational axis and any point of the surface of the sherd. Archaeologists require only the longest profile line. In general this profile line can be estimated by the intersection of one plane using the point, where the sherd has it highest elongation (h_{max}). We choose not to rely on simply extracting a profile line using h_{max}, because for complex fractures the profile line has to be estimated using two or more profile lines, which connect to a virtual longest profile line. Especially this is required, when several sherds have been glued together, resulting in a larger fragment of a ceramic. Furthermore we require a measurement to evaluate the estimation of the profile line.

Therefore we choose to extract multiple profile lines along the circumference of the 3D-model using multiple intersecting planes p_n. Practical experiments have shown that an angle between the intersecting plane of 5° for small sherds and 20° for large sherds have the best ratio between performance and accuracy. Figure 5.6a,b shows a correct orientated sherd and its profile line ($\mathbf{v}_{pt_n}$) using e_i. Figure 5.6c shows the profile lines from sherd D2-L19736-306141-10 estimated using an invalid rotational axis. The estimation of the axis failed for this sherd, because the sherd is very small ($< 30 \times 30\ mm$) and flat.

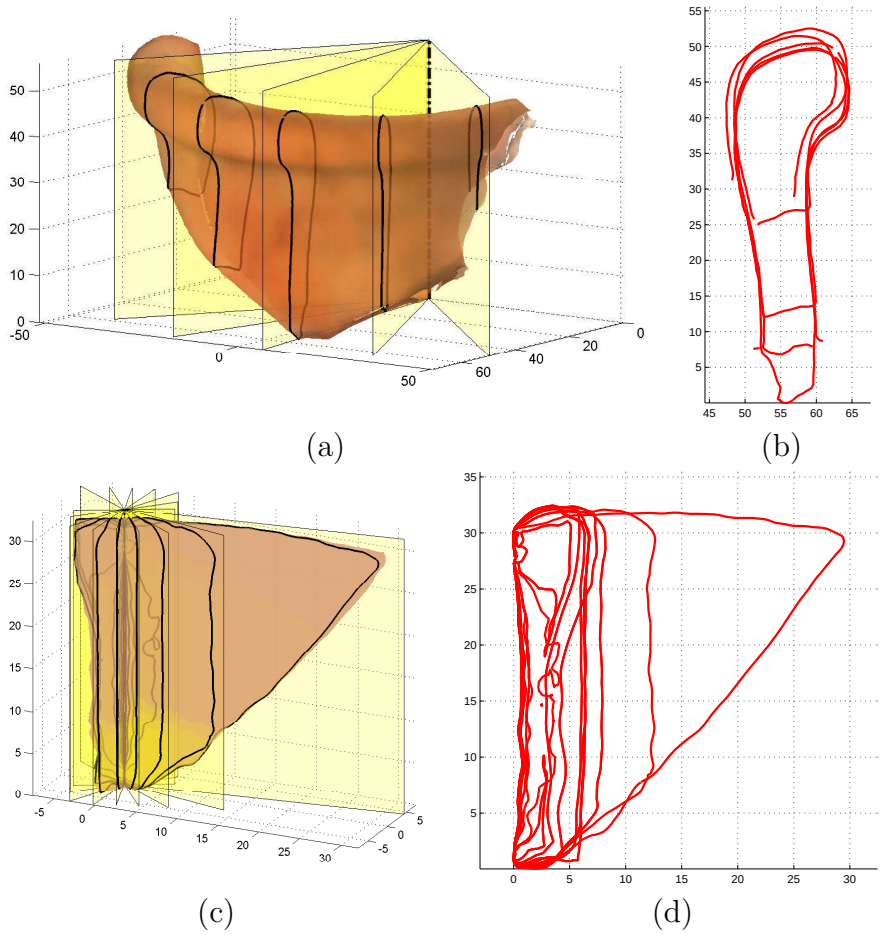

Figure 5.6: (a) Sample of multiple intersecting planes p_n and the (b) multiple profile lines (v_{pt_n}) using a correct estimated rotational axis for sherd "98-00 D1 260901". (c) p_n and (d) multiple profile lines from sherd "D2-L19736-306141-10", where no valid rotational axis could be estimated, because it was too flat.

For the automatic evaluation of the estimation of the rotational axis and therefore the profile line, the centers of gravity of the multiple profile lines are estimated. As these centers of gravity are distorted by the breakage, only 50° of the centers next to the center of gravity of the sherd are used for validation. In theory the centers of gravity should be aligned on an arc of a circle. Due to distortions we fit a circle [GGS94] and estimated the deviation of the centers to the circle. Is the deviation larger than the thickness of the wall of the sherd, the result is tagged as invalid for manual inspection, because there also exist vessels (coarse ware), which have not been manufactured properly.

Having the intersections $\mathbf{v}_{pt}$ between a plane $\mathbf{p}$ and the edges $\mathbf{e}$ of the triangles $\mathbf{t}$ is not sufficient, because $\mathbf{v}_{pt}$ have to be ordered to determine the characteristic point for classification. The first step of linking is the estimation of the pairs of edges $\mathbf{e}_i := (\mathbf{v}_{t_{k_1}}, \mathbf{v}_{t_{k_2}})$ and $\mathbf{e}_j := (\mathbf{v}_{t_{k_2}}, \mathbf{v}_{t_{k_3}})$ of a triangle $\mathbf{t}_k$, where its edges $\mathbf{e}_{12}$ and $\mathbf{e}_{23}$ are intersected at $\mathbf{v}_{pt_{12}}$ and $\mathbf{v}_{pt_{23}}$. The next step is linking $\mathbf{v}_{pt_{12}}$ and $\mathbf{v}_{pt_{23}}$ to an edge $\mathbf{e}_k$. This link has a well-defined di-

rection given by the data-structure, which consists of triangles having the vertices ordered clock-wise. Two edges $\mathbf{e}_{k_i} := \{\mathbf{v}_{pti_{12}}, \mathbf{v}_{pti_{23}}\}$ and $\mathbf{e}_{k_j} := \{\mathbf{v}_{ptj_{12}}, \mathbf{v}_{ptj_{23}}\}$ are connected when $\mathbf{v}_{pti_{23}} = \mathbf{v}_{ptj_{12}}$. To increase performance the search for $\mathbf{v}_{pti_{23}} = \mathbf{v}_{ptj_{12}}$ can be minimized using the order in the data-structure. This is done by the following recursive algorithm (steps 5 to 7) and its recursive calls in steps 8 and 9:

1. Estimate the normal distance d_n between all vertices $\mathbf{v}_n$ and the plane $\mathbf{p} = (p_1, p_2, p_3, p_4)^T$.
2. Find all intersected triangles $\mathbf{t}_p := \{\mathbf{v}_{p1}, \mathbf{v}_{p2}, \mathbf{v}_{p3}\}$ having distances $d_{pi} = |\mathbf{v}_{pi}\mathbf{p}|$ with different signs.
3. Tag all $\mathbf{t}_p$ as unprocessed.
4. Select the first unprocessed triangle $\mathbf{t}_{pi} := \{\mathbf{v}_a, \mathbf{v}_b, \mathbf{v}_c\}$.
5. Estimate the intersected edges $\mathbf{e}_{i12} := \{\mathbf{v}_a, \mathbf{v}_b\}$ and $\mathbf{e}_{i23} := \{\mathbf{v}_a, \mathbf{v}_b\}$.
6. Estimate and link the intersections $\mathbf{v}_{pit_{12}}$ and $\mathbf{v}_{pit_{23}}$.
7. Search for two neighboring triangles $\mathbf{t}_j := \{\mathbf{v}_b, \mathbf{v}_a, \mathbf{v}_d\}$ and $\mathbf{t}_k := \{\mathbf{v}_c, \mathbf{v}_b, \mathbf{v}_e\}$.
8. If $\mathbf{t}_j$ exists apply steps 5 to 7 and link $\mathbf{v}_{pit_{12}}$ with $\mathbf{v}_{pjt_{12}}$.
9. If $\mathbf{t}_k$ exists apply steps 5 to 7 and link $\mathbf{v}_{pit_{23}}$ with $\mathbf{v}_{pkt_{23}}$.
10. Return to step 4 until all triangles are processed.

Step 10 is necessary because the 3D-model might not be a perfectly closed surface, as parts of the surface may be missing due to shading effects during the acquisition. Missing parts are called holes. If $\mathbf{p}$ intersects two or more holes, then the profile line is not continuous, but it is ordered and therefore characteristic points can be estimated. The profile line is represented by one or more polygonal line segments. Finally the 3D-coordinates of $\mathbf{v}_{pt}$ are transformed into 2D-coordinates of the intersecting plane $\mathbf{p}$ with the axis of rotation as y-axis and the x-axis orthogonal through the vertex with minimum height h_{min}.

The next section shows the application of these algorithms applied to synthetic rotational fragments. The results for real data are shown in Chapter 6.

5.3 Experiments with Synthetic Data

This section shows the results for application of the methods shown in the previous sections applied on synthetic data. The synthetic data used for these experiments is the same as used in Chapter 4. We begin with experiments regarding the removal of noise, estimation of geodesic distance, geodesic patches and curvature. Finally we show the estimation of the profile line by estimation of the rotational axis using circle templates as proposed in Chapter 4.

5.3.1 Removal of Noise

The removal of noise by area and intensity of color was automatically applied on all our synthetic objects shown in this section. The size and the border of all objects has been estimated correctly. To test the removal of dark and bright triangles we changed the color of parts of the meshes used to evaluate the geodesic patches. Figure 5.7a shows a synthetic fragment of an s-shaped object with black areas, like the clamps of our frame. Furthermore the black parts have small bright spots. Figure 5.7b shows the same fragment after removal of the dark areas. The bright spots remain as 30 small surfaces ($< 1\ mm^2$). The borders of the surfaces are shown as thick lines in different levels of gray for each surface tag. Figure 5.7b shows the fragment after removal of dark areas. Figure 5.7c shows the fragment after removal of all surfaces of a size less than 100 mm.

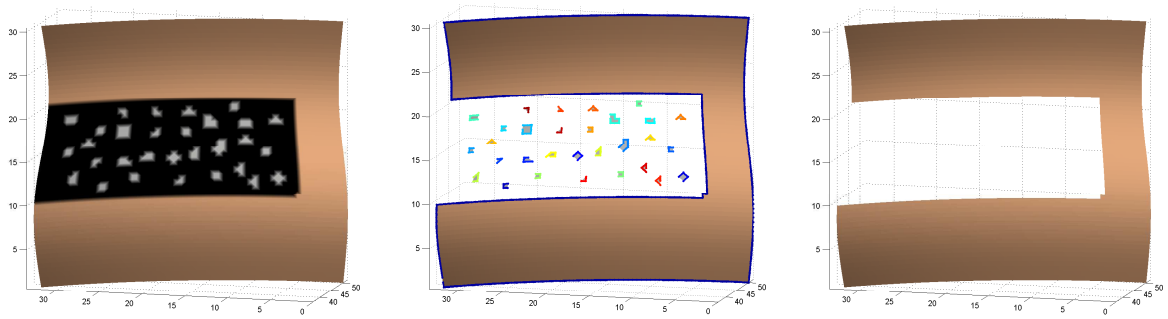

(a) (b) (c)

Figure 5.7: Synthetic fragment with (a) bright small spots in dark areas (b) after removal of the dark areas. The borders of the areas are shown as thick line with different levels of gray corresponding to the tag of the area. (c) Fragment after removal of dark and bright areas.

5.3.2 Geodesic Distance

For evaluation of the geodesic distance, which we use to find a certain neighborhood called geodesic patches; we first had to test the estimation of the geodesic distance. The geodesic distance is estimated by "walking" along the surface using the shortest path. Therefore we require a surface, which prevents "walking" directly from one point to another, which means that the geodesic distances does not equal the geometric distance for flat object. A "C"-shaped surface fulfills this requirement, which was chosen for our experiment. Therefore we estimated the geodesic distance between the two extreme points v_{C1} and v_{C2} of the "C". This shape has been chosen, because for a quadrangular surface the geodesic distance is identical to $|v_{C1}v_{C2}|$. Using the C-shaped surface, the path has to be the distance for diagonal "walking" upwards all along the "C'. Figure 5.8(b) shows the surface colored by the distance of all vertices towards v_{C1} - darker values mean closer. For evaluation we estimated length of different paths between v_{C1} and v_{C2}. First we have the geometric distance of $|v_{C1}v_{C2}| = 30\ mm$. The second path is directly "walking" from v_{C1} towards v_{C1} via the two inner corners of the "C", which has a path length of 74.77 mm. The length of this path would be equal to the geodesic distance for a flat fragment. The theoretical geodesic distance for surface described by the generating function (rotation of a sinus wave) of the fragment, would be 75.16 mm. The result for the application of our method is 75.40 mm. This means the error introduced by quantization of the surface and the approximation of the geodesic distance proposed by [SA01] has an acceptable error accumulated for geodesic paths, ten times longer than we use for the estimation of the rotational axis, of 0.3%.

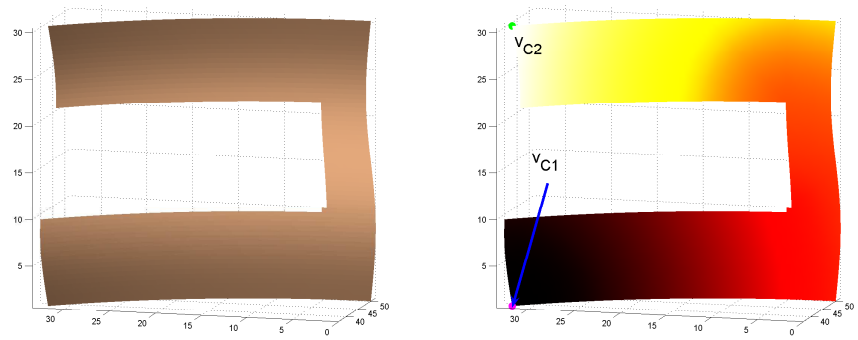

(a) (b)

Figure 5.8: (a) The fragment after removal of small areas for testing the geodesic distance. (b) Geodesic distance of all vertices towards the vertex shown in the bottom left corner. Darker vertices have a lower geodesic distance than brighter vertices.

For further experiments we used a synthetic unit-sphere ($2r = 1\ mm$) represented by 1584 triangles having a total surface area of 3.066 mm^2. The error of the area of 2.4% in respect to a perfect sphere having an area of $\pi\ mm^2$ is introduced by quantization into triangles. All geodesic patches with a maximum geodesic distance of $g_{1/2} = \pi/4$ have to cover half of the sphere. The application of our algorithm shows, that the area of the

geodesic patches $g_{1/2}$ covers 719 triangles having a total area of 1.353 mm^2. Therefore 95.2% of the half of the sphere is covered. The missing 4.8% is an error of the quantization of the sphere, because the missing area is covered by parts of the triangles along the border of the geodesic patch. This can be shown by the distances r_{CB} between the center vertex $\mathbf{v}_c$ and the border vertices $\mathbf{v}_B$ of the geodesic patch. The distances r_{CB} cover a maximum of 99.9%, an average of 96.0% and a minimum of 93.1% of the ideal value of $\pi/4$. This error could be minimized by subsampling the triangles along the border of the geodesic patches, which would cost additional performance, which gains a negligible precision, because the deviation even of perfectly estimated border vertices for real surface is generally larger than 6.9%.

Another test we applied in respect to real surfaces, is the estimation of the geodesic distance for the unit-sphere having holes. Therefore we remove randomly (normal distribution) triangles. The result was a sphere described by 1476 triangles covering a surface of 2.843 mm^2 having 19 holes. For this sphere we repeated the estimation of the geodesic distance to show that holes do not disturb the estimation. The distances r_{CB} having a sphere with holes cover a maximum of 98.9%, an average of 96.0% and a minimum of 92.2% of the ideal value of $\pi/4$. Comparing these results with the results from the sphere without holes, we can estimate a difference of less than one percentage point, which can be explained by the distortion by holes along the border along the geodesic patches.

Figure 5.9(a,b,c) shows one vertex and its geodesic patch $g_{1/2}$ for the sphere without holes. Figure 5.9(d,e,f) shows the same sphere with holes to test the estimation of the patches against missing parts of surface, which we expect from our real data. The geodesic distance for each vertex is shown as level of gray. Darker values mean lower geodesic distance, brighter values mean larger geodesic distance. The medium gray areas of the lower half of the sphere are vertices not reached by the geodesic patch $g_{1/2} = \pi/4$.

5.3.3 Curvature

The curvature has been evaluated using the synthetic s-shaped and cylindrical fragments. The cylindrical fragment has a constant curvature. The s-shaped fragment has a curvature which is constant only along the circumference. The curvature for this fragment is changing along its rotational axis. The experiments have been applied to fragments with and without noise already used in Section 4.5. Furthermore we engraved the word "EDGES" into the surface of these fragments. Engravings are common decorations, which have to be detected and removed, so that they do not influence the estimation of the rotational axis. The depth of the engraving was 1% of the objects radius ($\approx 5\ mm$), because this resembles the stamps and engravings applied to ceramics. Figure 5.10 shows the curvature of fragments with and without noise. Figure 5.10 show the curvature of the fragments with engravings as levels of gray, High negative curvature is shown as light-gray to white color, high positive curvature is shown as dark-gray to black color and low curvature is shown as medium gray. The contrast of Figure 5.10 has been enhanced to show the minor influence of noise between noisy and smooth surface and to show the engraved word.

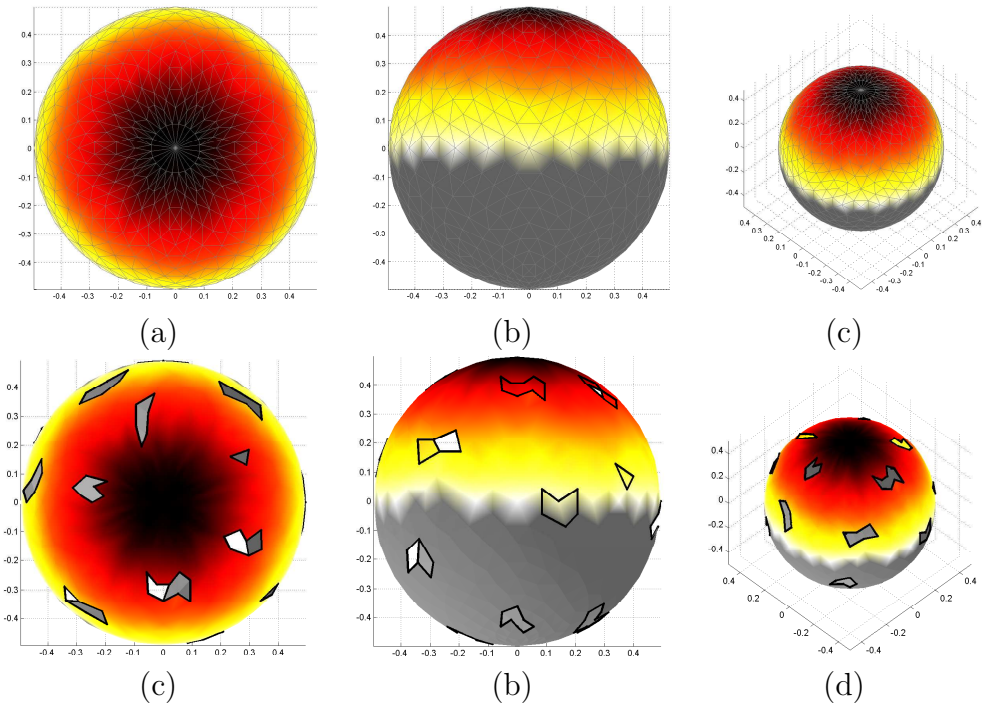

Figure 5.9: Unit-sphere with geodesic patch $g_{1/2} = \pi/4$: (a) view from the top, (b) view from the side and (c) an isometric view. Unit-sphere with holes and a geodesic patch $g_{1/2} = \pi/4$: (d) view from the top, (e) view from the side and (f) an isometric view. The borders of the holes are marked with black lines.

Figure 5.11 shows the fragments after removal of the engraving using the curvature.

5.3.4 Profile Line

The evaluation of the estimation of the profile line was done on the 24 synthetic fragments, using all the previous processing steps and the estimation of the rotational axis. Additionally we included the fragments with the engraving. The results for the estimated profile lines in respect to function used to generate the fragments by orientation corresponds as expected to Table 4.2. Therefore for the worst-case, which is the smallest fragment of the cone, the angle between the profile line and the generating function is 2.7°. Therefore this is the maximum angular error. All other fragments have an angular error less than 1.7°. For the radial error we have the same behavior. Therefore also the smallest cone-fragment has the maximum radial error of 2.2 mm. The noise of the points, under respect of radial and angular error, between the estimated profile line and the generating function is not measurable for the smooth fragments. The profile lines estimated of fragments with noise, have a noise of 13.7%. This corresponds to ≈2/3 of the noise, because the profile line is a two-dimensional line and therefore the distortions of the third dimension of the fragments have no influence. Figure 5.12 shows the profile lines having the worst-cases of noise.

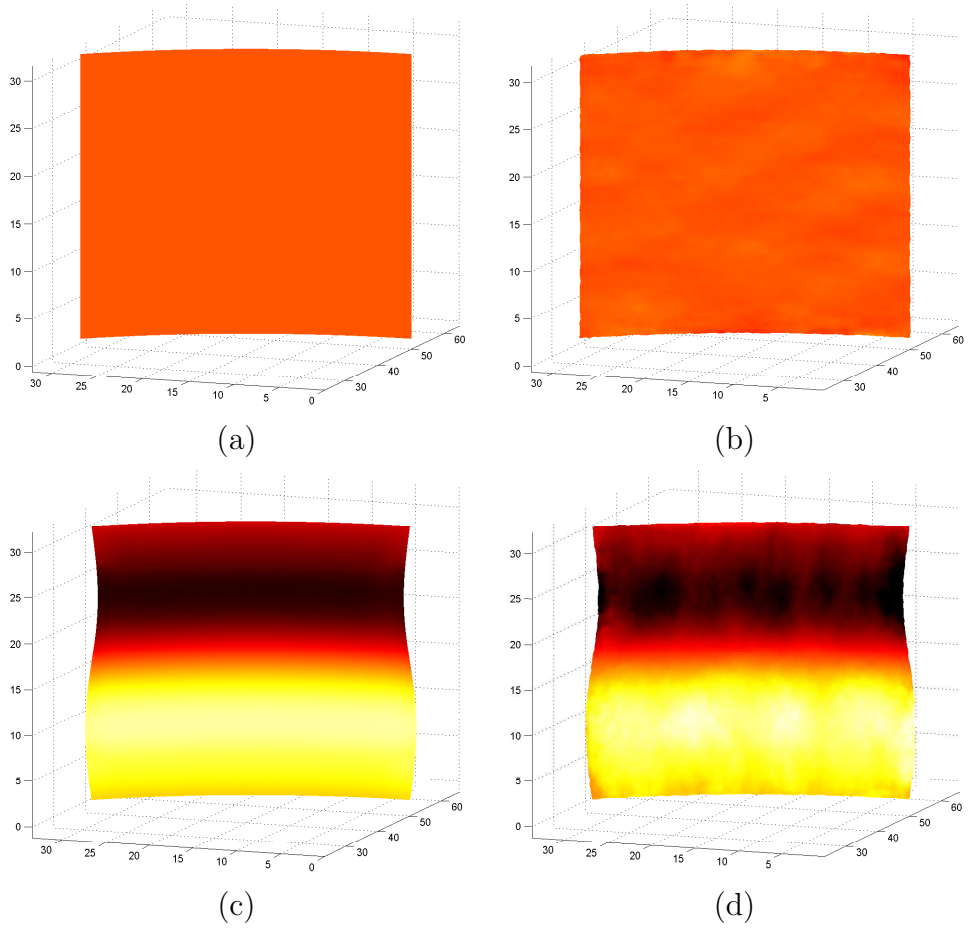

Figure 5.10: Curvature of a (a) smooth cylinder and (b) the same cylinder with noise. Curvature of a smooth s-shaped synthetic fragment (d) with and (c) without noise. The level of gray corresponds to the curvature: Dark and bright colors mean positive and negative high curvature. Medium gray means low curvature.

5.4 Summary

In this chapter we have shown how we remove noise and prepare the 3D-models acquired on archaeological excavations for estimation of the rotational axis. After application of estimation of the rotational axis, which was shown in the previous chapter, we have shown the estimation of the profile line using the rotational axis. Finally we have shown experiments with synthetic data to test our proposed method for processing of sherds. Therefore we could show that the errors from quantization and optimizations for performance do not introduce further errors, because the measurable errors of the estimated profile lines correspond directly to the error introduced by the estimation of the rotational axis.

The next chapter shows the results for application of the processing of sherds and the estimation of the rotational axis on real sherds in comparison with the *Profilograph* and the manual drawings of sherds selected by archaeologists,

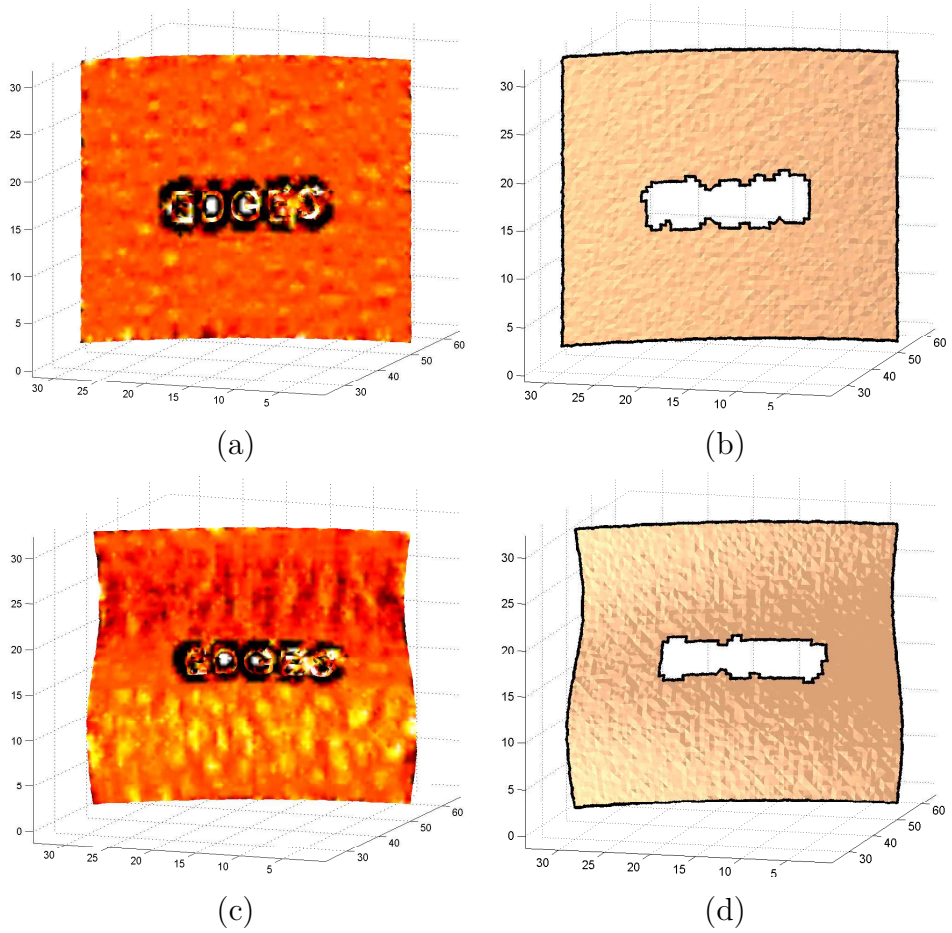

Figure 5.11: Curvature of an engraved (a) cylindrical fragment and (c) an engraved s-shaped synthetic fragment. (b,d) Fragments after removal of the engraving dedected using the curvature. The level of gray corresponds to the curvature: Dark and bright colors mean positive and negative high curvature. Medium gray means low curvature.

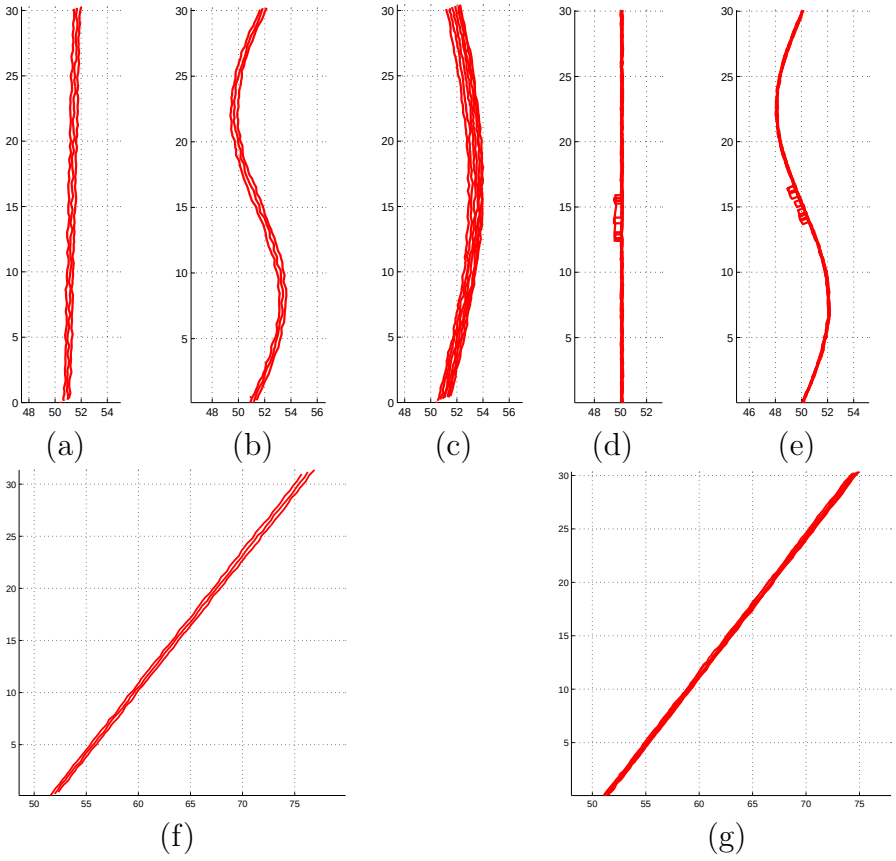

Figure 5.12: Worst-case examples of the estimated profile lines of our synthetic fragments with noise using the estimation of the rotational axis: (a) cylinder $\beta_{CM} = 20°$, (b) s-shaped $\beta_{CM} = 20°$, (c) sphere $\beta_{CM} = 40°$, (d) cylinder $\beta_{CM} = 40°$ with engraving, (e) s-shaped $\beta_{CM} = 40°$ with engraving, (f) cone with $\beta_{CM} = 20°$ and (g) $\beta_{CM} = 40°$.

Chapter 6

Results - Sherds

This chapter shows the comparison between profile lines of sherds acquired by manual drawing, *Profilograph* and estimated on the data acquired by the 3D-scanner. The comparison is done using shape analysis to determine the influence of expert knowledge on manual drawings for orientation of small sherds in respect to automated methods. Furthermore a comparison of precision and accuracy between the three methods of archaeological documentation is shown. Finally a conclusion is given.

There exists no general ground truth for profile lines of sherds, because only in rare cases enough sherds of a vessel are found to reconstruct it, which would give us the correct orientation. Therefore we applied tests with synthetic data and real data from well-known vessels. As these experiments have shown that smaller sherds are more error prone than large sherds, archaeologists gave us 25 of their smallest sherds for comparison of our method, the *Profilograph* and the manual drawing. The motivation behind this experiment was to see the influence of the expert knowledge for orientation of the sherds. Therefore the *Profilograph* and the 3D-scanner were operated by persons without archaeological skills, while the manual drawings were done by an archaeological draftsperson having more than ten years of experience in manually drawing profile lines.

The following three sections show the profile lines of 25 different sherds acquired for comparison. Further profile lines of sherds acquired by the 3D-scanner and the *Profilograph* are shown in Appendix A. At the beginning of each section, we show results from sherd "98-00 D1 260901", which has been introduced in Figure 1.3 and has been shown to illustrate the different processing steps of previous chapters.

6.1 Comparing Profile Lines

Before we begin with comparing profile lines, we require a method for comparison of profile lines. At the first glance it appears that the profile lines have to be almost identical and an intersection of the mean-normalized areas described by the profile lines can do the trick. This is almost true for comparing the *Profilograph* and the 3D-scanner, **if** it is extracted at the same position. Comparisons with the manual drawings are more com-

plicated, because archaeological draftspersons tend to draw the profile lines longer than they actually are. This can be done, because sherds can show evidence by their fracture or decorations, which give information about the further shape of a profile line, which only can be detected with a certain expert knowledge.

As the position (radii) of a profile line, its orientation and its shape are the relevant properties of a profile line, we split the comparison into two parts. First we estimate the radius $\overline{r}$ at the center of the profile line using the center of the medial axis [FEC02]. An alternative would be the radius of the center of gravity, but it may not be located within the profile line. Medial axis have been first introduced by [Blu67] and as their estimation is important for numerous applications, there exist numerous methods (e.g. [RJ66, ND97, KK02, TK98, SBTZ99]). As our profile lines are polygonal lines, we choose a novel method, based on Voronoi Diagrams [FEC02].

The second part is comparing the shapes of the profile lines regardless of their position. There exist also numerous methods for shape analysis for numerous applications (e.g. [SP94, BMP01, ALLT04, CC04, MKF04, PNN06]). As the major requirements for a method for comparing our profiles is the ability to handle open curves and the ability to ignore the shape at the beginning and at the end of the curve, we choose the method of [Tho03]. This method selects landmarks [HT00], which are used to minimize the distance between shapes [DTC+02] by rotation and scaling. Therefore we estimate the angle of rotation and the scaling factor s between the profiles from the 3D-scanner and the manual drawing. This is done by dividing the profile line changed by [Tho03] through the original profile line, which gives a 2×2 rotation matrix containing the cosinus of the angle of rotation β. The scaling factor is estimated in similar manner using a division of the output through the input profile line having the same orientation ($\beta = 0$). Figure 6.1 shows examples for the selected landmarks. Figure 6.1b shows how landmarks are set on profile lines with different length ignoring the extended open ends of the curve.

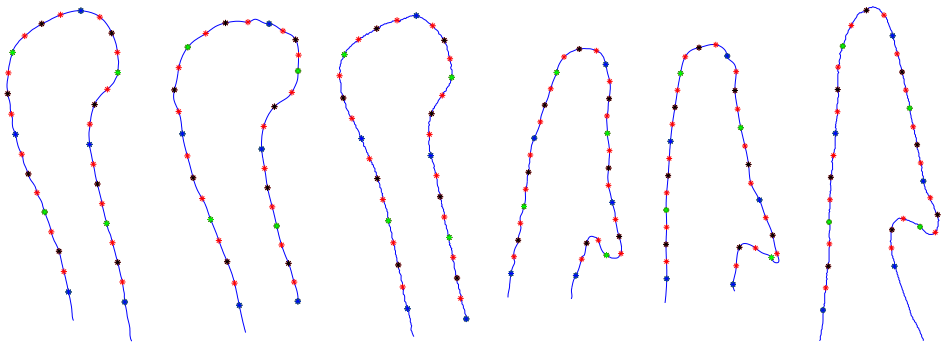

(a) (b)

Figure 6.1: Landmarks estimated using [Tho03] of the profile lines of sherd (a) "98-00 D1 260901" and (b) "D2-L19732-305940-6". From left to right: 3D-scanner, *Profilograph* and manual drawing. These figure repesent only the shape of the profile lines and therefore they are not shown in the same scale.

To get proper results using [Tho03] we had to assure that all profile lines have the same circular orientation. Therefore the outer angles between the line segments of the profile line is estimated. The sign of the sum of the outer angles corresponds to a clock-wise circular orientation for positive values and vice versa. We decided arbitrarily to orientate all profile lines clock-wise. Therefore all profile lines with a negative sum of angles have been reversed.

Furthermore we estimate the angle α of the main direction in respect to the rotational axis (equals y-axis) for basic classification into general types of ceramics like (e.g.) plate, bowl, jug. The main direction is estimated using the first component of the principal component analysis (*PCA* [DKK96, Jol02]) of the medial axis. The direction is represented as angle α between the first component and the rotational axis.

6.2 Manual Drawings

Figure 6.2a shows the pencil drawing of the profile line aligned along the rotational axis (vertical line on the left side). Figure 6.2b show the profile line with the center of the medial axis. It shows the radius $\overline{r_M}$ estimated by the center of the medial axis. The angle α_M used for basic classification into bowls ($\alpha \ll 0$), jugs ($\alpha \approx 0$) and plates ($\alpha \gg 0$). The grid-lines are spaced 10 mm. The Figures 6.3 and 6.4 show the same information like Figure 6.2b about the other manual drawings.

The numeric results are shown in Table 6.1. This tables shows the estimated radius $\overline{r_M}$, the maximum height h_{max} in mm. The angle α_M of the main direction of the medial axis towards the rotational axis is shown in degree. Furthermore the scaling factor s_e is shown, because the scaling given by archaeologists was not correct, neither it had a systematic error like introduced due to digitizing the drawing. For further comparison we used the manual profile lines corrected by s_e.

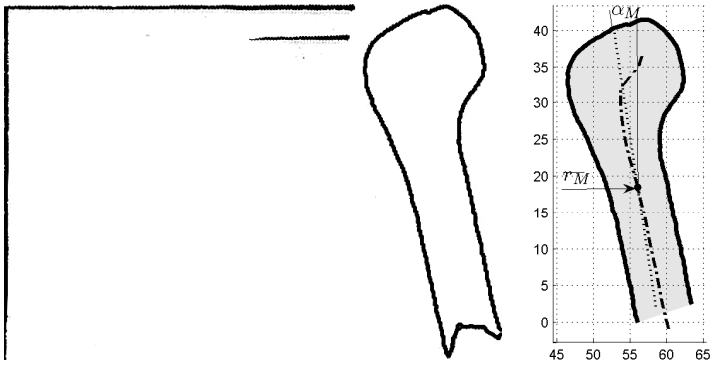

(a) (b)

Figure 6.2: Manual drawing of sherd "98-00 D1 260901" (a) before removal of manual lines for the rotational axis (vertical line) and the orifice plane (horizontal line). (b) Profile line with angle α_M of the main direction (dotted line) and the radius $\overline{r_M}$ of the center (dot) of the medial axis (dashed line).

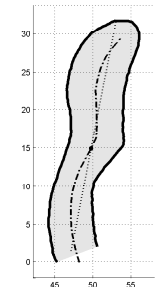

D2-L19720-305925-12

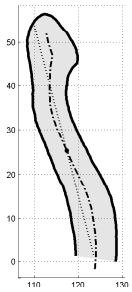

D2-L19732-305940-5

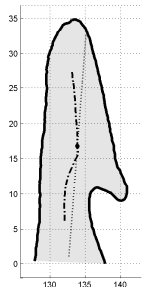

D2-L19732-305940-6

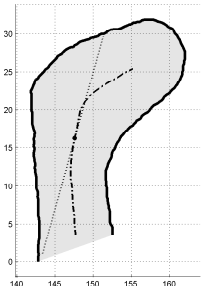

D2-L19732-305940-7

D2-L19732-305940-8

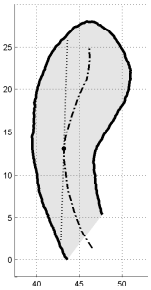

D2-L19736-306027-1

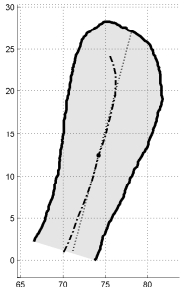

D2-L19736-306146-6

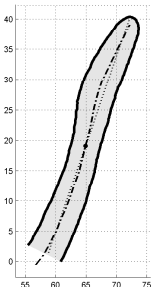

D2-L19739-305994-2

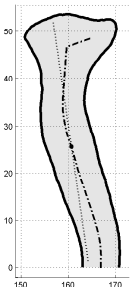

D2-19739-305994-4

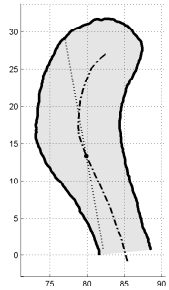

D2-L19742-305996-1

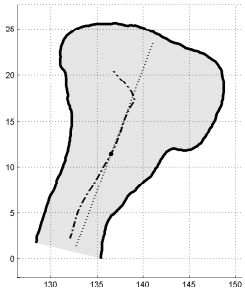

D2-L19742-305996-2

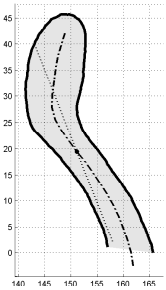

D2-L19742-305996-3

Figure 6.3: Profile lines estimated by manual drawing. The medial axis is shown as dashed line. The major direction of the medial axis is shown as dotted line.

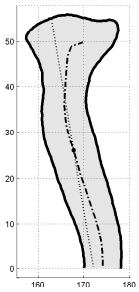

D2-L19742-305996-7

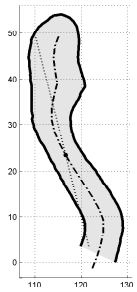

D2-L19743-306028-11

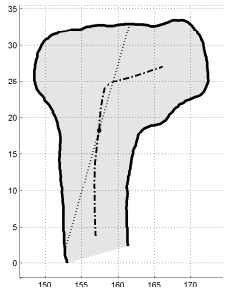

D2-L19743-306028-2

D2-L19743-306028-3

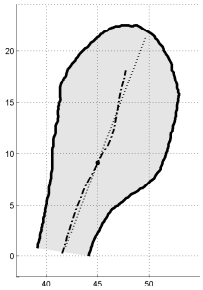

D2-L19743-306028-5

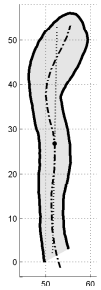

D2-L19743-306028-6

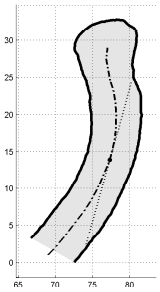

D2-L19743-306051-2

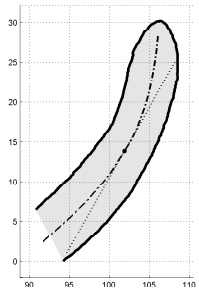

D2-L19751-306083-2

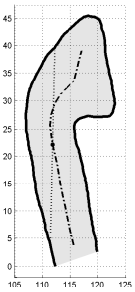

D2-L19766-306231-12

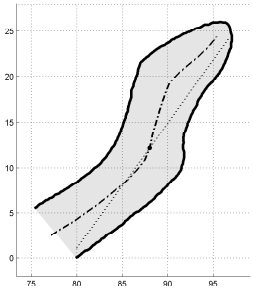

D2-L19766-306231-3

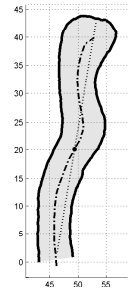

D2-L19766-306231-4

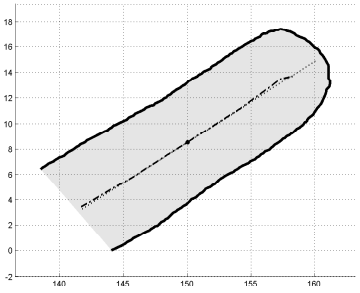

D2-L19766-306231-7

Figure 6.4: Profile lines estimated by manual drawing. The medial axis is shown as dashed line. The major direction of the medial axis is shown as dotted line.

Sherd No.	$\overline{r_{Mn}}$	h_{max}	$\overline{\alpha_{Mn}}$	s_e
D2-L19720-305925-12	49.45 mm	35.05 mm	11.01°	11.27%
D2-L19732-305940-5	118.17 mm	62.82 mm	-14.44°	9.59%
D2-L19732-305940-6	133.16 mm	38.51 mm	4.37°	17.13%
D2-L19732-305940-7	148.49 mm	36.08 mm	15.54°	49.52%
D2-L19732-305940-8	166.72 mm	73.10 mm	-10.43°	17.94%
D2-L19736-306027-1	44.58 mm	30.24 mm	1.84°	2.34%
D2-L19736-306146-6	73.97 mm	31.45 mm	14.94°	63.62%
D2-L19739-305994-2	64.87 mm	43.77 mm	19.05°	13.85%
D2-L19739-305994-4	162.52 mm	59.78 mm	-8.30°	14.01%
D2-L19742-305996-1	81.36 mm	35.35 mm	-10.29°	28.69%
D2-L19742-305996-2	135.78 mm	29.55 mm	20.59°	13.68%
D2-L19742-305996-3	152.91 mm	51.10 mm	-21.52°	25.99%
D2-L19742-305996-7	169.31 mm	62.41 mm	-9.54°	18.94%
D2-L19743-306028-11	118.23 mm	59.99 mm	-14.16°	21.04%
D2-L19743-306028-2	157.99 mm	37.96 mm	15.91°	17.66%
D2-L19743-306028-3	138.80 mm	72.70 mm	-4.26°	22.89%
D2-L19743-306028-5	44.56 mm	24.91 mm	20.84°	26.81%
D2-L19743-306028-6	51.93 mm	61.46 mm	1.11°	16.08%
D2-L19743-306051-2	75.70 mm	35.30 mm	15.61°	9.15%
D2-L19751-306083-2	100.26 mm	31.91 mm	29.39°	21.28%
D2-L19766-306231-12	113.57 mm	50.53 mm	1.33°	22.29%
D2-L19766-306231-3	86.96 mm	27.47 mm	35.89°	7.22%
D2-L19766-306231-4	48.32 mm	48.34 mm	9.53°	13.06%
D2-L19766-306231-7	149.71 mm	18.35 mm	57.56°	16.64%
98-00 D1 260901	56.36 mm	46.20 mm	-8.62°	18.06%

Table 6.1: Average radius $\overline{r}$ at the center of the medial axis with a major tilt angle α_M towards the rotational axis (equals y-axis), maximum height h_{max} of the sherd and additional scaling-factor s_e of the manual drawings of the profile lines.

6.3 *Profilograph*

The data acquired by the *Profilograph* contains two profile lines. The first profile line corresponds to the manual drawing. It has a correct scale and it is orientated by setting the rotational axis parallel to the y-axis of the coordinate system. Therefore the height (e.g. h_{max}) can be estimated properly, but no radius can be estimated, because the offset between the rotational axis and the y-axis is not known.

Therefore, we have the second profile line, which has been estimated orthogonal to the rotational axis at the height of the center of gravity of the sherd. This horizontal profile line is divided into an inner profile and an outer profile. The inner and outer profile can be easily divided, because the breakage was not acquired and therefore we get one polygonal line for the inner and the outer part of the horizontal profile line. Into this two profile lines we fit two circles by minimizing the least square error [GGS94]. These two circles have the centers $\mathbf{x}_{0_{in}}$, $\mathbf{x}_{0_{out}}$ and the radii r_{in} and r_{out}.

As the circles are estimated at the same height as the center of the medial axis, we can estimate the average radius as $\overline{r}_P = \frac{r_{out}-r_{in}}{2}$. Furthermore we can estimate the distance between the centers $d_{x_0} = |\mathbf{x}_{0_{in}} - \mathbf{x}_{0_{out}}|$, which is an indicator for a proper acquisition. Figure 6.5a shows the horizontal profile line and the radii r_{in} of the inner side and r_{out} of the outer side. The distance between the centers d_{x_0} is shown. The grid-lines are spaced 50 mm. Figure 6.5b show the profile line with the center of the medial axis with radius $\overline{r}_P$. Analog to the manual drawing the angle α_P of the major direction of the medial axis is shown.

Table 6.2 at the end of this section shows the estimated radius $\overline{r}_P$, the distances d_{x_0}, the maximum height h_{max} and the wall thickness $d_r = r_{out} - r_{in}$ based on the horizontal profiles in mm. Furthermore the angle α_P towards the rotational axis is shown in °.

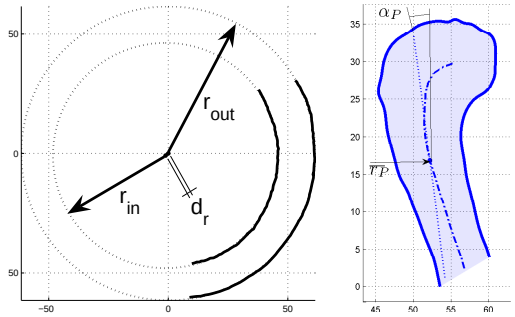

(a) (b)

Figure 6.5: Profile line of "98-00 D1 260901" acquired by the *Profilograph*. (a) Horizontal profile lines for estimation of the radii r_{in} and r_{out} and the distance between the circle centers d_{x_0}. (b) Profile line with radius $\overline{r}_P$ and angle of orientation α_P.

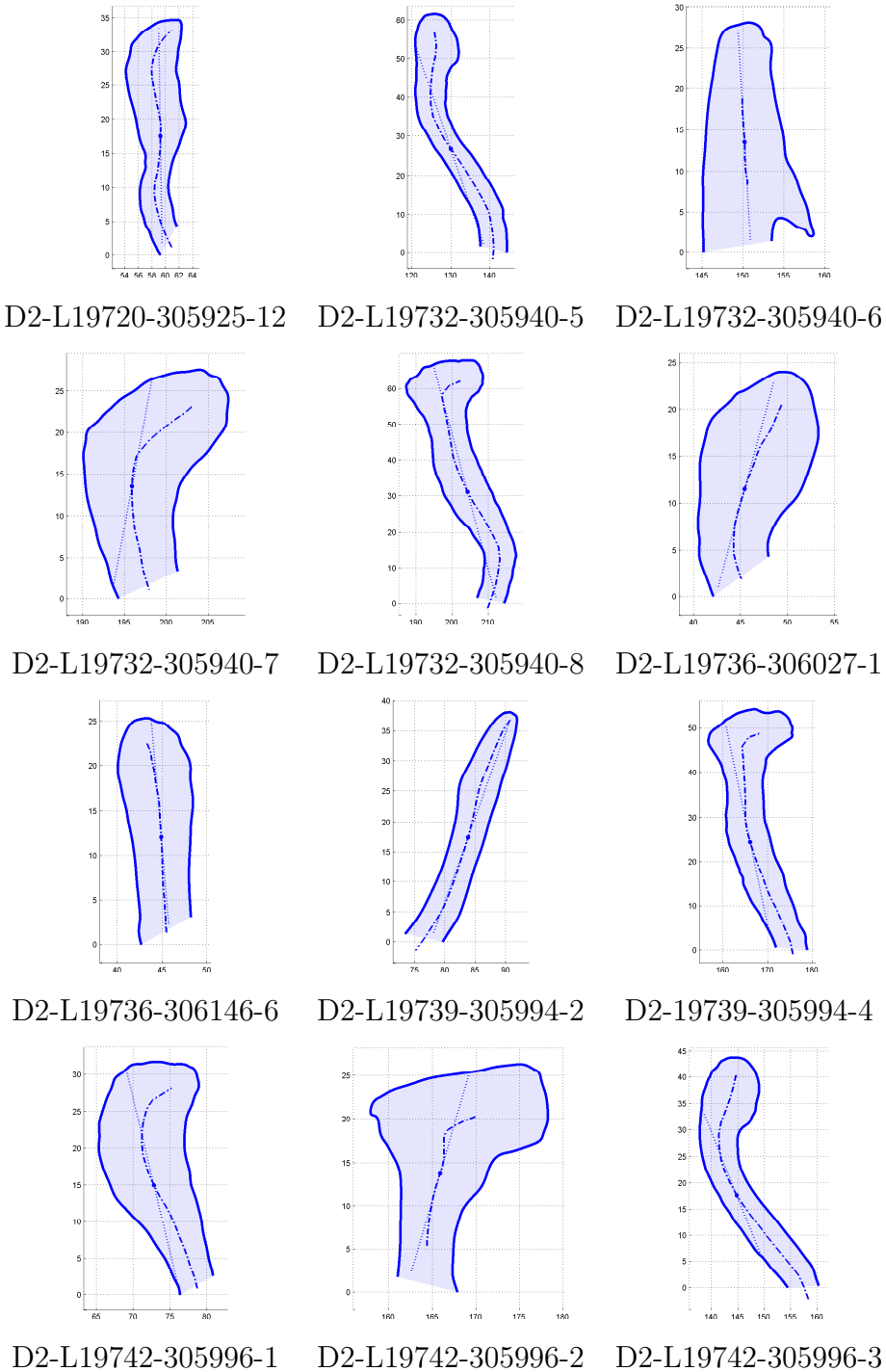

Figure 6.6: Profile lines estimated using the *Profilograph*. The medial axis is shown as dashed line. The major direction of the medial axis is shown as dotted line.

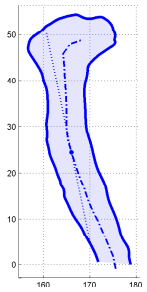

D2-L19742-305996-7

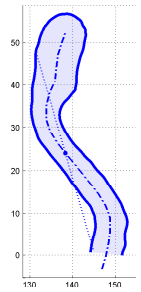

D2-L19743-306028-11

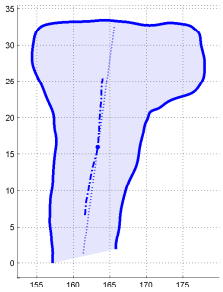

D2-L19743-306028-2

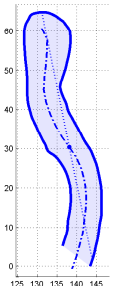

D2-L19743-306028-3

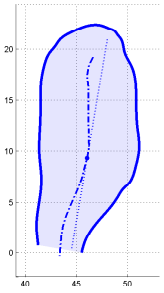

D2-L19743-306028-5

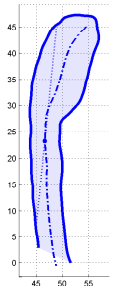

D2-L19743-306028-6

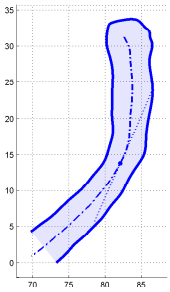

D2-L19743-306051-2

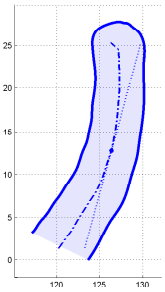

D2-L19751-306083-2

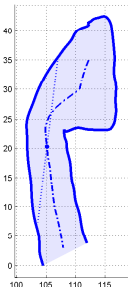

D2-L19766-306231-12

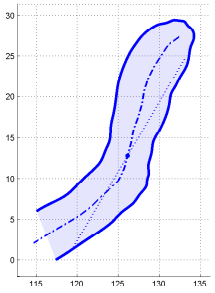

D2-L19766-306231-3

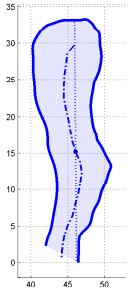

D2-L19766-306231-4

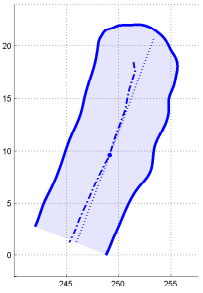

D2-L19766-306231-7

Figure 6.7: Profile lines estimated using the *Profilograph*. The medial axis is shown as dashed line. The major direction of the medial axis is shown as dotted line.

Sherd No.	$\overline{r_{Pr}}$ mm	h_{max} mm	d_r mm	d_{x_0} mm	$d_{x_0} < d_r$	$\overline{\alpha_P}$
D2-L19720-305925-12	58.99	37.06	8.91	1.19	$\surd$	-0.90°
D2-L19732-305940-5	131.86	67.31	11.93	4.44	$\surd$	-18.91°
D2-L19732-305940-6	150.16	31.77	14.91	9.36	$\surd$	-3.34°
D2-L19732-305940-7	197.59	30.80	28.61	27.19	$\surd$	10.58°
D2-L19732-305940-8	205.50	75.92	13.41	6.46	$\surd$	-14.98°
D2-L19736-306027-1	46.07	26.18	14.73	2.36	$\surd$	15.13°
D2-L19736-306146-6	44.76	27.51	9.49	17.62	$\times$	-4.90°
D2-L19739-305994-2	83.54	41.08	14.36	21.42	$\times$	19.71°
D2-L19739-305994-4	168.18	60.68	21.22	2.31	$\surd$	-11.75°
D2-L19742-305996-1	74.12	34.77	10.26	4.95	$\surd$	-13.44°
D2-L19742-305996-2	165.84	29.29	39.01	19.76	$\surd$	16.23°
D2-L19742-305996-3	147.52	48.92	9.83	22.65	$\times$	-21.94°
D2-L19742-305996-7	168.12	60.68	21.22	2.31	$\surd$	-11.75°
D2-L19743-306028-11	140.83	63.19	22.51	39.07	$\times$	-16.07°
D2-L19743-306028-2	162.83	37.90	31.83	9.75	$\surd$	7.79°
D2-L19743-306028-3	137.00	70.18	14.98	3.08	$\surd$	-11.45°
D2-L19743-306028-5	45.39	24.51	2.99	5.24	$\times$	9.62°
D2-L19743-306028-6	48.37	51.44	13.73	1.42	$\surd$	5.82°
D2-L19743-306051-2	79.92	35.88	3.12	3.21	$\times$	23.68°
D2-L19751-306083-2	125.31	31.21	24.05	31.17	$\times$	15.26°
D2-L19766-306231-12	107.26	46.46	13.13	2.30	$\surd$	7.02°
D2-L19766-306231-3	124.90	30.90	30.83	36.58	$\times$	30.51°
D2-L19766-306231-4	45.34	36.36	7.23	2.89	$\surd$	-0.45°
D2-L19766-306231-7	248.66	23.97	20.64	29.04	$\times$	20.75°
98-00 D1 260901	53.42	38.99	14.36	1.42	$\surd$	-7.33°

Table 6.2: Average radius $\overline{r}$ at the center of the medial axis with a major tilt angle α_M towards the rotational axis (equals y-axis), maximum height h_{max}, distances $d_r = r_{in} - r_{out}$, $d_{x_0} = d_{x_{0_{out}}} - d_{x_{0_{in}}}$ of the sherd of the profile lines acquired using the *Profilograph*.

As shown in Table 6.2 19 profile lines have a correct radius ($\surd$), while 9 profile lines have a wrong radius ($\times$) due to missplaced horizontal intersections with $d_{x_0} < d_r$.

6.4 3D-Scanner

The profile lines of the 3D-scanner have been estimated using the method proposed in Section 4 and Section 5. Figure 6.8a shows a top view with horizontal intersections for the final step of the estimation of the rotational axis similar to the *Profilograph*. Figure 6.8b shows multiple profile lines using multiple intersecting planes defined by the rotational axis and point along the circumference of the sherds. These profile lines are used to estimate the longest profile in case of sherds with complex fracture, where the point of maximum elongation parallel to the rotational axis would not result in the longest profile line. The grid-lines are spaced 50 mm. Figures 6.9 to 6.10 show the same information of the other sherds similar to Figure 6.8c. The grid-lines are spaced 10 mm. The horizontal profile lines and the multiple profile lines are shown in Appendix A

Table 6.3 at the end of this sections shows the estimated radius $\overline{r_{3D}}$, the maximum height h_{max} in mm. The angle α_{3D} of the main direction of the medial axis towards the rotational axis is shown in degree. All sherds could be acquired using the 3D-scanner, but the estimation of the axis of rotation failed for sherd "D2-L19766-306231-7", because it was too flat, as the circumference covered by this sherd was less than 5%.

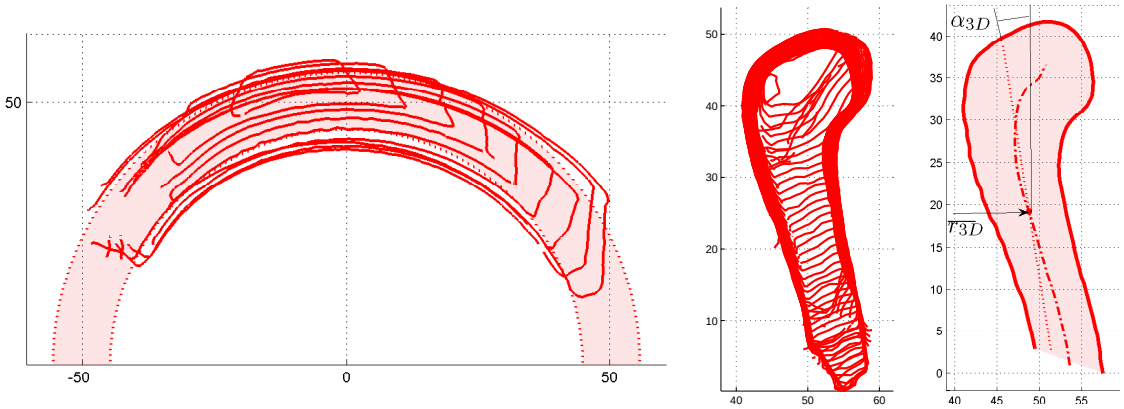

(a) (b) (c)

Figure 6.8: (a) Horizontal profiles and estimated circles based on the centers of gravity, (b) multiple profiles and (c) longest profile of the 3D-model of sherd "98-00 D1 260901".

The results for the horizontal intersection of sherd "D2-L19736-306146-8" and "D2-L19739-305994-4" shown in Figure A.2 have a distortion of the rotational axis. This distortion is a translation of the rotational axis is along the x-axis. The reason for this translation is a broken symmetry of these sherds, because they have been glued together (restored), which introduce a noticeable error, because the breakages are worn. Therefore we recommend to estimate the rotational axis based on sherds, that have not been restored.

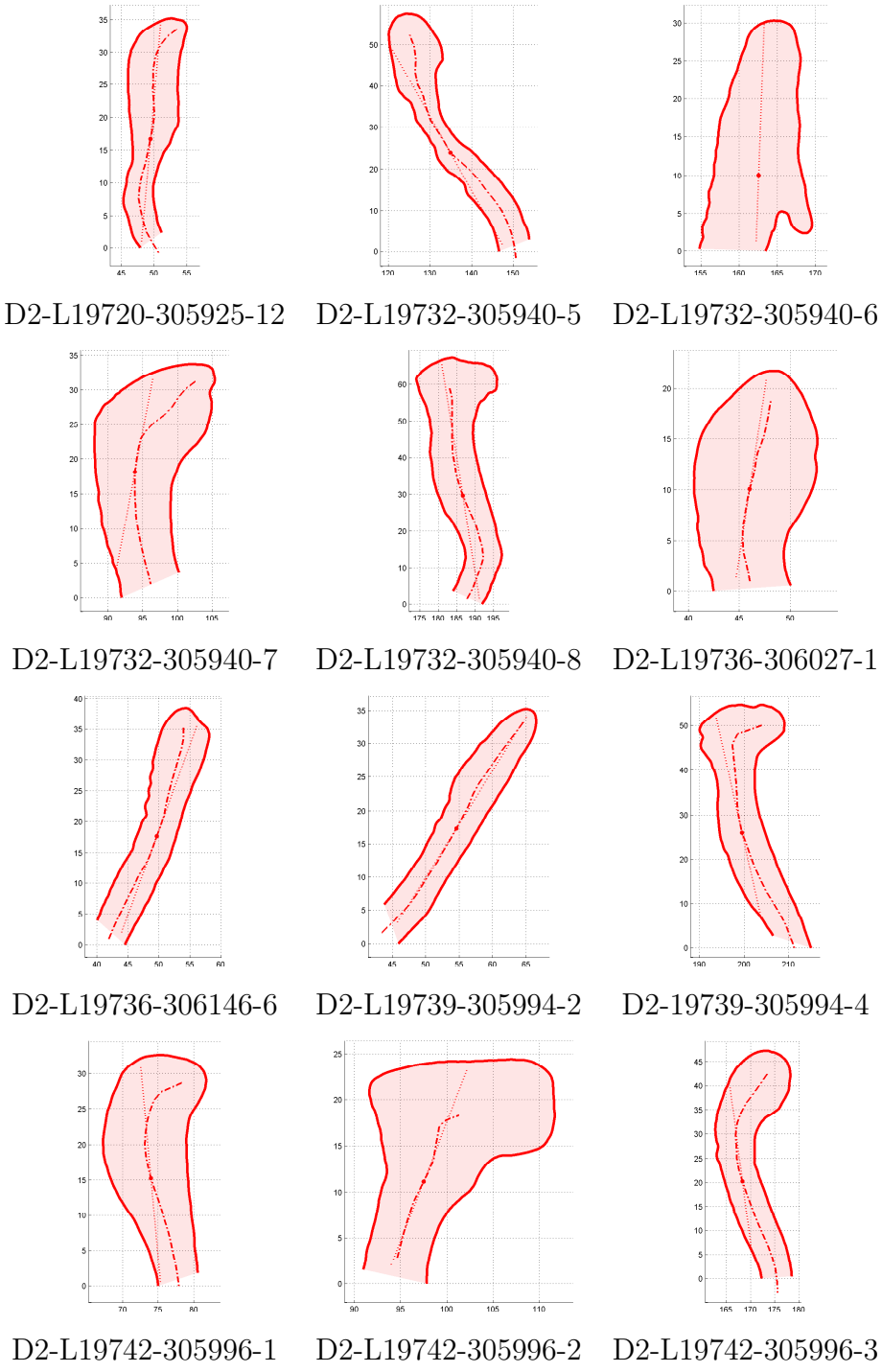

Figure 6.9: Profile lines estimated using the 3D-scanner. The medial axis is shown as dashed line. The major direction of the medial axis is shown as dotted line.

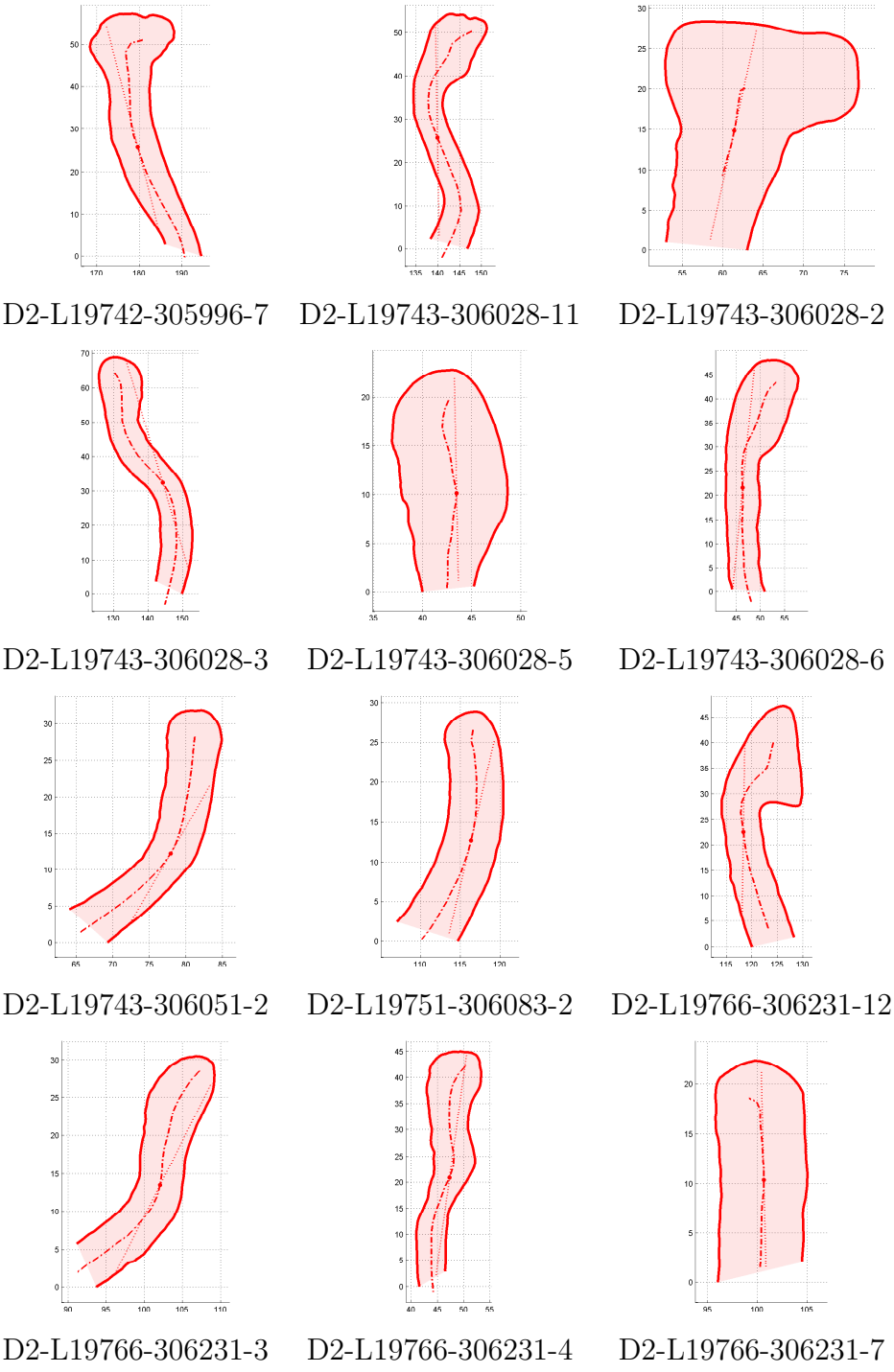

Figure 6.10: Profile lines estimated using the 3D-scanner. The medial axis is shown as dashed line. The major direction of the medial axis is shown as dotted line.

Sherd No.	$\overline{r_{3D}}$	h_{max}	$\overline{\alpha_{3D}}$
D2-L19720-305925-12	49.45 mm	38.04 mm	4.98°
D2-L19732-305940-5	137.48 mm	66.04 mm	-29.33°
D2-L19732-305940-6	162.80 mm	38.47 mm	2.10°
D2-L19732-305940-7	95.80 mm	39.80 mm	10.80°
D2-L19732-305940-8	187.25 mm	78.09 mm	-9.06°
D2-L19736-306027-1	46.50 mm	28.10 mm	8.65°
D2-L19736-306146-6	48.89 mm	42.86 mm	19.99°
D2-L19739-305994-2	54.54 mm	38.87 mm	31.98°
D2-L19739-305994-4	202.41 mm	64.03 mm	-12.62°
D2-L19742-305996-1	75.33 mm	37.27 mm	-5.21°
D2-L19742-305996-2	96.77 mm	30.47 mm	21.14°
D2-L19742-305996-3	170.89 mm	55.44 mm	-7.49°
D2-L19742-305996-7	182.04 mm	62.31 mm	-14.34°
D2-L19743-306028-11	141.77 mm	60.41 mm	-0.98°
D2-L19743-306028-2	61.13 mm	38.40 mm	12.40°
D2-L19743-306028-3	141.22 mm	76.10 mm	-16.58°
D2-L19743-306028-5	42.71 mm	28.67 mm	-1.10°
D2-L19743-306028-6	47.55 mm	52.77 mm	5.58°
D2-L19743-306051-2	75.64 mm	37.03 mm	29.92°
D2-L19751-306083-2	115.32 mm	33.51 mm	13.15°
D2-L19766-306231-12	120.52 mm	51.39 mm	0.89°
D2-L19766-306231-3	100.62 mm	32.86 mm	26.74°
D2-L19766-306231-4	45.94 mm	52.79 mm	7.84°
D2-L19766-306231-7	100.41 mm	29.39 mm	-1.36°
98-00 D1 260901	50.19 mm	49.57 mm	-8.94°

Table 6.3: Average radius $\overline{r}$ at the center of the medial axis with a major tilt angle α_M towards the rotational axis (equals y-axis), maximum height h_{max} of the sherd of the profile lines acquired using the 3D-scanner.

6.5 Comparison of Accuracy and Performance

As proposed in Section 6.1, we compare pairs of profile lines, where the profile lines are from the same sherd, but each profile line has been estimated by either the 3D-scanner or the *Profilograph* or the manual drawing. Therefore a comparison of the *Profilograph* in respect to the 3D-scanner is abbreviated as $P - 3D$. Comparisons with the manual drawing are abbreviated with an M.

The first step of the comparison is regarding the radial error. The radii $\overline{r}$ for the center of the medial axis is shown in Table 6.4. This table shows the radius $\overline{r_{3D}}$ for the profile line of the 3D-scanner and the absolute and relative distances $\Delta\overline{r}$ to the radius $\overline{r_P}$ of the *Profilograph* and the radius $\overline{r_M}$ of the manual drawing.

The second step was the comparison of the orientation of the profile lines. Table 6.5 shows the angle of rotation β between pairs of profiles. The angle β was estimated using the orientation of shapes by [Tho03]. Furthermore it shows the rotation of the main directions α of the skeletons of profile lines in respect to the orientated by [Tho03]. Regarding the main direction of the skeletons we can show that all pairs of profile lines orientated by [Tho03] have the same orientation with an average error of 3.0°, with a maximum of 13.3°. In comparison to the archaeological precision of ±5°, this is an acceptable result for 73 out of 75 pairs.

Finally Table 6.6 shows the average absolut distances Δp between the pairs of profile lines, which has a maximum of 3.75 mm even for the worst-case, where no axis of rotation could be found, because sherd "D2-L19766-306231-7" was too flat. The average of Δp is 1.22 mm. This result and the results of Table 6.6 show, that all profile lines have the same shape.

Figures 6.11a shows the pairs of profile lines with equal orifice plane for comparison. As the orifice plane is considered as plane orthogonal to the rotational axis and defined by the highest point of the profile, all these profile lines have been shifted parallel to the rotational axis (y-axis) to the same height. Furthermore this figure shows the medial axis (dashed line) and ist center (dot) and the main orientation (dotted line). The grid lines are spaced 10 mm. Therefore this figure corresponds to Table 6.4 and Table 6.5. Figures 6.11b shows the same pairs of profile lines as they have been translated, rotated and scaled by [Tho03]. Therefore this figure corresponds to Table 6.6. The Figures 6.13, Figures 6.14 and Figure 6.15 at the end of this Chapter show the same information like Figure 6.11 about the other 24 sherds. Figure 6.15 shows the four outliers, where either the radial error or the angular error is more then 40%.

Sherd No. D2-L...	$\overline{r_{3D}}$ mm	$\Delta\overline{r_{P-3D}}$ mm	$\Delta\overline{r_{M-3D}}$ mm	$\Delta\overline{r_{M-P}}$ mm	$\frac{\Delta\overline{r_{P-3D}}}{\overline{r_{3D}}}$	$\frac{\Delta\overline{r_{M-3D}}}{\overline{r_{3D}}}$	$\frac{\Delta\overline{r_{M-P}}}{\overline{r_{P}}}$
19720-305925-12	49.46	9.52	0.56	-8.95	-19.24%	-1.14%	-15.18%
19732-305940-5	134.90	-3.79	-16.47	-12.68	2.81%	12.21%	-9.67%
19732-305940-6	162.56	-12.40	-28.74	-16.34	7.63%	17.68%	-10.88%
19732-305940-7	93.86	102.12	54.16	-47.96	-108.80%	-57.70%	-24.47%
19732-305940-8	186.63	16.60	-21.23	-37.83	-8.90%	11.37%	-18.62%
19736-306027-1	46.03	-0.77	-3.48	-2.71	1.68%	7.57%	-5.98%
19736-306146-6	49.66	-5.93	24.19	30.12	11.94%	-48.71%	68.87%
19739-305994-2	54.58	28.64	9.76	-18.88	-52.47%	-17.88%	-22.69%
19739-305994-4	199.49	-33.34	-38.73	-5.39	16.71%	19.41%	-3.24%
19742-305996-1	73.98	-1.58	5.94	7.52	2.14%	-8.02%	10.38%
19742-305996-2	97.49	68.13	38.92	-29.21	-69.88%	-39.92%	-17.64%
19742-305996-3	168.33	-24.52	-18.24	6.29	14.57%	10.83%	4.37%
19742-305996-7	179.59	-13.43	-11.61	1.82	7.48%	6.47%	1.10%
19743-306028-11	139.89	-2.79	-24.25	-21.46	1.99%	17.34%	-15.65%
19743-306028-2	61.41	101.13	95.65	-5.48	-164.69%	-155.77%	-3.37%
19743-306028-3	144.29	-5.64	-1.78	3.85	3.91%	1.23%	2.78%
19743-306028-5	43.45	3.20	2.70	-0.49	-7.36%	-6.22%	-1.06%
19743-306028-6	46.33	0.36	5.21	4.85	-0.78%	-11.24%	10.38%
19743-306051-2	77.90	3.89	-1.45	-5.34	-4.99%	1.86%	-6.53%
19751-306083-2	116.36	10.17	-13.67	-23.84	-8.74%	11.75%	-18.84%
19766-306231-12	118.36	-12.93	-6.61	6.31	10.92%	5.59%	5.99%
19766-306231-3	102.07	24.24	-13.83	-38.07	-23.75%	13.55%	-30.14%
19766-306231-4	47.32	-1.37	2.29	3.66	2.90%	-4.83%	7.96%
19766-306231-7	100.65	149.81	51.32	-98.49	-148.84%	-50.99%	-39.32%
98-00 D1 260901	48.78	3.05	6.67	3.62	-6.25%	-13.66%	6.98%

Table 6.4: Average radius $\overline{r}$ at the center of the medial axis with a major tilt angle α_M towards the rotational axis (equals y-axis), maximum height h_{max} of the sherd of the profile lines acquired using the *Profilograph*.

Sherd No.	$\overline{\beta_{P-3D}}$	$\overline{\beta_{M-3D}}$	$\overline{\beta_{M-P}}$	$\Delta\overline{\alpha_{P-3D}}$	$\Delta\overline{\alpha_{M-3D}}$	$\Delta\overline{\alpha_{M-P}}$
D2-L19720-305925-12	-8.95°	6.25°	15.21°	-3.08°	0.23°	3.30°
D2-L19732-305940-5	11.79°	15.02°	3.23°	1.37°	0.13°	-1.24°
D2-L19732-305940-6	-8.84°	-7.37°	1.47°	-3.41°	-9.64°	-6.23°
D2-L19732-305940-7	1.81°	8.72°	6.90°	2.03°	3.98°	1.95°
D2-L19732-305940-8	-9.70°	-2.83°	6.87°	-3.78°	-1.46°	2.32°
D2-L19736-306027-1	-4.83°	-13.70°	-8.87°	-11.32°	-6.89°	4.43°
D2-L19736-306146-6	-30.90°	-6.43°	24.47°	-6.01°	-1.39°	4.62°
D2-L19739-305994-2	-16.36°	-15.52°	0.83°	-4.09°	-2.60°	1.49°
D2-L19739-305994-4	0.79°	1.51°	0.72°	-0.07°	-2.80°	-2.73°
D2-L19742-305996-1	-8.38°	0.68°	9.06°	-0.15°	5.76°	5.91°
D2-L19742-305996-2	-7.28°	-1.85°	5.43°	-2.36°	-1.30°	1.06°
D2-L19742-305996-3	-13.72°	-14.45°	-0.74°	0.73°	-0.42°	-1.15°
D2-L19742-305996-7	1.55°	2.40°	0.86°	-1.04°	-2.40°	-1.36°
D2-L19743-306028-11	-13.98°	-11.42°	2.55°	1.11°	1.75°	0.65°
D2-L19743-306028-2	-9.61°	-9.79°	-0.18°	-4.99°	-13.29°	-8.30°
D2-L19743-306028-3	6.77°	11.42°	4.65°	1.64°	-0.90°	-2.54°
D2-L19743-306028-5	13.00°	20.98°	7.98°	2.28°	-0.95°	-3.24°
D2-L19743-306028-6	0.54°	-7.80°	-8.34°	0.31°	-3.33°	-3.64°
D2-L19743-306051-2	-4.74°	-13.25°	-8.50°	1.50°	1.07°	-0.43°
D2-L19751-306083-2	4.49°	22.08°	17.59°	2.38°	5.84°	3.46°
D2-L19766-306231-12	5.16°	-1.94°	-7.10°	-0.97°	-2.38°	-1.40°
D2-L19766-306231-3	3.55°	7.04°	3.49°	-0.22°	-2.11°	-1.89°
D2-L19766-306231-4	-2.27°	3.92°	6.19°	6.02°	2.23°	-3.79°
D2-L19766-306231-7	25.96°	59.70°	33.74°	3.85°	0.79°	-3.06°
98-00 D1 260901	-5.76°	-7.58°	-1.82°	-7.38°	-7.90°	-0.52°

Table 6.5: Average radius $\overline{r}$ at the center of the medial axis with a major tilt angle α_M towards the rotational axis (equals y-axis), maximum height h_{max} of the sherd of the profile lines acquired using the *Profilograph*.

Furthermore Figure 6.12 shows perfectly overlaid pairs of profile lines estimated at a precisely marked point on sherd "98-00 D1 260901". Figure 6.12d shows that this manual drawing has a different height and the curvature on the rim differs from the *Profilograph* (Figure 6.12b) and the 3D-scanner (Figure 6.12c). At the inner side the curvature changes the sign, which can influence an automated classification based on the curvature of the profile line.

Figure 6.12b shows that due to high quantization error there may be non-existing edges introduced (at the rim). Such edges are detected as characteristic points and can lead to wrong classification. The quantization for this profile is 50 points for the profile line acquired with the *Profilograph*. The profile line estimated using the 3D-modelhas 572 points. As this profile line has an arc-length of 113.7 *mm* the *Profilograph* has an

Sherd No.	Δp_{P-3D} mm	Δp_{M-3D} mm	Δp_{M-P} mm
D2-L19720-305925-12	0.93	0.67	1.35
D2-L19732-305940-5	1.93	2.47	1.13
D2-L19732-305940-6	0.90	1.02	1.08
D2-L19732-305940-7	0.92	0.90	0.95
D2-L19732-305940-8	1.81	0.60	1.38
D2-L19736-306027-1	0.80	1.34	0.86
D2-L19736-306146-6	3.16	1.65	2.17
D2-L19739-305994-2	2.03	1.81	0.41
D2-L19739-305994-4	0.57	0.75	0.43
D2-L19742-305996-1	0.79	0.40	0.97
D2-L19742-305996-2	0.64	0.60	0.83
D2-L19742-305996-3	1.70	2.00	0.69
D2-L19742-305996-7	0.71	0.72	0.55
D2-L19743-306028-11	1.98	1.64	1.01
D2-L19743-306028-2	1.26	1.20	0.39
D2-L19743-306028-3	1.52	2.07	1.07
D2-L19743-306028-5	0.93	1.47	0.64
D2-L19743-306028-6	0.68	1.51	1.96
D2-L19743-306051-2	0.56	1.13	0.85
D2-L19751-306083-2	0.44	1.91	1.52
D2-L19766-306231-12	1.11	0.62	1.08
D2-L19766-306231-3	0.31	0.84	0.69
D2-L19766-306231-4	2.10	0.68	2.04
D2-L19766-306231-7	1.76	3.75	2.14
98-00 D1 260901	1.76	1.48	1.05

Table 6.6: Average radius $\overline{r}$ at the center of the medial axis with a major tilt angle α_M towards the rotational axis (equals y-axis), maximum height h_{max} of the sherd of the profile lines acquired using the *Profilograph*.

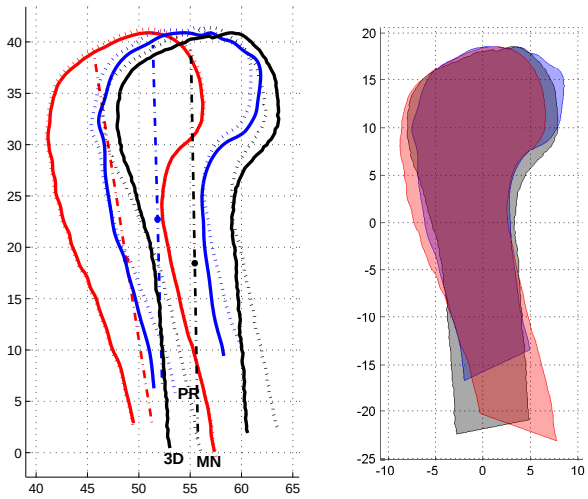

(a) (b)

Figure 6.11: Longest Profile Lines of sherd "98-00 D1 260901" translated along the rotational axis to have an equal orifice plane ($h = 50.7\ mm$). (a) From left to right the 3D-scanner ($3D$), the *Profilograph* (Pr) and the manual drawing (Mn). (b) Overlay of the translated, rotated and scaled profile lines by [Tho03].

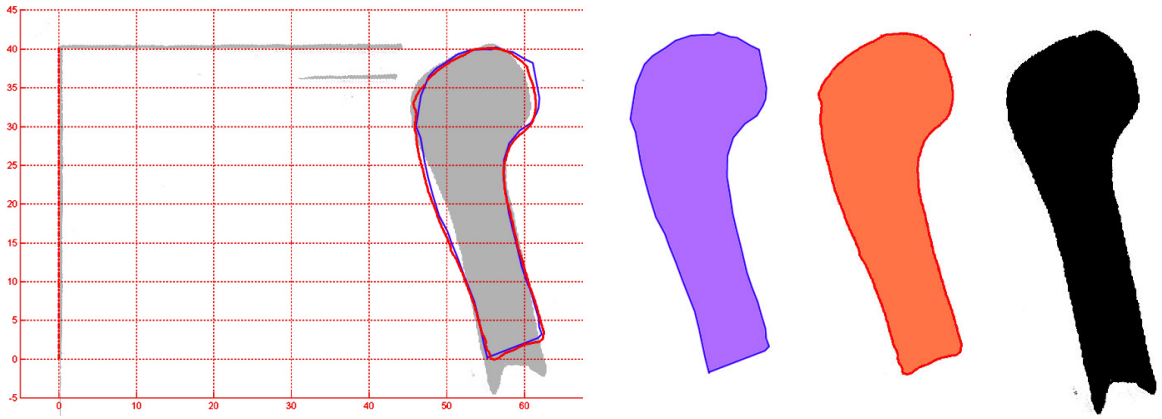

(a) (b) (c) (d)

Figure 6.12: (a) Profile Lines of sherd "98-00 D1 260901" extracted at the same point of the sherd in respect to the rotational axis (equals y-axis), acquired by (b) the *Profilograph*, (c) the 3D-scanner and (d) the manual drawing.

average resolution of 2.2 mm and the 3D-scannerof 0.2 mm. The resolution of the manual drawing can be approximated in between with 1.0 mm, because a 1 mm scale paper was used.

For the acquisition of the 25 sherds, we measured the time required for acquisition and processing for the 3D-scanner and the *Profilograph*. The time for drawing a profile line manually was measured to compare the three system regarding performance. Furthermore we measured the time for acquisition and processing of additional sherds in-situ and in the laboratory (e.g. well-known vessel from Section 4). These additional measurments had the same result. Table 6.7 shows the average time for documentation and the estimated time in working days (8 hours per day) for acquiring a typical archaeological documentation showing 15.000 sherds. The average time measured using the 3D-scanner is based on further 500 sherds which have been acquired, with and without the frame. For future improvement we measured the times for entering data (e.g. sherd number), data transfer and handling the 3D-scanner. Table 6.7 shows the proposed time.

	Sherds per hour	Working days
Manual Drawing	4–5	375
Profilograph	5–6	312
3D-scanner	15–20	94
... with frame	35–40	47
... with future improvements	60–100	24

Table 6.7: Average time for documentation of fragments using the 3D-scanner, the *Profilograph* and manual drawings. Estimation of working days for a typical archaeological documentation having 15.000 sherds.

6.6 Summary

Comparing the results regarding radial and angular errors to determine which method is best, is difficult because it depends on how the threshold for acceptable errors are set and how these errors are weighted. In particular this decision gets even more difficult for smaller sherds like shown in Figure 6.15. For example for sherd "D2-L19766-306231-7" the estimation of the axis of rotation fails. This might appear as disappointing, but it is honest because it is more objective than setting an arbitrary axis of rotation. This example also supports our paradigm, that our method should assist archaeologists and shall not replace them.

Comparing all results especially regarding accuracy, performance and possibilities for further use, we can conclude that the 3D-scanner using our methods is the best choice, when it is used with a minimal archaeological supervision, because of several reasons, which are shown below. The minimal archaeological supervision means nothing more than using 'a second set of eyes', which checks the plausibility of automatically estimated profile lines in respect to the archaeological context. As this has do be done also for manual drawings or the *Profilograph*, no extra working-time is required.

- 3D-acquisition and its processing is today at least four times faster than a manual drawing and the *Profilograph*.
- It is robust against unintentionally tampering of profile lines like the scaling problems of the manual drawings or introduction of characteristic points due to misplaced measurements using the *Profilograph*.
- 3D-scanners can be operated with only a few hours of training and without expert knowledge.
- Having a complete representation of sherds or vessels as 3D-model opens new possibilities for further archaeological research, because they are accessible in contrast to real sherds, which are virtually inaccessible locked away into their storage.

The only (today's) drawback of the 3D-scanner are the initial cost, which have to be counterbalanced by the savings regarding cost for working hours. This can be achieved by a continuous use for approximately two to three years.

The next Chapter shows one new possibility for an archaeological application using 3D-acquisition.

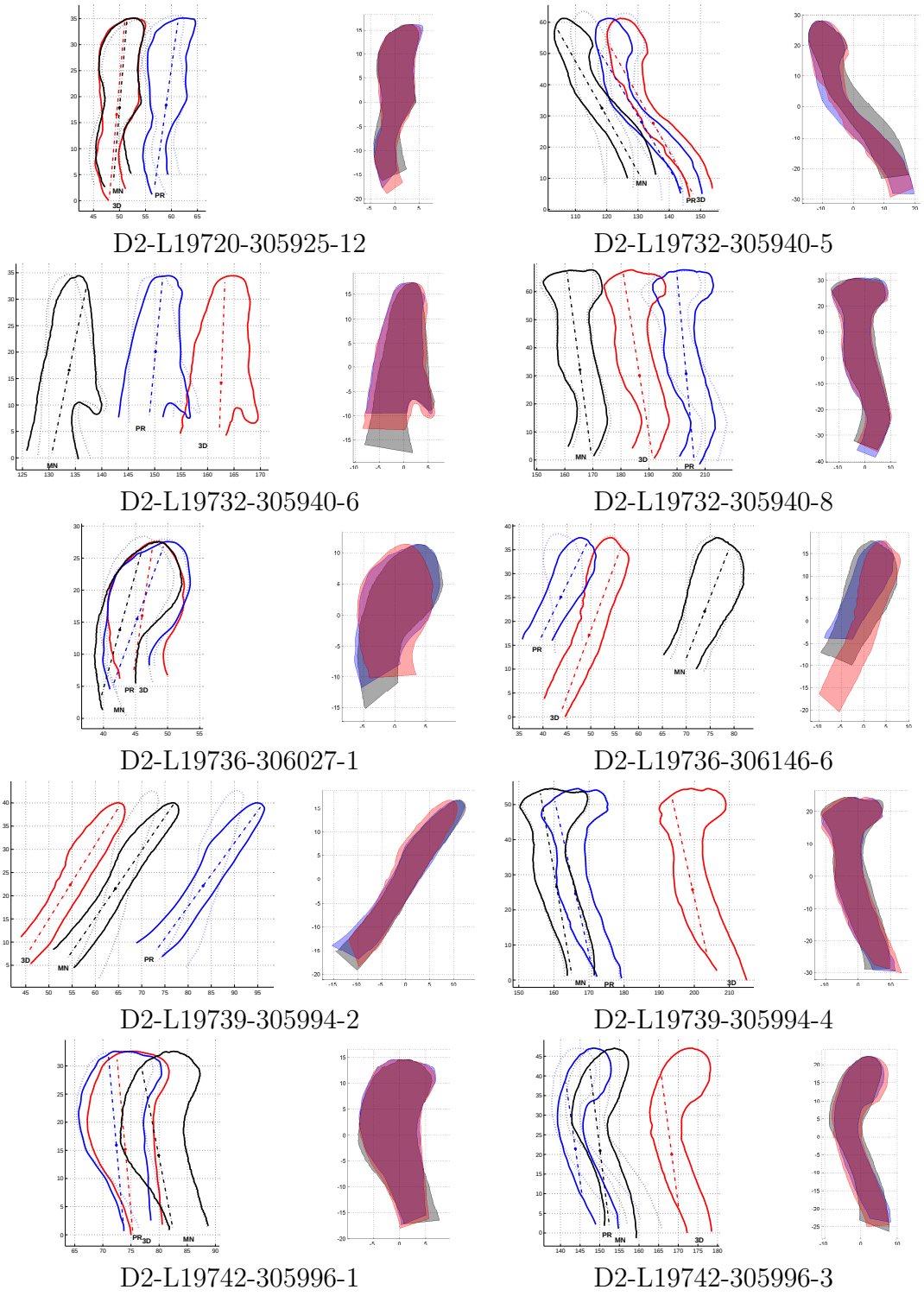

D2-L19720-305925-12 D2-L19732-305940-5

D2-L19732-305940-6 D2-L19732-305940-8

D2-L19736-306027-1 D2-L19736-306146-6

D2-L19739-305994-2 D2-L19739-305994-4

D2-L19742-305996-1 D2-L19742-305996-3

Figure 6.13: Comparison of profile lines.

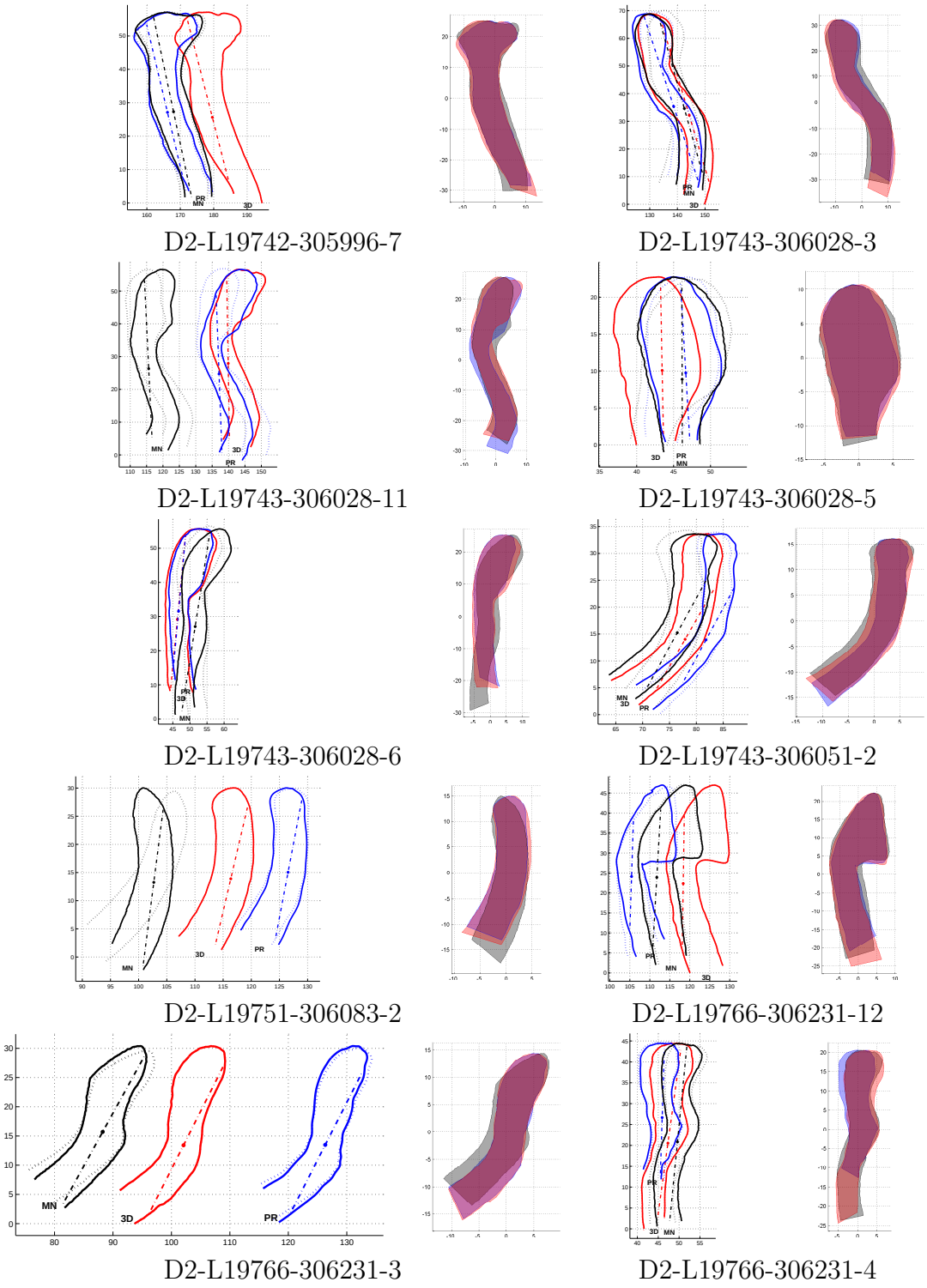

Figure 6.14: Comparison of profile lines.

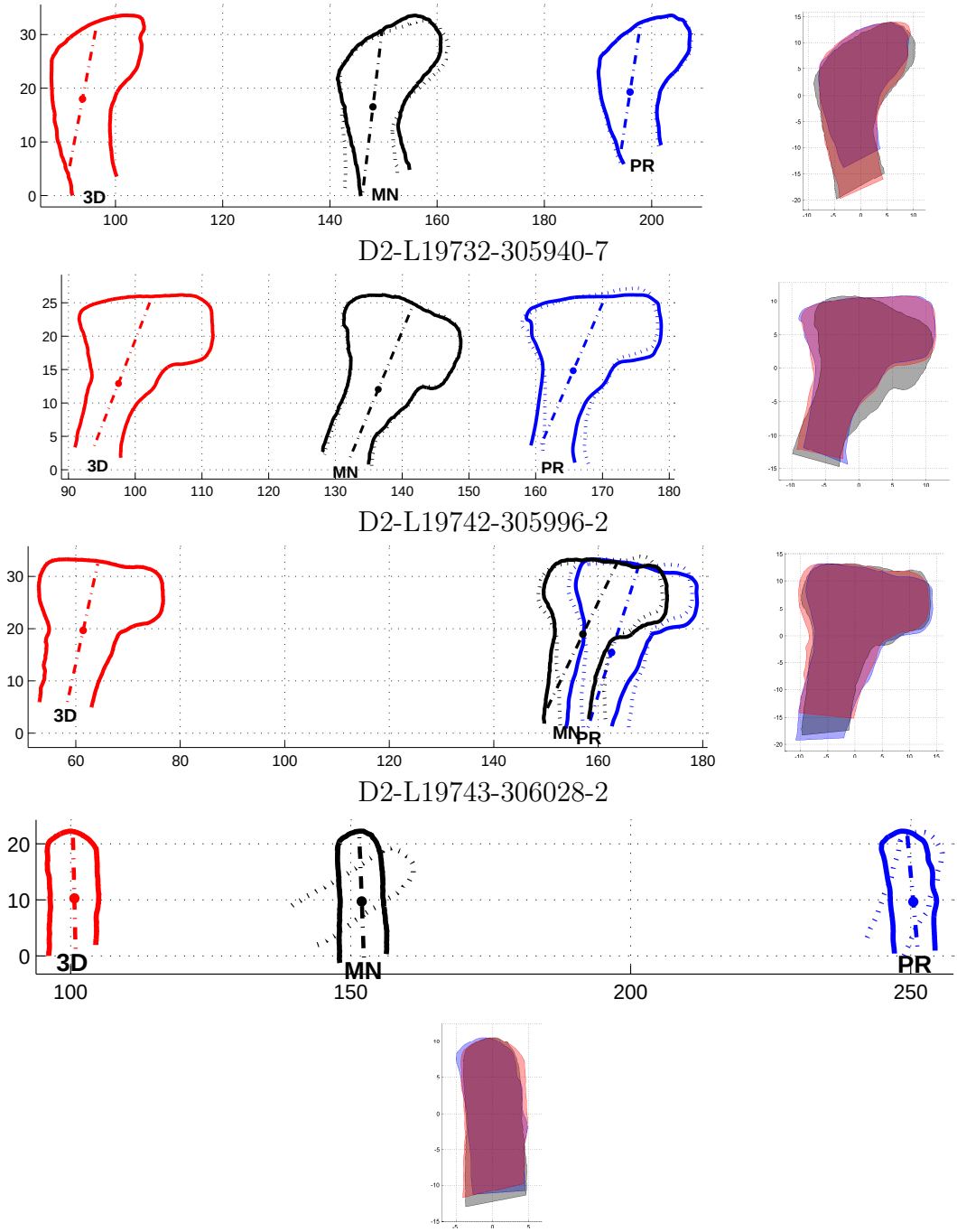

Figure 6.15: Comparison of profile lines.

Chapter 7

Processing of Vessels

This chapter shows a method to answer archaeological questions about the manufacturing process of ancient ceramics, which is important to determine the technological advancement of ancient culture. The method is based on the estimation of the profile lines of sherds described in previous chapters, which can also be applied to complete vessels. With the enhancements shown in this chapter, archaeologists get a tool to determine ancient manufacturing techniques.

Four this method we use complete vessels, because sherds of excavations of living places have been dumped and re-used as filling material for floors and walls. Therefore sherds virtually never reassemble a complete vessels and therefore no real ground truth is known. As archaeologists are also excavating burial places, where individual unbroken ceramics or complete sets of sherds are found, our method can be applied on, but is not limited to, individual vessels.

7.1 Analysis regarding the Manufacturing Process

Conclusions about the manufacturing process can reveal important information for archaeologists, because the manufacturing technology give information about development of an ancient culture, For example archaeologists determine between ceramics, that have been produced on slow or fast turning rotational plates. Another example would be an ongoing discussion between archaeologists about the existence of rotational plates for manufacturing ceramics in South America. The general opinion is that in this region the wheel was not invented and there fore ceramics were produced with a rotational plate (wheel) [WT02] on the other hand-side there is evidence that rotational plates were used [Car86].

As we use structured light as 3D-acquisition method, we can not make an assumption about the internal structure of a ceramic like [WT02], but we can estimate the surface with high resolution (0.1 mm). Therefore we can analyze the symmetry and estimate features like deviation of real surfaces in respect to a perfectly symmetrical surface. Such features can help archaeologists to decide about the technological advancements of ancient cultures.

To begin with our investigation in answering questions about the manufacturing process of ceramics, we choose to use two modern pots, which were manufactured in traditional way. Therefore this data can be interpreted as mixture between synthetic and real data, because we used real objects, but in contrast to real archaeological fragments, we know how it was produced.

Furthermore we decided to use the method for finding the orientation of a sherd [MK03]. We start with the profile line, which can be estimated in a similar way like for sherds. The difference is, that for complete vessels the bottom plane can be used for orientation, because it is the counterpart for the rotational plate, which defines the (orthogonal) axis of rotation.

We estimate multiple profile lines, which can be overlaid by transforming them into the same coordinate system, where the y-axis equals the rotational axis. Therefore the distance between profile lines can be estimated. Figure 7.1 shows a front and side-view of our pots. The third column it shows the longest profile line and the fourth column shows multiple profile lines combined with the side-view, like archaeologists show such vessels in their documentation. In case of the multiple profile lines, we have estimated, that the distance between the profile lines differs and therefore these pots and their profile lines are unique. The maximum distance between two profile lines of the first pot was 9.8 mm and 21.2 mm for the second pot.

7.2 Experiments

The multiple profile lines shown Figure 7.1d,h. The radii (x-axis) between their profile lines at the same height (y-axis) are not equal. If the profile lines were parallel, this would mean, that the pots have an elliptic (horizontal) cross-section. As it appears, the asymmetry is more complex. Therefore, we choose to analyize the pots slice-by-slice along the rotational axis supposed as orthogonal to the bottom plane.

Figure 7.2a,c shows the horizontal intersection, we applied with a distance of 10 mm along the rotational axis. The distance of 10 mm corresponds to the manufacturing process, which has left its traces as rills as seen in Figure 7.1a,b,e,f. These rills are spaced 10 mm, which corresponds to the width of finger or tool used to "grow" the pot along the axis of the rotational plate. The intersections at height 160 mm and 170 mm have been discarded, because they intersect the "shoulder" of the pot with a very low angle ($<< 5°$), resulting in an intersection having a non-representative, random curvature.

Dividing ceramics into section by characteristic points (like the "shoulder") is done by archaeologists for classification. Therefore we choose to analyze the segmented object into a lower and an upper part. This means, we have two fragments, where an axis estimation can be applied, like for sherds (fragments). The estimation of the axis is shown in Figure 7.2b,d. The numeric results for the axis are, that they have a minimum distance

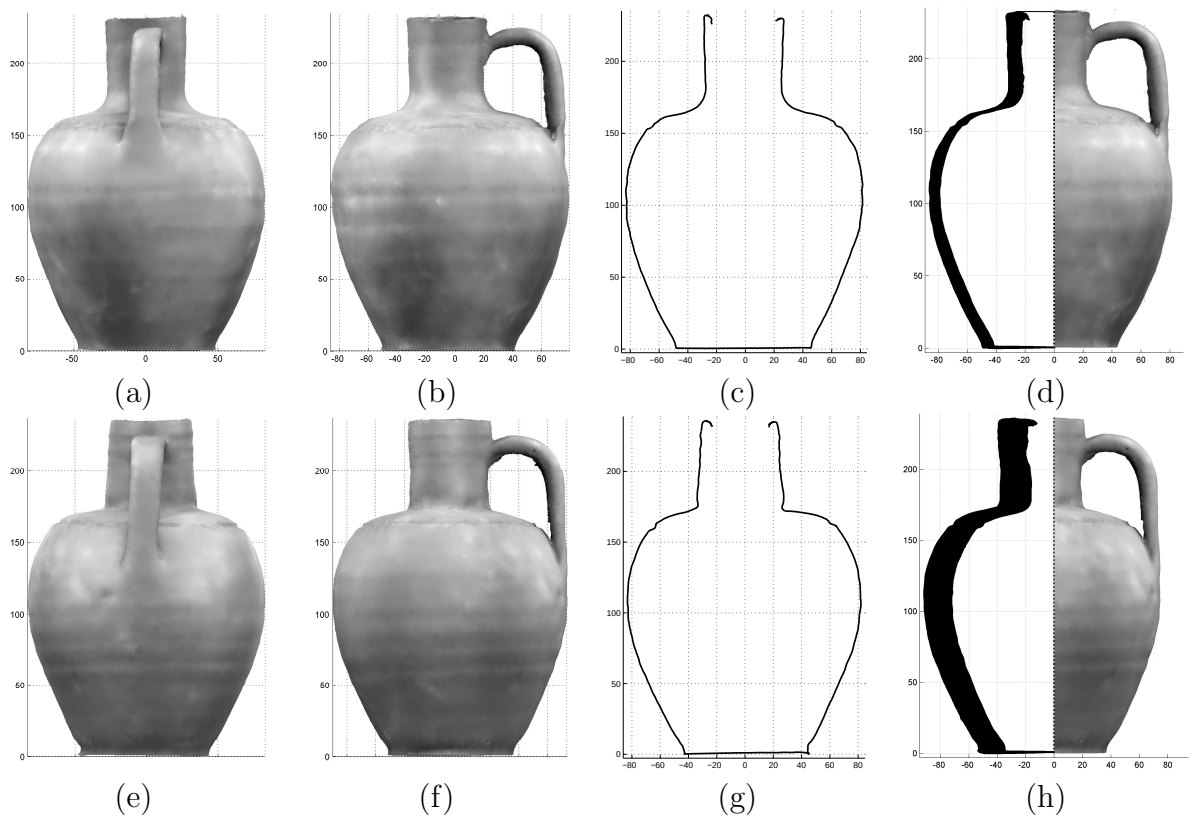

Figure 7.1: (a,e) Front-view, (b,f) side-view, (c,g) longest profile line and (d,h) multiple profile lines of modern ceramics, manufactured in traditional way, which are supposed to be identical.

of 4 mm towards each other and to the axis defined by the bottom plane. Furthermore the angles between the axes differ for 5° to 7°.

Using the rotational axis of the lower and upper fragment, we repeated the estimation of the profile lines, which are shown in Figure 7.3 for the upper part and lower part of the objects. The maximum distance between the profile line is 7 mm for the upper and 2 mm for the lower part. Therefore the first conclusion is, that the upper and lower part do have different axis of rotation, which means, that these parts have been produced separately and combined without the use of the rotational plate.

7.3 Results

We can conclude, based on the different deviation to the multiple profile lines shown in Figures7.3a,e of the upper parts, that the upper part has been made in a lesser quality than the lower part, which has been made by potters with different experience and/or on a slower rotational plate. Vice versa the deviation of the upper part of up to 7 mm compared to less than 2 mm of the lower part, shows that a faster turning rotational plate

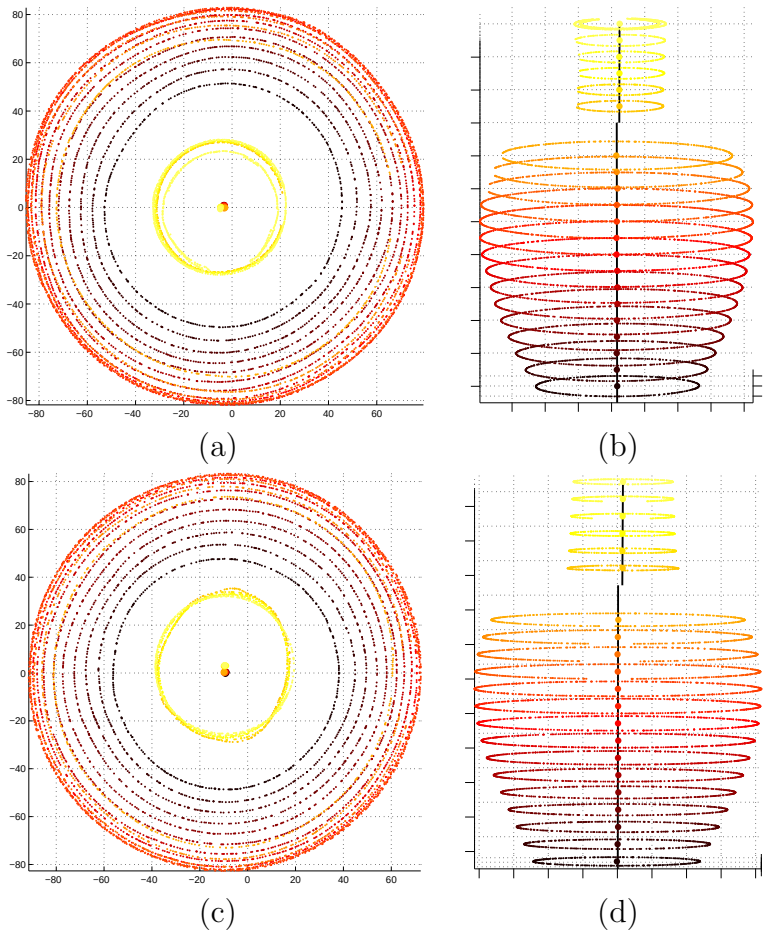

Figure 7.2: (a,c) Top-view and (b,d) side-view of the horizontal cross-sections - the level of gray corresponds to the height. The axis of rotation for the lower and upper part is shown as black line, defined by the centers of the concentric circles (shown as dots).

has been used and for the upper part more experience is required.

From the differing angle between the axis of rotation based on the bottom plane compared to the axis of rotation of the upper and lower fragment, we can conclude that the either the bottom has been post-worked or the pot has been contorted before it was fired in the oven.

Even with the corrected axis for the parts of the object, the horizontal intersections are not perfectly circular. The horizontal intersections are elliptic. Therefore we estimated the direction of the major and minor axis of the ellipses. Therefore we could estimate that the minor axis has the same direction as the orientation of the handle. This means that the symmetry of the pots was broken, when the handle was attached, while the pots were still wet. Figure 7.4 shows the pots, intersected by a plane, defined by the center of gravity of the pot and the direction of the major axis of the ellipses. The angle between the minor axis and the handle of the pot was 7° and 14° for the second pot.

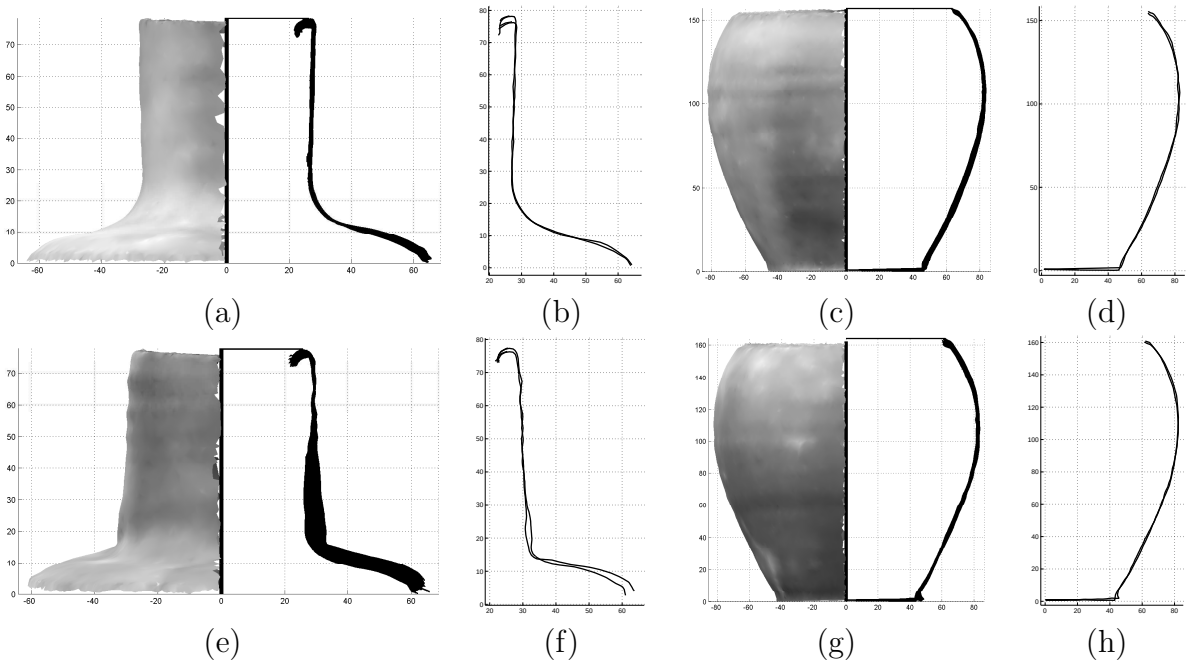

Figure 7.3: Axis of rotation and multiple profile lines of the upper part (a,e) and lower part (c,g), and (b,d,f,h) the longest profile lines of the parts of the objects.

Figure 7.4: Planes of symmetry of the (a) first and (b) second object.

We additionally conclude that ellipses fitted [GGS94] to the horizontal cross-sections can be used as a further feature. Therefore the distance between the foci of the ellipse is estimated. Ceramics with a distance converging towards zero (circular cross-sections) are made of higher quality.

7.4 Summary

The proposed method regarding the analysis of the manufacturing process is part of an enhanced archaeological documentation system, which will replace the traditional documentation system of manual drawings by a fully computerized system, which can be used beyond the estimation of profile lines of sherds. This system can document sherds with increased accuracy and makes it possible to investigate other archaeological questions. Such questions concern the quality of production of ceramics, which are reflected by its symmetry or information about the manufacturing process can be revealed. The next chapter concludes this thesis and gives an outlook for future work.

Chapter 8

Conclusion and Outlook

The work presented in this thesis proposes a method for estimation of the axis of rotationally, symmteric objects. The main application has been the documentation of archaeological finds, which are fragments of ceramics (sherds) manufactured on rotational plates. The acquisition has been done by 3D shape estimation, using structured light. The orientation, which has been done by estimation of the rotational axis of the sherds, is the important step in documentation of ancient ceramics. Documentation of sherds is an important task in archaeology, because they belong to the majority of finds on excavations and therefore their documentation is essential for retrieval of information about history, which are, but not limited to, the size of a populations, technological advancements, trading relations and cultural influence by traveling people.

Therefore the main part of this work has been the algorithm for estimation of the rotational axis. Because of the difficulty having generally no ground truth about fragments of ceramics, we have implemented an automated method inspired by the well-proven and well-known manual method used by archaeologists. Archaeologists document their finds by drawing a profile line, which is used to determine the class of the object it belongs to. The profile line is a horizontal cross-section of the finds. As the word "horizontal" proposes, the orientation of the finds is the essential part of the documentation. This is achieved by archaeologists by template matching of concentric circles. Therefore we used the same principle for the estimation of the rotational axis. In the first step sets of parallel circle templates were matched vertically against the balancing plane of the sherd. The result was the plane of symmetry, which contains the rotational axis. In the second step the sets of circle templates were matched using the plane of symmetry. For perfect objects the result would be the rotational axis, but in respect to real objects a third refinement step has been applied. In the refinement step variations of the rotational axis of the previous step were used for circle matching. The best fitting set of circle templates were used to fit the rotational axis using the (concentric) centers of the circle. This method has been tested with synthetic objects and real well-known sherds. Furthermore, the results of the well-known sherds using the manual (inspiring) method, have been compared with the results of the proposed method.

The second part has described the tasks which have to be perfomerd to use the axis estimation for practical application at archaeological excavations. These tasks were the removal of noise and objects holding the sherds in front of the 3D-scanner. Furthermore we had to determine distortions of the symmetry, which are decorations and the fractured parts of a sherd. As sherds are generally decorated only on the outside, we decided to use the inner side for estimation of the rotational axis. To find the inner side and to discard the fracture and other possible distortions of the symmetry we estimate the curvature along the surface using geodesic patches. Then the rotational axis is estimated using the inner rotationally, symmetric side of the sherd. Afterwards the profile line is estimated. Experiments with synthetic objects have been shown, before the method was tested on real objects.

Experiments with real objects have been described in the third part of this thesis. In this part we experimented with small sherds, where an estimation of the rotational axis is difficult. Furthermore profile lines of these sherds were also drawn manualy and using the *Profilograph*. All pairs of profile lines estimated from 25 selected sherds have been compared. The result was that all profile lines have the same shape, but have differences in postion (radii) and orientation (angle). Because the shape is equal and these differences are no major errors, we could conclude that either way of estimating profile lines has its drawbacks. Under respect to accuracy and performance our method using 3D-acquisition has a winning margin.

Beside this winning margin, we finally have shown a method using 3D-models to determine ancient manufacturing techniques. This method can be used even for rare unbroken vessles or sets of sherds reassembling a complete vessel. This additional functionality, like the analysis of the manufactuing process, will lead to an enhanced archaeological documentation system, which will replace the traditional documentation system of manual drawings by a fully computerized system. This system can document sherds in a fraction of time and with increased precision. Therefore archaeologists can save working time for other important archaeological tasks, e.g. the interpretation of finds. Furthermore our system will also be able to assist archaeologists in documentation and comparison of painted sherds, which require even more manual working time. Additionally the use of databases for storage of profile lines will assist archaeologists comparing the tens of thousands of sherds found on excavations.

During our continuous cooperate work with archaeologists we have shown that archaeological documentation of ceramics can be done by the use of 3D-scanners. Beside the main concern of archaeologists regarding accuracy they are also concerned about performance. Therefore we are not only introducing new algorithms and improving our existing algorithms, but we always measure the time for handling the different steps of the documentation system. These steps begin when an artifact is found, and end, when it is put to storage. Therefore we also measure the time for each sub-step, which are for example:

- Assigning a unique number to an artifact.
- Cleaning
- Positioning of the artifact for 3D-scanning.
- Entering information about an artifact into a database.
- Final storage of the artifact into an archive.

Regarding our practical experiments, we can propose a speedup of a factor of three or more for documentation of sherds by improving the user-interface and by automation of the numbering systems. For example, the use of bar-codes or printed numbers instead of manually assigned and painted numbers will increase performance and robustness of the system. Such techniques have to be field-tested in long-term experiments, because the numbering system has to be robust against aging issues (e.g. fading of bar-codes). Future improvements other than performance related will be:

- Puzzle solving: as sherds sometimes belong to the same vessel, a matching of fractures of the surface will lead to a longer profile line and therefore to a complete reconstruction of a vessel. Such complete reconstruction can be achieved if fragments from the bottom up to the rim are present. If there are no matching fragments an alignment of sherds like pearls on a string can be used to estimate a profile line of the complete vessel.
- High-resolution texture. As current 3D-Scanners use high-speed CCDs with a low resolution for acquisition of fragments in less than a minute, the texture acquired lacks resolution. The resolution of the state-of-the-art 3D-scanner used for our experiments has a resolution of 640×480 pixels and uses a color-wheel for retrieval of color images. Therefore the integration of digital camera with higher resolution and better quality of color is proposed.
- Multi-spectral texture-map: The consequential improvement of the previous step would be the integration of an infrared camera and a camera acquiring ultra-violet images. This will open new possibilities for analyzing the paint used for ceramics and can help restore faded colors similar to applications on medieval paintings in art history.

As we have shown our system assists and increases the speed of archaeological documentation of excavations. The improvements listed above will extend the use for archaeology and it will be of interest for other user-groups working in the field of restoration and conservation, which are mostly museums, and for archaeological research regarding interpretation of finds.

Acknowledgements

Hereby I wish to thank all institutions, projects and archaeological partners for funding my work and for providing hardware, real data and expert knowledge:

- The FWF (*Fonds zur Förderung der wissenschaftlichen Forschung*) project *Computer Aided Classification of Ceramics* under grant P13385-INF for financial funding of my work and the travel expenses to international conferences. Kristina Adler und Martin Penz for archaeological supervision and for providing the classification scheme for late roman pottery.
- The *Innovative Project 3D Technologies* of the Vienna University of Technology for providing the 3D-scanner.
- The Bikura Project and Uzy Smilansky for partial travel funding of the field trip to *Tel Dor* in Israel.
- Israel Antiquties Authority (IRAA) and the exploration society of the *Tel Dor* excavation under supervision of Ilan Sharon for granting permission for publication of the sherds acquired in *Tel Dor*. Vered Rozen for manually drawing the profile lines of the sherds found in *Tel Dor*. Igor Mintz for operating the *Profilograph*.
- Horst Wildenauer (Vienna University of Technology, PRIP Group) for usefull comments about the geodesic neighbourhood.
- Elisabeth Trinkl (*Institut für Kulturgeschichte der Antike, "Østerreichische Akademie der Wissenschaften*) for manually drawing the profile lines of the well-known object.
- Willi Kaiser for proofreading the manuscript of this thesis.

Appendix A

Profile Lines

This appendix shows profile lines of sherds acquired during the field-trip to *Tel Dor* acquired by using the 3D-scanner and the *Profilograph*.

A.1 3D-Scanner

This section shows the profile lines estimated using the estimation of the rotaional axis proposed in this thesis using real 3D-models. The first and second column of each Figure shows the horizontal intersections used for the final step of the axis estimation. The third and fourth column shows the multiple profile lines for validation of the axis estimation and for estimation of the longest profile line. The grid lines are spaced 50 *mm* for the first and third column. The grid lines are space 10 *mm* for the second and third column.

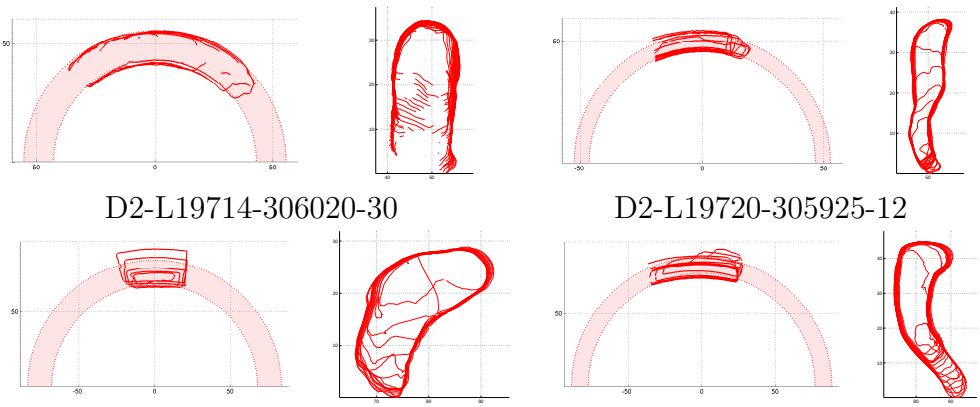

D2-L19714-306020-30 D2-L19720-305925-12

D2-L19720-305925-1 D2-L19732-305940-11

Figure A.1: Horizontal intersections and profile lines.

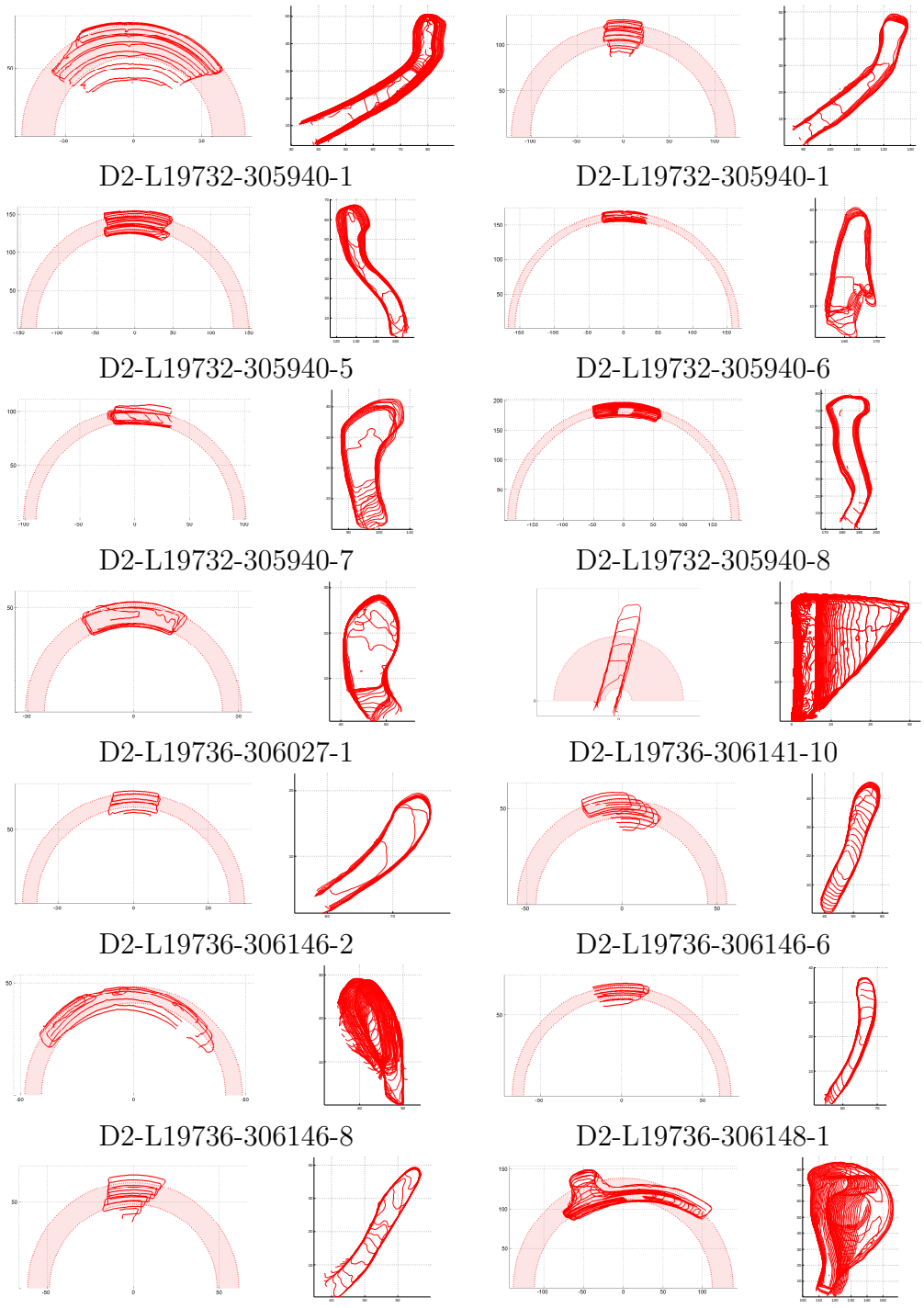

Figure A.2: Horizontal intersections and profile lines.

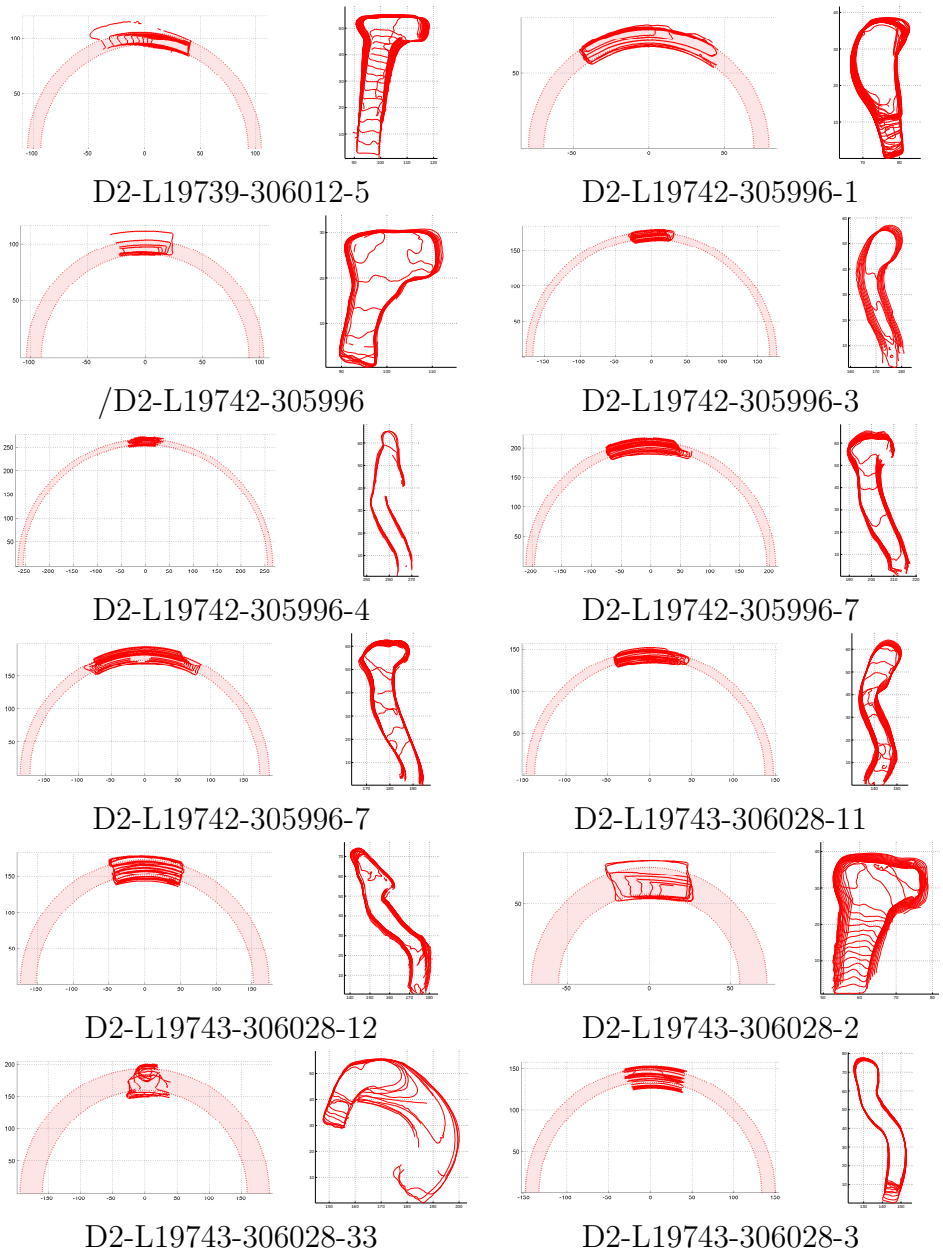

Figure A.3: Horizontal intersections and profile lines.

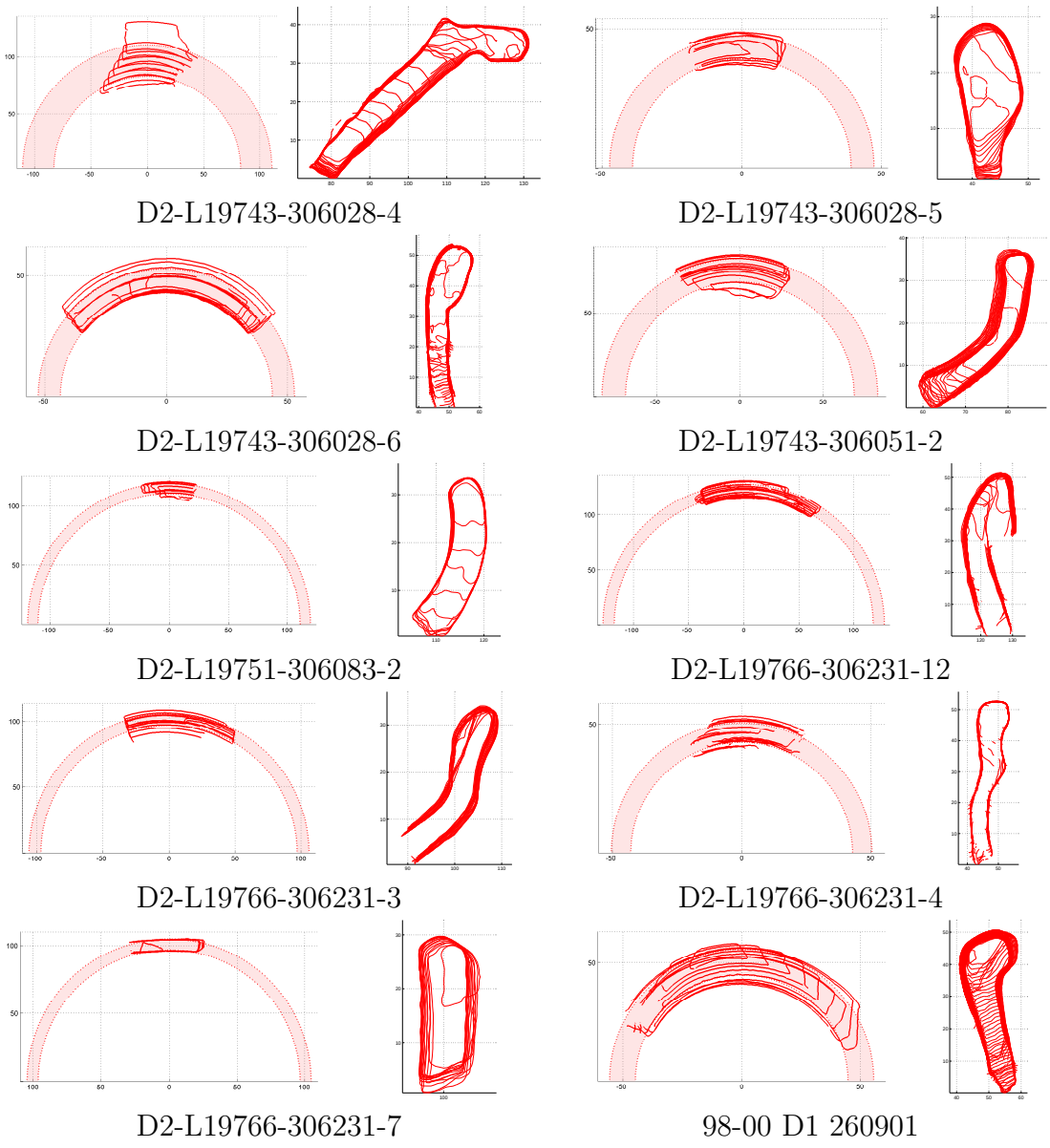

Figure A.4: Horizontal intersections and profile lines.

A.2 *Profilograph*

This section shows the profile lines estimated using the *Profilograph*. The first and second column of each Figure shows the horizontal intersections used for estimation of the rotaional axis. The third and fourth column shows the profile line showing the radii on th x-axis, which have been set using the horizontal intersection. The grid lines are spaced 50 mm for the first and third column. The grid lines are space 10 mm for the second and third column.

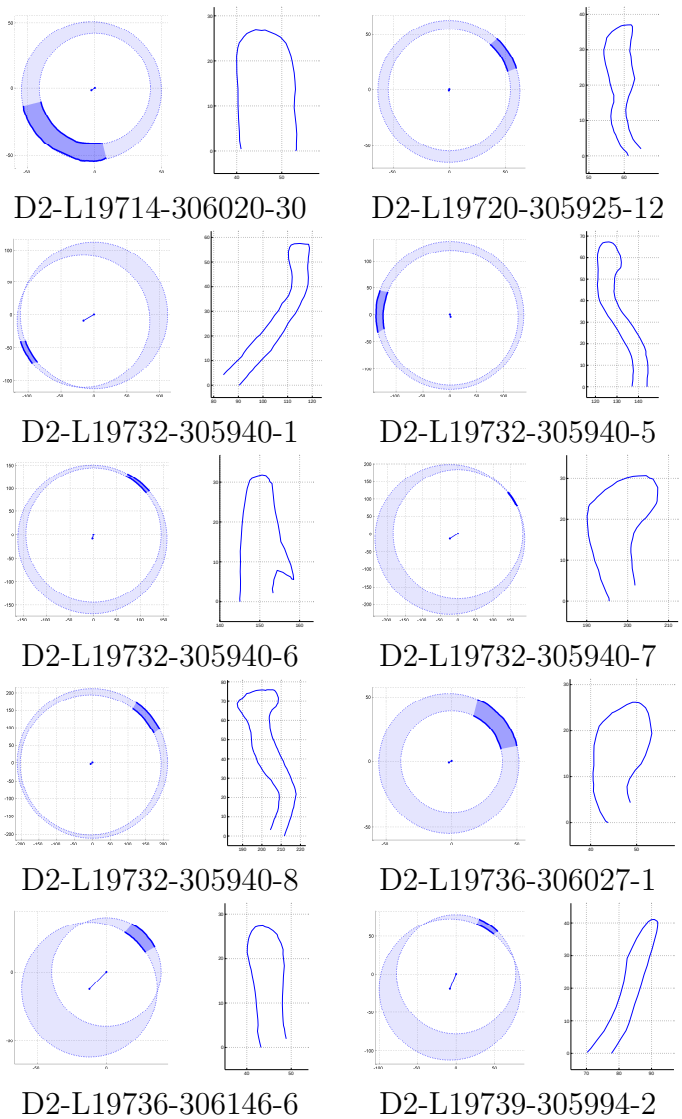

Figure A.5: Horizontal intersections and profile lines.

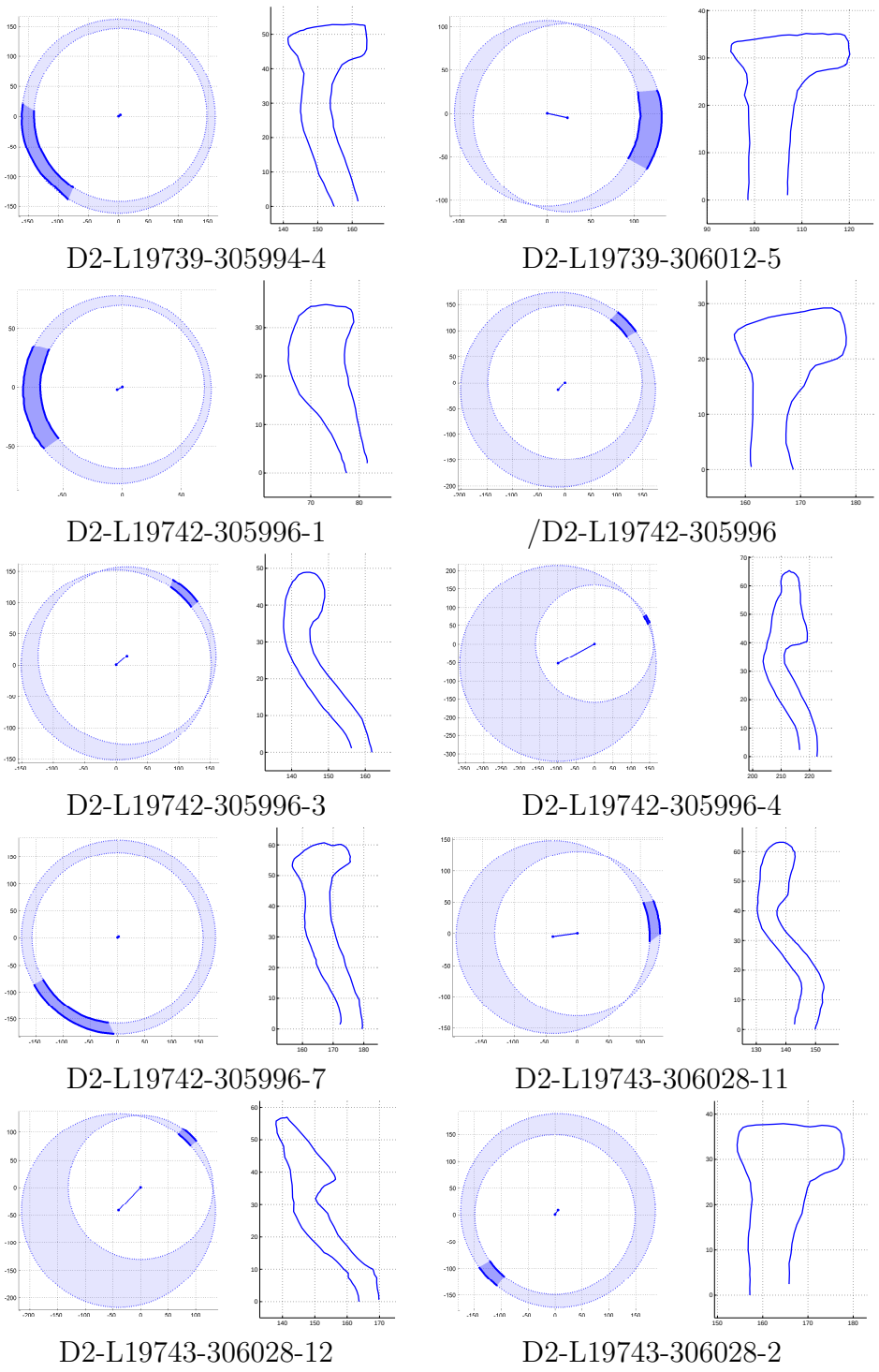

Figure A.6: Horizontal intersections and profile lines.

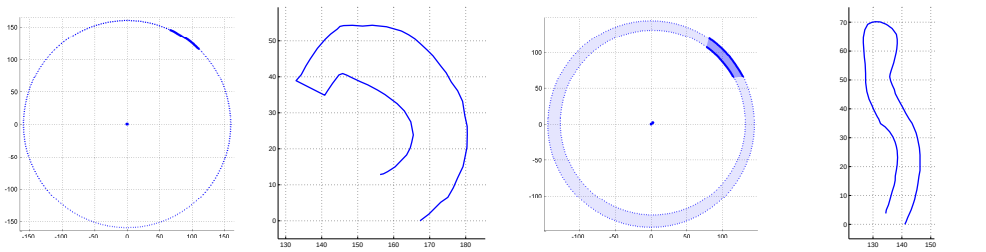

D2-L19743-306028-33 D2-L19743-306028-3

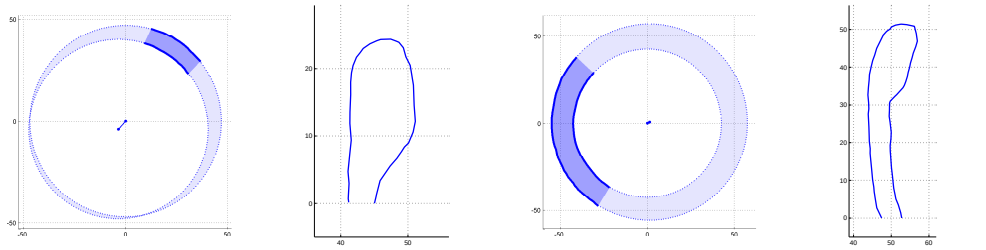

D2-L19743-306028-5 D2-L19743-306028-6

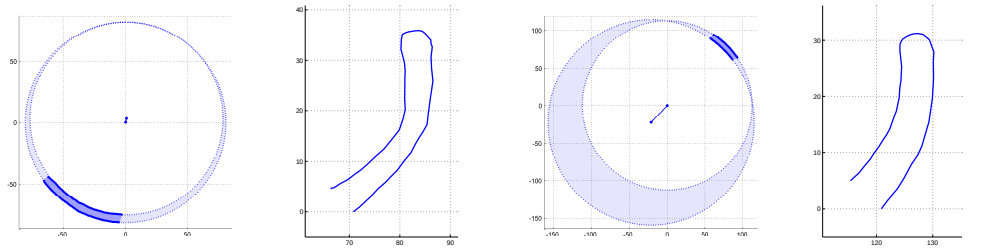

D2-L19743-306051-2 D2-L19751-306083-2

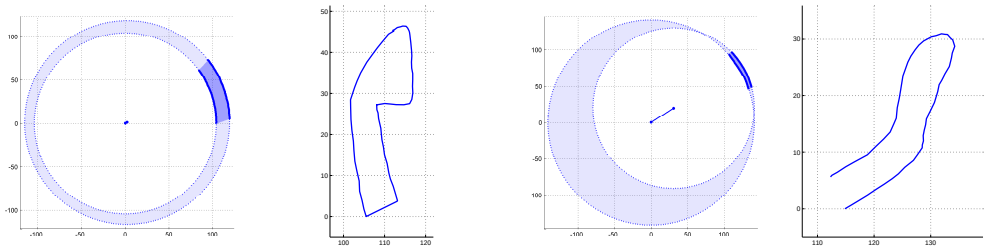

D2-L19766-306231-12 D2-L19766-306231-3

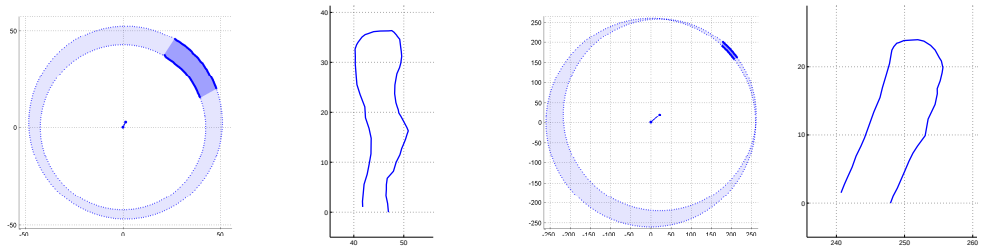

D2-L19766-306231-4 D2-L19766-306231-7

Figure A.7: Horizontal intersections and profile lines.

Bibliography

[ABB+99] E. Anderson, Z. Bai, C. Bischof, S. Blackford, J. Demmel, J. Dongarra, J. Du Croz, A. Greenbaum, S. Hammarling, A. McKenney, and D. Sorensen. *LAPACK User's Guide (http://www.netlib.org/lapack/lug/lapack_lug.html), Third Edition*. SIAM, Philadelphia, 1999.

[ALLT04] S. Antani, D.J. Lee, L.R. Long, and G.R. Thoma. Evaluation of shape similarity measurement methods for spine x-ray images. *Journal of Visual Communication and Image Representation Special issue: Multimedia Database Management Systems*, 15(3):285–302, 2004.

[Arf85] G. Arfken. *Mathematical Methods for Physicists, Chapter 4.7 Eigenvectors, Eigenvalues*. Academic Press, 3rd edition, 1985.

[BDW+04] G.H. Bendels, P. Degener, R. Wahl, M. Krtgen, and R. Klein. Image-Based Registration of 3D-Range Data Using Feature Surface Elements. In Y. Chrysanthou, K. Cain, N. Silberman, and F. Niccolucci, editors, *The 5th International Symposium on Virtual Reality, Archaeology and Cultural Heritage (VAST)*, 2004.

[Blu67] H. Blum. A Transformation for Extracting New Descriptors of Shape. pages 362–380, 1967.

[BM92] P.J. Besl and N.D. McKay. A Method for Registration of 3-D Shapes. *IEEE Trans. on Pattern Analysis and Machine Intelligence*, 14(2), 1992.

[BMP01] S. Belongie, J. Malik, and J. Puzicha. Shape matching and object recognition using shape contexts, January 2001.

[Car86] P.H. Carmichael. NASCA Pottery Construction. In *Nawpa Pacha*, volume 24. Berkeley, California, 1986.

[CC04] D. Cristinacce and T.F. Cootes. A comparison of shape constrained facial feature detectors. In *Proceedings of AFGR'04: 6th Intl. Conf. on Automatic Face and Gesture Recognition*, pages 375–380, May 2004.

[CIG+01] J. Cosmas, T. Itagaki, D. Green, E. Grabczewski, L. Van Gool, A. Zalesny, D. Vanrintel, F. Leberl, M. Grabner, K. Schindler, K. Karner, M. Gervautz, S. Hynst, M. Waelkens, M. Pollefeys, R. DeGeest, R. Sablatnig, and M. Kampel. 3D MURALE: A Multimedia System for Archaeology. In *Proceedings*

of the International Conference on Virtual Reality, Archaeology and Cultural Heritage, pages 297–305, Athens, Greece, November 2001.

[CM92] Y. Chen and G. Medioni. Object Modelling by Registration of Multiple Range Images. *Image and Vision Computing*, 10:145–155, 1992.

[CM02] Y. Cao and D. Mumford. Geometric structure estimation of axially symmetric pots from small fragments. In *Proceedings of SPPRA'02: Signal Processing, Pattern Recognition, and Applications*. IASTED, June 2002.

[Cou79] N.A. Court. *Modern Pure Solid Geometry*. Chelsea Pub Co, 2nd edition, 1979.

[CRB+02] A. Charles, A.M. Ric, B. Bann, K.L. Boehlen, M.C. Gower, P.T. Rumsby, I.S. Boehlen, and N. Sykes. New Techniques for Laser Micromachining MEMS Devices. In Claude R. Phipps, editor, *Proceedings SPIE'02: High-Power Laser Ablation IV*, volume 4760, pages 281–288. SPIE–The International Society for Optical Engineering., September 2002.

[CWK+01] M. Capek, R. Wegenkittl, A. Knig, W. Jaschke, R. Sweeny, and R. Bale. Multimodal Volume Registration Based on Markers. In *Proceedings of the International Conference in Central Europe on Computer Graphics, Visualization and Computer Vision (former Winter School of Computer Graphics)*, pages 17–25, University of West Bohemia, Plyen, Czech Republic, 2001.

[Deg00] R. Degeest. The Common Wares of Sagalassos. In M. Walken, editor, *Studies in Eastern Mediterranean Archaeology*, III. Brepols, 2000.

[DKK96] I. Diamantaras, I. Konstantinos, and S.Y. Kung. *Principal Component Neural Networks*. John Wiley & Sons, 1996.

[DTC+02] R. Davies, C.J. Twining, T.F. Cootes, J.C. Waterton, and C.J. Taylor. A minimum description length approach to statistical shape modeling. *IEEE Transactions on Medical Imaging*, 21(5):525–537, 2002.

[FEC02] R. Fabbri, L.F. Estozi, and L. da F. Costa. On Voronoi Diagrams and Medial Axes. *Journal of Mathematical Imaging and Vision*, 17:27–40, July 2002.

[FJ89] P.J. Flynn and A.K. Jain. On Reliable Curvature Estimation. pages 110–116, 1989.

[Gat84] I. Gathmann. ARCOS, ein Gerät zur automatischen bildhaften Erfassung der Form von Keramik. *FhG - Berichte*, (2):30–33, 1984.

[GGS94] W. Gander, G.H. Golub, and R. Strebel. Least-squares fitting of circles and ellipses. *BIT*, 34:558–578, 1994.

[Gil01] A. Gilboa. *Southern Phoenicia during Iron Age IIa in the light of the Tel Dor excavations. Ph.D. thesis*. The Hebrew University, Jerusalem, 2001.

[Grü79] M. Grünewald. Die Gefässkeramik des Legionslagers von Carnuntum (Grabungen 1968-1977). In *Der römische Limes in Österreich 29*, pages 74–80. Vienna, 1979.

[GW01] I. Guskov and Z. Wood. Topological noise removal. In B. Watson and J. W. Buchanan, editors, *Proceedings of Graphics Interface 2001*, pages 19–26, 2001.

[HS92] R.M. Haralick and L.G. Shapiro. *Computer and Robot Vision*, volume I. Addison-Wesley, 1992.

[HT00] A. Hill and C.J. Taylor. A framework for automatic landmark identification using a new method of nonrigid correspondence. *IEEE Transactions on Pattern Analysis and Machine Intelligence*, 22:241–251, March 2000.

[Jol02] I.T. Jolliffe. *Principal Component Analysis, 2nd Edition.* Springer, 2002.

[Kam03] M. Kampel. *3D Mosaicing of Fractured Surfaces. Ph.D. thesis.* Vienna University of Technology, Inst. of Computer Aided Automation, Pattern Recognition and Image Processing Group, 2003.

[KK02] B. Kegl and A. Krzyzak. Piecewise linear skeletonization using principal curves. *IEEE Transactions on Pattern Analysis and Machine Intelligence*, 24:59–74, 2002.

[KS99a] M. Kampel and R. Sablatnig. On 3d Modelling of Archaeological Sherds. In *Proceedings of the International Workshop on Synthetic-Natural Hybrid Coding and Three Dimensional Imaging*, pages 95–98, 1999.

[KS99b] M. Kampel and R. Sablatnig. Range image registration of rotationally symmetric objects. In Norbert Brändle, editor, *Computer Vision - CVWW'99, Proc. of the Computer Vision Winter Workshop, Rastenfeld*, pages 69–77, Vienna, Austria, 1999. Vienna University of Technology, Institute of Computer Aided Automation, Pattern Recognition and Image Processing Group.

[KS01] M. Kampel and R. Sablatnig. On using 3d multimedia tools to measure, reconstruct and visualize an archaeological site. *Forum Archaeologiae, Zeitschrift für klassische Archaeologie*, 19(IV), 2001.

[Lau01] C. Laugerotte. *Virtual 3D Reconstruction in Archaeology. Ph.D. thesis.* Université Libre de Bruxelles, Belgique, 2001.

[Leu87] U. Leute. *Archaeometry: An Introduction to Physical Methods in Archaeology and the History of Art.* John Wiley & Sons, December 1987.

[Lis99] C. Liska. Das Adaptive Lichtschnittverfahren zur Oberflächenkonstruktion mittels Laserlicht. Master's thesis, Vienna University of Technology, Vienna University of Technology, Institute of Computer Aided Automation, Pattern Recognition and Image Processing Group, April 1999.

[LK89] U. Lübbert and U. Kampffmeyer. Forschungsprojekt ARCOS: Ein Rechner und Programmsystem für die Archäologie. *Archäologie in Deutschland*, (Heft 1/89):36–40, 1989.

[Mar03] H. Mara. Automated profile extraction of archaeological fragments. Technical Report PRIP-TR-083, Vienna University of Technology, Inst. of Computer Aided Automation, Pattern Recognition and Image Processing Group, 2003.

[MGI04] T. Michel, R. Gottschalg, and D.G. Infield. Large area laser scanning of amorphous silicon modules. In *Proceedings of the 19th Photovoltaic Solar Energy Conference*, 2004.

[MK03] H. Mara and M. Kampel. Automated Extraction of Profiles from 3D Models of Archaeological Fragments. In O. Altan, editor, *Proc. of CIPA2003: XIX CIPA Int. Symposium: New Perspectives to Save Cultural Heritage*, pages 87–93. CIPA 2003 organising committe, 2003.

[MKF04] P. Min, M. Kazhdan, and T. Funkhouser. A comparison of text and shape matching for retrieval of online 3d models. In *Proceedings of ECDL'04: European Conference on Digital Libraries*, pages 209–220. Springer-Verlag, September 2004.

[MLCT03] F. J. Melero, A. Leon, F. Contreras, and J.C. Torres. A new system for interactive vessel reconstruction and drawing. In *Proceedings of CAA'03: Computer Applications in Archaeology*, pages 8–12, April 2003.

[MM88] M. Marcus and H. Minc. *Introduction to Linear Algebra*. New York: Dover, 1988.

[Nal93] V. S. Nalwa. *A Guided Tour Of Computer Vision*. Addison-Wesley, 1993.

[ND97] F. Nilsson and P.E Danielsson. Finding the minimal set of maximum disks for binary objects. *Graphical Models and Image Processing*, 59:55–60, 1997.

[NK02] M. Novotni and R. Klein. Computing Geodesic Distances on Triangular Meshes. In *Proceedings of The 10-th International Conference in Central Europe on Computer Graphics, Visualization and Computer Vision'2002 (WSCG'2002)*, February 2002.

[OTV93] C. Orton, P. Tyers, and A. Vince. *Pottery in Archaeology*, 1993.

[Plü68] J. Plücker. *Neue Geometrie des Raumes Gegründet auf die Betrachtung der Geraden Linie als Raumelement*. B.G.Teubner, 1868.

[PNN06] E. Pichon, D. Nain, and M. Niethammer. A laplace equation approach for shape comparison. In *Proceedings of SPIE'06: Medical Imaging*, page in press, February 2006.

[PPR99] H. Pottmann, M. Peternell, and B. Ravani. An introduction to line geometry with applications. *Computer Aided Design*, 31:3–16, 1999.

[PR98] H. Pottmann and T. Randrup. Rotational and helical surface approximation for reverse engineering. *Computing*, 60:307–322, 1998.

[PVC+01] M. Pollefeys, M. Vergauwen, K. Cornelis, F. Verbiest, J. Schouteden, J. Tops, and L.V. Gool. 3D Acquisition of Archaeological Heritage from Images. In *Proc. of CIPA'01: XVIII Int. Symposium of CIPA*, volume Vol. XVIII-2001, pages 381–388. CIPA International Archive for Documentation of Cultural Heritage, 2001.

[PW01] H. Pottmann and J. Wallner. *Computational Line Geometry*. Springer Verlag, 2001.

[RJ66] A. Rosenfeld and J.Pfaltz. Sequential Operations in digital picture processing. *Journal of the Association for Computing Machinery*, 13:471–494, 1966.

[Rob96] L. Robert. Camera Calibration without Feature Extraction. *Computer Vision and Image Understanding*, 63(2):314–325, March 1996.

[SA01] Y. Sun and M.A. Abidi. Surface Matching by 3D Point's Fingerprint. In *Proceedings. Eighth IEEE International Conference on Computer Vision (ICCV'01)*, volume 2, pages 263–269, 2001.

[SBTZ99] K. Siddiqi, S Bouix, A. Tannenbaum, and S.W. Zucker. The Hamilton-Jacobi Skeleton. In *Proceedings of ICCV99: IEEE International Conference on Computer Vision*, pages 828–834. IEEE, September 1999.

[Sha48] C.E. Shannon. A Mathematical Theory of Communication. *Bell System Technical Journal*, 27:379–423 and 623–656, July and October 1948.

[SK02] R. Sablatnig and M. Kampel. Model-based Registration of Front- and Backviews. *Computer Vision and Image Understanding*, 87(1–3):90–103, July 2002.

[SMD91] R. Sablatnig, C. Menard, and P. Dintsis. A Preliminary Study on Methods for a Pictorial Acquisition of Archaeological Finds. Technical Report PRIP-TR-010, Vienna University of Technology, Institute of Computer Aided Automation, Pattern Recognition and Image Processing Group, 1991.

[SP94] S. Sclaroff and A. P. Pentland. Search by shape examples: Modeling nonrigid deformation. Technical Report 1994-015, 1994.

[Ste88] C. Steckner. SAMOS: Dokumentation, Vermessung, Bestimmung und Rekonstruktion von Keramik. *Akten des 13. internationalen Kongresses für klassische Archäologie - Berlin*, pages 631–635, 1988.

[Ste89] C. Steckner. Das SAMOS Projekt. *Archäologie in Deutschland*, (Heft 1):16–21, 1989.

[Ste00] E. Stern. *Dor - Ruler of the Seas*. Israel Exploration Society, 1994, extended 2000.

[Str88] G. Strang. *Linear Algebra and its Applications*. Harcourt Brace Jovanovich College Publishers, Orlando, FL, 3rd edition, 1988.

[TF95] E. Trucco and R.B. Fisher. Experiments in Curvature-Based Segmentation of Range Data. *IEEE Transactions on Pattern Analysis and Machine Intelligence*, 17(2):177–182, 1995.

[Tho03] H.H. Thodberg. *Minimum Description Length Shape and Appearance Models*, volume 2732. 2003.

[TK98] H. Tek and B.B. Kimia. Curve evolution, wave propagation and mathematical morphology. In *Proceedings of ISMM'98: Fourth International Symposium on Mathematical Morphology*, pages 305–322. Kluwer Academic, June 1998.

[Tos02] S. Tosovic. Adaptive 3D Modeling of Objects by combining Shape from Silhouette and Shape from Structured Light. Master's thesis, Vienna University of Technology, Vienna University of Technology, Institute of Computer Aided Automation, Pattern Recognition and Image Processing Group, February 2002.

[Tsa86] R. Y. Tsai. An Efficient and Accurate Camera Calibration Technique for 3D Machine Vision. In *Proceedings of IEEE Conference on Computer Vision and Pattern Recognition*, 1986.

[UD02] F. Utili and Ph. Dolmazon. Bemerkungen zu drei attischen Trinkgefäßen im Reiss-Museum in Mannheim. In M. Bentz, editor, *Vasenforschung und Corpus vasorum antiquorum: Standortbestimmung und Perspektiven, Beihefte zum CVA 1*, pages 37–. 2002.

[VH96] T. Várady and T. Hermann. Best fit surface curvature at vertices of topologically irregular curve networks. In *Proceedings of the 6th IMA Conference on the Mathematics of Surfaces*, pages 411–427. Clarendon Press, 1996.

[WT02] A. Wieczorek and M. Tellenbach. Exkurs zur Frage der Drehscheibenkeramik. In *An die Mächte der Natur - Mythen der altperuanischen Nasca-Indianer. Katalog zur Ausstellung im Reiss-Engelhorn-Museum. Mainz: Philipp von Zabern.*, pages 54–63. 2002.

[YM97] S.B. Yacoub and C. Menard. Robust Axis Determination for Rotational Symmetric Objects out of Range Data. In W. Burger and M. Burge, editors, *Proceedings of the 21th Workshop of the AAPR/ÖAGM*, pages 197–202, Hallstatt, Austria, May 1997.

[Zha00] Z. Zhang. A Flexible New Technique for Camera Calibration. *IEEE Transactions on Pattern Analysis and Machine Intelligence*, 22(11):1330–1334, November 2000.